

DISS. ETH NO. 18203

**CMS Pixel Module Readout Optimization
and
Study of the B^0 Lifetime
in the Semileptonic Decay Mode**

A Dissertation submitted to
ETH Zurich
for the Degree
Doctor of Sciences

presented by

Sarah Dambach
Staatsexamen, University of Heidelberg
10. June 1980
citizen of Germany

accepted on the recommendation of
Prof. Dr. Urs Langenegger
Prof. Dr. Roland Horisberger

2009

Abstract

After more than twenty years of development, the CERN Large Hadron Collider will start continuously operating in mid 2009. An enormous amount of high energy collisions will take place inside the CMS experiment. The innermost detector of this experiment is the barrel pixel detector, with its main goals of track and vertex reconstruction. To do this reconstruction with a high precision, the charge produced inside the silicon sensor is read out as an analog signal. In the first part of this work, the analog readout chain is optimized by setting digital-to-analog converters on the readout chip. Procedures are developed to apply this optimization on more than 10'000 readout chips for the entire detector. The optimization is verified by comparing all optimized chips and with a simulation studying the hit resolution inside the detector.

In the second part of this work the lifetime measurement of the B^0 meson is studied in the semileptonic decay mode using a new reconstruction method for the undetected neutrino appearing in this decay. Since the decay vertex of the B^0 meson is a crucial input parameter for this method, an optimal analog readout is essential. Furthermore, the vertex resolution is optimized by comparing different fit methods. Various consequences of the neutrino reconstruction method are studied. Finally, the new method leads to a reconstruction of the B^0 lifetime without introducing a bias.

Zusammenfassung

Nach einer mehr als zwanzigjährigen Entwicklungsphase wird der LHC am CERN Mitte 2009 seinen kontinuierlichen Betrieb aufnehmen. Hierbei werden grosse Mengen hochenergetischer Kollisionen im CMS Experiment stattfinden. Der innerste Detektor dieses Experiments ist der Barrel Pixeldetektor mit den Hauptzielen Spur- und Vertexrekonstruktion. Um diese Rekonstruktion mit hoher Präzision zu gewährleisten, wird die Ladung, die im Siliziumsensor produziert wurde, analog ausgelesen. Im ersten Teil dieser Arbeit wird die analoge Auslekette optimiert, indem Digital-Analog-Wandler (DACs) auf dem Auslesechip gesetzt werden. Methoden werden entwickelt, um diese Optimierung auf die mehr als 10.000 Auslesechips des Detektors anzuwenden. Die Optimierung wird verifiziert, indem alle optimierten Chips verglichen werden und durch eine Simulation, die die Trefferauflösung innerhalb des Detektors untersucht.

Im zweiten Teil dieser Arbeit wird die Messung der Lebensdauer des B^0 Mesons über den semileptonischen Zerfall untersucht, wobei eine neue Rekonstruktionsmethode für das undetektierte Neutrino dieses Zerfalls verwendet wird. Da der Zerfallsvortex des B^0 Mesons ein entscheidender Eingangsparameter für diese Methode ist, ist eine optimale Auslese von äusserst wichtiger Bedeutung. Ausserdem wird die Vertexpauflösung optimiert, indem verschiedene Fitmethoden verglichen werden. Diverse Folgen der Neutrinorekonstruktionsmethode werden untersucht. Letztendlich führt die neue Methode zur Rekonstruktion der B^0 Lebensdauer, ohne eine tendenzielle Fehlmessung einzuführen.

Contents

1	Introduction	1
2	The LHC and the CMS Experiment	3
2.1	The Large Hadron Collider	3
2.2	Physics with the LHC	5
2.2.1	Higgs Boson	5
2.2.2	Supersymmetry	6
2.3	The Compact Muon Solenoid Experiment	7
2.3.1	The Solenoid Magnet	9
2.3.2	The Tracking System	9
2.3.3	The Electromagnetic Calorimeter	11
2.3.4	The Hadron Calorimeter	12
2.3.5	The Muon System	12
2.3.6	The Trigger System	13
2.3.7	Alignment of the Detector	14
I	CMS Pixel Module Readout Optimization	17
3	The Pixel Barrel Detector	19
3.1	The Pixel Barrel Detector Module	19
3.1.1	The Silicon Sensor	20
3.1.2	The Readout Chip	21

3.1.3	HDI and TBM	21
3.2	Purpose of the Pixel Barrel Detector	22
3.2.1	Tracking	22
3.2.2	Vertex Reconstruction	22
3.3	The Readout Chain	23
4	Optimization Criteria	27
4.1	Pulse Height Distributions	27
4.1.1	Linearity in the Low V_{cal} Range	27
4.1.2	Linearity in the Full V_{cal} Range	29
4.2	Timewalk	29
4.3	Address Levels	30
5	DAC Setting	33
5.1	Generally optimized DACs	33
5.2	Dynamically optimized DACs	36
5.3	Registers	42
6	Setting Verification	43
6.1	P_1 Distributions	43
6.2	ADC Range Utilization	43
6.3	Position Resolutions	44
6.3.1	Influence of the Responses and Calibrations	45
6.3.2	Influence of the Pseudorapidity Range	47
6.3.3	Influence of the Trimming	47
6.3.4	Influence of the Uniformity of the Calibration	48
II	Study of the B^0 Lifetime in the Semileptonic Decay Mode	51
7	B Physics	53
7.1	Historical Aspects of B -physics	53
7.2	The CKM Matrix and CP Violation	54
7.2.1	The CKM Matrix	54
7.2.2	CP Violation	55
7.2.3	Experimental Determination of the CKM Matrix Elements	56
7.3	B Mesons	57
7.3.1	Lifetimes of B Mesons	58
7.3.2	Heavy Flavor Production	59
7.3.3	The B^0 Decay	60

8	The Neutrino Reconstruction Method	63
8.1	Motivation	63
8.2	The k -Factor Method	63
8.3	Kinematics of B^0 Decays	65
8.4	Comparison of k -Factor and Neutrino Reconstruction Method	68
8.5	Experimental Limitations	70
9	Monte Carlo Production	71
9.1	Simulation	71
9.2	The Signal Sample	71
9.3	The Data Sample	72
10	Event Reconstruction	75
10.1	Trigger Paths	75
10.2	Candidate Construction	77
10.3	Track Reconstruction Efficiencies	79
10.4	Candidate Selection	80
10.5	D^0 Mass Distributions	82
10.6	Vertex Fitting	84
10.6.1	The Kinematic Vertex Fitter	85
10.6.2	Different Approaches of Fitting the B^0 vertex	86
10.7	Results of the Neutrino Reconstruction	88
10.7.1	Selection of a Neutrino Solution	89
10.7.2	Candidates with a Negative Radicand	90
11	Study of the Lifetime Measurement	93
11.1	Proper Time Reconstruction	93
11.2	Lifetime Fit	93
11.3	Shape of the Proper Time Distribution	96
11.4	Systematic Errors	98
11.5	Outlook	99
12	Conclusions	101
	Bibliography	103
	Acknowledgements	107
	Curriculum Vitae	109

1

Introduction

On October 21, 2008 the Large Hadron Collider (LHC) at the Conseil Européen pour la Recherche Nucléaire (CERN) in Geneva, Switzerland, was officially inaugurated. It is the world's largest and highest-energy particle accelerator ever built and is designed to accelerate protons to an energy of 7 TeV. At four points of the 27 km long ring experiments are placed, which are dedicated to measure the decay products of the colliding particles. One of the two multi purpose detectors is the Compact Muon Solenoid (CMS) Experiment. It consists of several sub-detectors to precisely measure tracks and energies of the arising particles. The heart of all those detectors is the pixel detector. This is a silicon detector with an active area of about 1 m², which consists of three barrel layers placed radially around the interaction point and two discs at each end of the barrel part.

Besides the large field of new physics that is expected to be discovered with the LHC, there is also a potential for precision measurements of already known fields. For instance, there will be many interesting events that contain B mesons. These mesons have lifetimes of the order of pico seconds resulting in a flight length of a few hundred micro meters. Therefore, they decay even inside the beampipe, far away from the first layer of the pixel detector. Nevertheless, their decay length can be measured by vertexing the tracks of their decay products. To do this with a high precision, a pixel detector with a very good hit resolution is needed. In the CMS pixel detector, this is realized by a small size of the pixels ($100 \mu\text{m} \times 150 \mu\text{m}$) and benefiting from the fact that the produced charge inside a sensor of the detector is shared between pixels due to a drift caused by the magnetic field of the experiment.

A detailed overview of the LHC and the CMS experiment is given in Chapter 2. Here, also two most popularly investigated fields of physics, the search for the Higgs boson and for supersymmetry, are discussed. In Chapter 3, the layout and functionality of the pixel detector are explained. To really be able to benefit from the charge

sharing between pixels, a very precise readout of the produced charge is needed. This precision can be optimized by adjusting 26 digital-to-analog converters that are placed on the readout chip and have an influence on the analog signal. A description of those criteria is given in Chapter 4. In Chapter 5 the concrete optimization of all 26 digital-to-analog converters is discussed. The results of the optimization and its influence on the hit resolution of the pixel detector are presented in Chapter 6.

From Chapter 7 on, this work is dedicated to an application of the optimization above. The lifetime measurement of the B^0 meson is studied in the semileptonic decay mode using a new method. After an overview of the history and the theory of B -physics, the used decay chain of the B^0 meson is introduced. In Chapter 8, a new method of reconstructing the B^0 meson is explained and compared to the conventional one. Chapter 9 reports on the produced data on which the measurement is performed, while in Chapter 10, the event reconstruction and its quality and efficiency are discussed. The measurement of the lifetime and the challenges of the new reconstruction method are explained in Chapter 11. Here, also an outlook is given and open issues are discussed. A summary of the complete work is given in Chapter 12.

The LHC and the CMS Experiment

2.1 The Large Hadron Collider

The Large Hadron Collider (LHC) is a proton accelerator placed in a 27 km long circular tunnel 50 to 175 meter below ground at the Conseil Européen pour la Recherche Nucléaire (CERN) in Geneva, Switzerland [1]. It consists of two separate beam pipes to accelerate protons in opposite directions up to an energy of 7 TeV. The increase in the proton energy is achieved by 1232 super-conducting dipole magnets, while the focusing of the beam is guaranteed by quadrupole, sextupole and octupole magnets. All magnets are cooled by superfluid helium to their operation temperature of 1.9 K.

Before the protons are injected into the LHC, they need to be pre-accelerated. This is done using the existing accelerator infrastructure at CERN: the Linear Accelerator (LINAC), the Proton Synchrotron Booster (PSB), the Proton Synchrotron (PS), and the Super Proton Synchrotron (SPS) (compare Figure 2.1). In the PS, the protons are accumulated as they will be injected into the LHC, grouped in bunches of nominally 10^{11} with a 25 ns spacing between the bunches. The root mean square (RMS) of their length is 8 cm and of their diameter $16 \mu\text{m}$. After the protons are accelerated in the SPS to an energy of 450 GeV, they are transferred the LHC, where their energy is increased by 0.5 MeV per turn up to the nominal energy of 7 TeV. Besides the acceleration of protons, heavy ions can be accelerated.

At four points of the LHC the two beams are brought into collision, whereby particles are generated. Those can be detected and measured precisely by the two general purpose experiments ATLAS (A Toroidal LHC Apparatus) and CMS (Compact Muon Solenoid) and the LHCb detector, which is focused on B physics. ALICE (A Large Ion Collider Experiment) is dedicated to measure heavy ion physics.

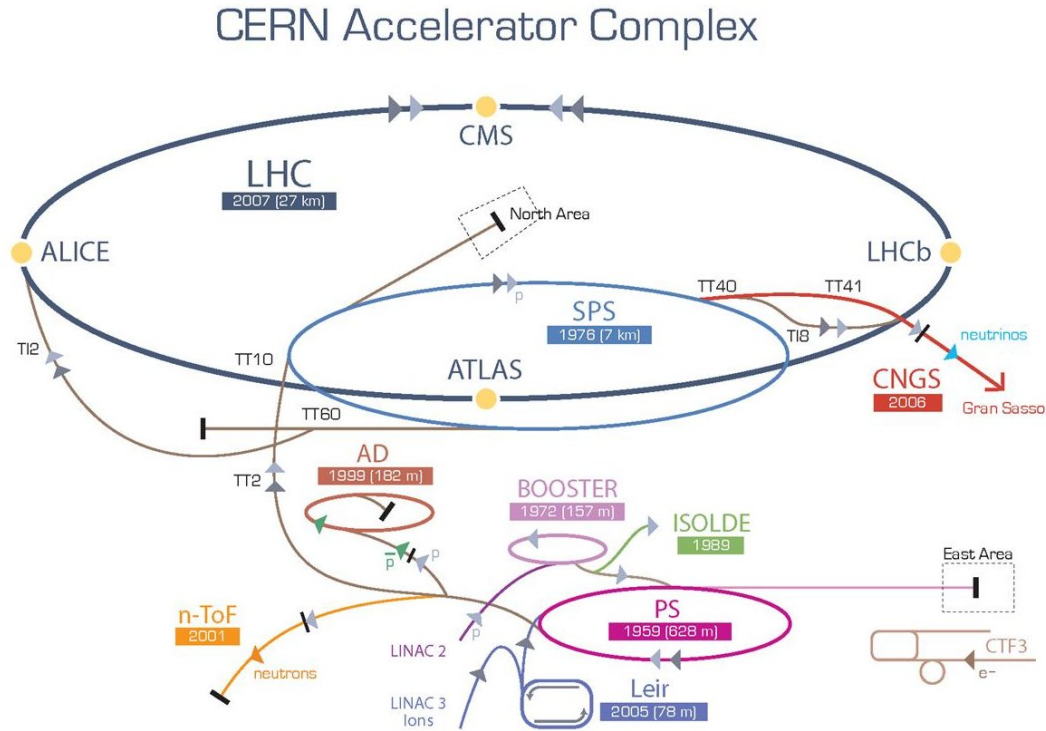


Figure 2.1: The CERN accelerator complex.

With an average data taking time of 50 days at the nominal high luminosity of $\mathcal{L} = 10^{34} \text{ cm}^{-2} \text{ s}^{-1}$, $\approx 50 \text{ fb}^{-1}$ can be collected per year. Hence the LHC increases the high energy frontier by a factor 7 and raises proton luminosities by about two orders of magnitude compared to the Tevatron.

The successful start-up of the LHC took place at September 10, 2008 when the first beam was steered around the complete ring. This was a great moment after more than two decades in development of both the collider and the experiments. During commissioning (without beam) of the final LHC sector at high current for operation at 5 TeV, an incident occurred at September 19, resulting in a large helium leak into the tunnel. The reason was a faulty electrical connection between two of the accelerator's magnets which caused a mechanical damage. Since the time needed for bringing the magnets in the involved sector to room temperature, to repair the defect and to cool down again is several months, a restart of the accelerator complex is forseen in 2009 [2, 3, 4, 5].

2.2 Physics with the LHC

The main goal of the LHC is the search for new physics, of which the search for the Higgs boson and supersymmetric (SUSY) particles are the most popular ones. During the first time of operation with low luminosity and low trigger thresholds there is a huge potential for B physics, which will be discussed in more detail in Chapter 7.

2.2.1 Higgs Boson

In weakly coupled perturbation theory, elastic W boson scattering is characterized by an amplitude that is quadratically growing with energy. The divergences in the terms of this amplitude can be canceled by adding the exchange of an additional weakly interacting particle. The couplings of this particle to all fermions and gauge bosons depend on its mass.

A mechanism of generating this additional particle was first introduced by Peter Higgs and others in 1964 [6, 7, 8, 9] and is therefore called Higgs mechanism. A scalar background field is introduced in the form of an isospin doublet of complex fields. By explicitly choosing the ground state of the potential, the local symmetry is spontaneously broken and the W and Z bosons achieve masses (80.4 GeV and 91.2 GeV, respectively), while the photon stays massless. This means that three of the four degrees of freedom of the background field vanish because they are absorbed by the masses of the vector boson field. The remaining scalar field corresponds to the needed weakly interacting scalar particle, the Higgs boson.

The only unknown parameter of the Higgs boson is its mass m_H . Knowing it, all other properties like lifetime, branching ratios, production mechanisms, and cross sections can be calculated. From theory and experiment, upper and lower bounds on m_H exist. LEP excluded masses below $114.4 \text{ GeV}/c^2$ and theoretically the mass is restricted to values below $1 \text{ TeV}/c^2$.

At the LHC, the Higgs boson will be produced via four processes, namely gluon fusion, vector boson fusion, Higgs-strahlung, and Higgs bremsstrahlung off top quarks. The cross sections for those four production mechanisms as a function of the Higgs boson mass are shown in Figure 2.2(a).

The branching ratios of the Higgs boson as function of its mass are shown in Figure 2.2(b). The range is divided into low and high Higgs boson masses by the production threshold of two W bosons at $\approx 160 \text{ GeV}/c^2$. Despite the fact that for low masses the decays into two b quarks and two τ leptons are dominant, the main discovery potential lays on the decay into two photons, since the other modes are dominated by QCD background (Figure 2.3). For Higgs masses above $\approx 160 \text{ GeV}/c^2$, the decays into two W or Z bosons and into leptons are most promising (Figure 2.3).

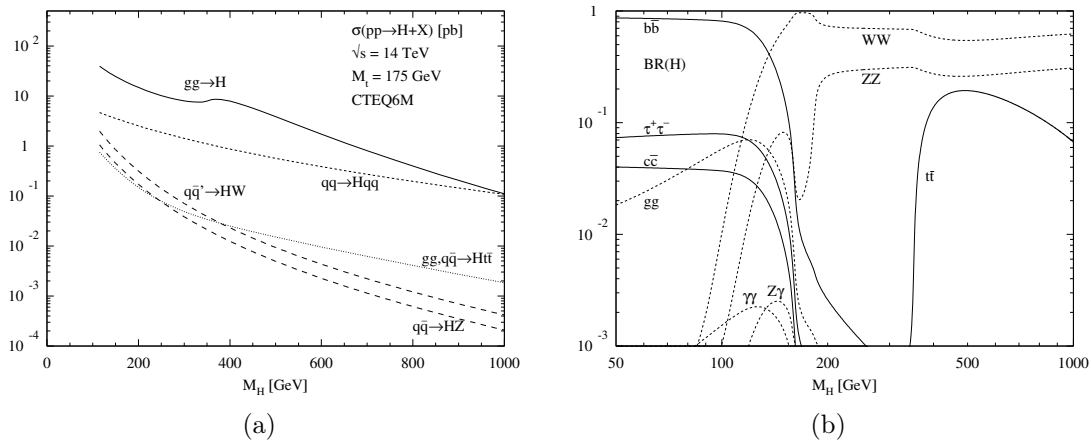


Figure 2.2: Higgs boson production cross sections at the LHC for the various production mechanisms as a function of the Higgs boson mass (a) and branching ratios of the dominant decay modes (b) [10].

2.2.2 Supersymmetry

In the last decades, the Standard Model of particle physics has been tested in various experiments and considered to be an effective theory up to a scale of $\Lambda \approx 1$ TeV. Nevertheless, there are some important hints that it can not be a complete theory of nature. First it does not include gravity and therefore can not be valid at energy scales above $m_{Planck} \sim 10^{19}$ GeV. Second it has been shown that neutrinos oscillate [12] and therefore have a mass $\neq 0$, which was not included in the Standard Model.

Most of the theories for physics beyond the Standard Model are supersymmetric, whereof the Minimal Supersymmetric Standard Model (MSSM) is the simplest one [13]. It introduces for each boson of the standard model a fermionic superpartner (gaugino) and to each fermion a bosonic one (squark and slepton). In addition there are five Higgs bosons: A light (h^0) and a heavy (H^0) neutral scalar Higgs boson, a neutral pseudo-scalar Higgs boson (A^0) and two charged scalar Higgs bosons (H^+ , H^-).

If supersymmetric particles exist in a mass range up to $1 \text{ TeV}/c^2$, they are expected to be detected at the LHC. This can be done in an indirect way, which uses the fact that in some models the lightest supersymmetric particle (LSP) is stable. If it leaves the detector without interacting, this leads to a sizable amount of missing energy that can be measured.

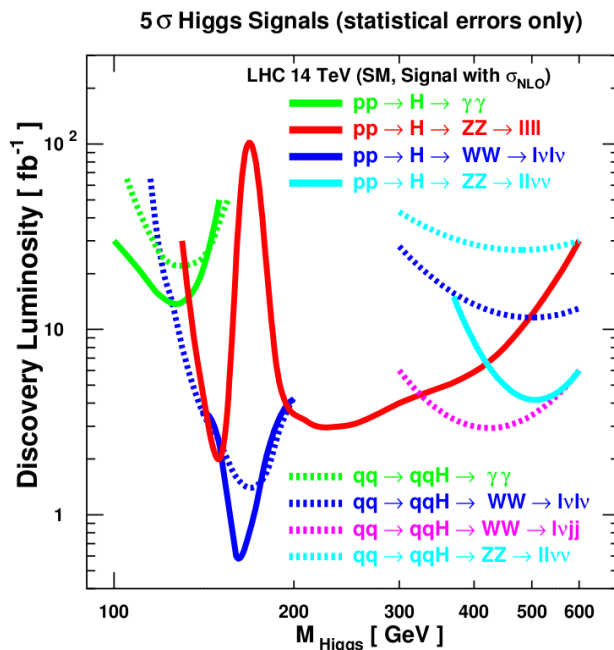


Figure 2.3: Integrated luminosity needed for a Higgs boson discovery [11].

2.3 The Compact Muon Solenoid Experiment

The CMS experiment (Figure 2.4) is a general purpose high energy physics detector located at one of the four interaction points of the LHC near the village of Cessy in France [14, 15]. With its length of 21.6 m and its diameter of 15 m, it is relatively small compared to its weight of 12 500 t. CMS is built in a cylindrical structure composed of a barrel in the center and endcaps at both sides ¹.

CMS has a special focus on the following requirements [14]:

- Good muon identification and momentum resolution over a wide range of momenta in the region $\eta \leq 2.5$, good dimuon mass resolution ($\approx 1\%$ at $100 \text{ GeV}/c^2$), and the ability to determine unambiguously the charge of muons

¹ The CMS coordinate system is defined as follows: The origin is the collision point. The x axis is horizontal, pointing south to the LHC center. The y axis is vertical pointing upwards. The z axis is horizontal pointing west. The sign of $\eta = -\ln(\tan(\frac{\theta}{2}))$ is equal to the sign of z . The polar angle θ is measured w.r.t. the z axis. The azimuthal angle ϕ is measured in the x - y -plane. The magnetic field of the solenoid points into the $+z$ direction.

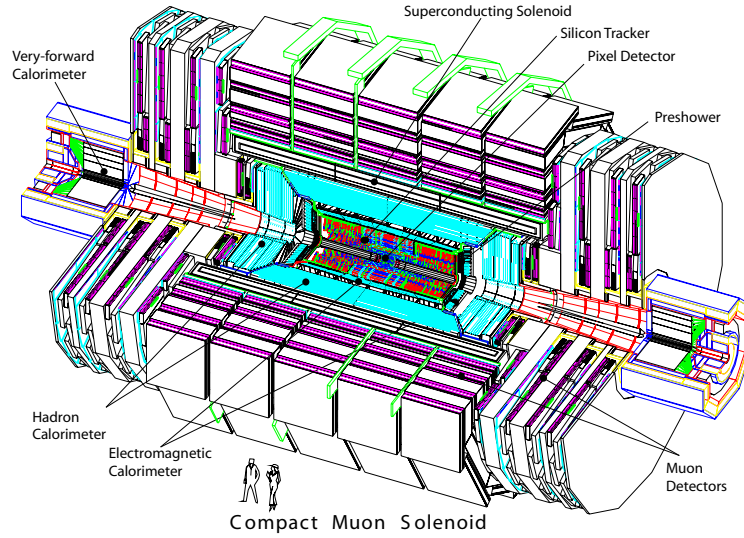


Figure 2.4: The CMS Experiment [14].

with $p \leq 1 \text{ TeV}/c$.

- Good charged particle momentum resolution and reconstruction efficiency in the inner tracker. Efficient triggering and offline tagging of taus and b-jets, requiring pixel detectors close to the interaction region.
- Good electromagnetic energy resolution, good diphoton and dielectron mass resolution ($\approx 1\%$ at $100 \text{ GeV}/c^2$), wide geometric coverage ($\eta \leq 2.5$), measurement of the direction of photons, π^0 rejection and efficient photon and lepton isolation at high luminosities.
- Good E_T and dijet mass resolution, requiring hadron calorimeters with a large hermetic geometric coverage ($\eta \leq 5$) and with fine lateral segmentation ($\Delta\eta \times \Delta\varphi \leq 0.1 \times 0.1$).

Figure 2.5 shows a slice through the CMS detector in the central region with particles and their interactions in the various sub-detectors indicated. Only the main components are shown. From inside out, CMS consists of the tracker to reconstruct the trajectories of all charged particles, the electromagnetic calorimeter to measure the energies of photons and electrons, the hadron calorimeter to measure the energies of hadrons, the coil of the solenoid to provide a 3.8 T magnetic field and the iron return yoke of the solenoid interlaced with muon chambers to measure the momenta

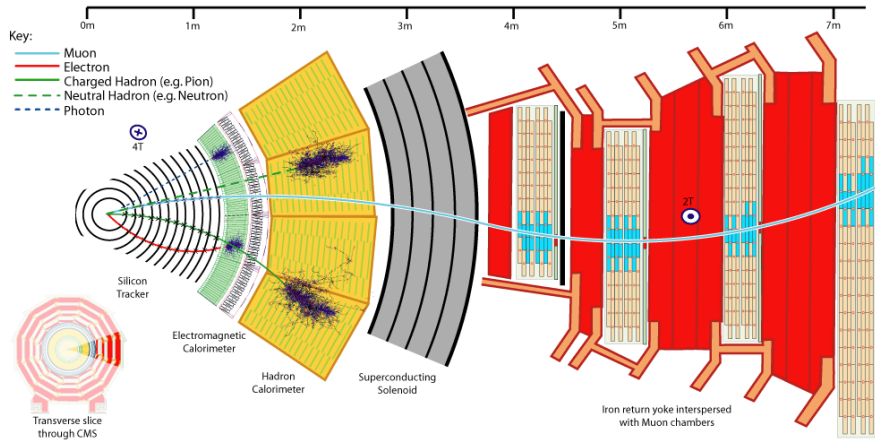


Figure 2.5: Slice through CMS showing particles incident on the different sub-detectors [14].

of muons. A more detailed description of all sub-detectors will be given in the following.

2.3.1 The Solenoid Magnet

To fulfill the requirements of a momentum resolution less than one percent even for high p_t particles, a strong magnetic field is needed. Within the CMS detector this is achieved by a superconducting magnet with a length 12.9 m and an inner diameter of 5.9 m which generates a magnetic field of 4 Tesla [14]. The magnetic flux is returned through a saturated 10 000-t iron yoke with a field of 2 Tesla placed in between the muon chambers. The solenoid is large enough to contain both the tracking system and the calorimeters (ECAL and HCAL). This guarantees that particles do not have to pass a big amount of material before their energy is measured in the calorimeters.

The cold mass of the solenoid is composed of four winding layers of superconducting cable inserted in aluminium. It is placed inside a cryostat cooled by helium to an operational temperature of 4.6 K. At a nominal current of 19.14 kA, a total energy of 2.6 GJ is stored inside the solenoid.

2.3.2 The Tracking System

Three conditions strongly influenced the overall design of the CMS tracking system [14, 15]. Due to the high luminosity of $10^{34} \text{ cm}^{-2}\text{s}^{-1}$ and the short time of 25 ns between bunch crossings, 40 million events are expected per second, each resulting

in about 1000 particles. This requires a high granularity of the detector to have a low occupancy per bunch crossing. The readout of the detector must be fast and the entire system has to be radiation hard. This leads to a full silicon detector technology with decreasing granularity from inside out. To avoid a too high leakage current, which is induced by bulk damage inside the sensor, the whole tracker will be operated at a temperature of -10°C . It covers a range up to $|\eta| = 2.5$.

The main goals of the tracking system are a precise measurement of charged particle trajectories and reconstruction of secondary vertices, which requires a good position and momentum resolution, and a high reconstruction efficiency. Figure 2.6 shows the transverse momentum resolution and the track reconstruction efficiency for muons with transverse momenta of $1\text{ GeV}/c$, $10\text{ GeV}/c$ and $100\text{ GeV}/c$ as a function of the pseudorapidity η . It can be seen that the p_t -resolution decreases with η and the transverse momentum of the muons. The reason for this is the dependency of the transverse momentum resolution $\sigma(p_t)/p_t$ on the transverse momentum itself given by the equation

$$\frac{\sigma(p_t)}{p_t} = \sqrt{\frac{720}{N+4}} \cdot \sigma_x \cdot \frac{p_t[\text{GeV}/c]}{0.3 \cdot B \cdot L^2} \quad (2.1)$$

with N being the number of detector layers, σ_x being the hit resolution of the detector, B being the strength of the magnetic field, and L being the distance between the first and the last detector layer. Note that this equation does not include effects from multiple scattering and energy losses of the passing charged particle.

The efficiency for all transverse momenta of the muons is close to 100 % over almost the full η -range. It only drops down for high η where no tracking detectors are available anymore and for $\eta \approx 0$ due to the gaps in the sensors of the pixel detector here.

The Pixel Detector

In the innermost part around the interaction point within the CMS detector (radii below 10 cm), a very high flux of about $1\text{ MHz}/\text{mm}^2$ is expected. To achieve an occupancy below 1%, a silicon pixel detector is required. It consists of three barrel layers and two endcap discs at each end of the barrel part, with 66 million channels in total. A more detailed description will be given in Chapter 3.

The Silicon Strip Detector

At a distance of 20 cm from the interaction point, where the particle flux has sufficiently dropped, the usage of a pixel detector is not needed any longer, a silicon

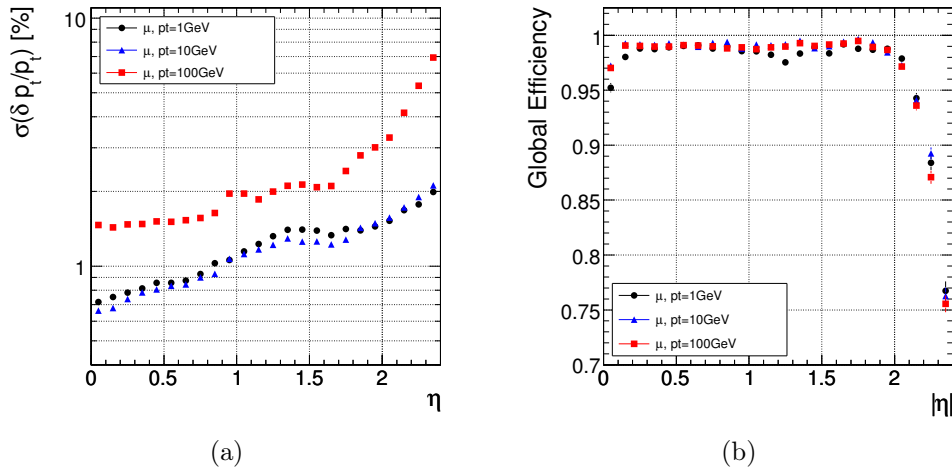


Figure 2.6: Transverse momentum resolution (a) and track reconstruction efficiency (b) for muons of transverse momenta of 1 GeV/c, 10 GeV/c and 100 GeV/c as a function of the pseudorapidity η [14].

strip detector can be used instead. It consists of three parts, namely the Tracker Inner Barrel and Discs (TIB/TID), the Tracker Outer Barrel (TOB) and the Tracker EndCaps (TEC+ and TEC-, the sign indicates the location along the z axis). They consist of modules with on average 10 cm long strips that are oriented parallel to the beam axis in 10 barrel layers and radially in 12 discs at each side.

The TIB consists of four layers with pitches of 80 μm and 120 μm up to a radius of 55 cm, the TID of three discs with pitches between 100 μm and 141 μm up to $z = \pm 110$ cm. Both TIB and TID are surrounded by six layers of the TOB that have strip pitches of 183 μm and 122 μm up to a radius of 116 cm. On each side of the TOB and the TID there are nine discs with strip pitches between 97 μm and 184 μm up to $z = \pm 184$ cm.

To measure the position of a passing particle in both $r\varphi$ - and rz - direction, some of the strips are built in double layers tilted against each other by an angle of 100 mrad. With distance from the interaction point, not only the strip pitch increases, but also strip length, and sensor thickness become larger. All modules are mounted on carbon structures.

2.3.3 The Electromagnetic Calorimeter

The goal of the electromagnetic calorimeter is to measure precisely the energy of electrons and photons which generate electromagnetic showers inside it. It should

be built of a material with a short radiation length and high density to be small enough to fit inside the solenoid [14]. For this reason, lead tungstate (PbWO_4) is used, which has the advantage that 80 % of the scintillation light is emitted within the LHC bunch crossing time of 25 ns. The crystals have a size of $22 \times 22 \text{ mm}^2$ at the front- and $26 \times 26 \text{ mm}^2$ at the backside and a length of 23 cm in the barrel region. In the endcaps, their front face cross section is $28.62 \times 28.62 \text{ mm}^2$, their rear face cross section is $30 \times 30 \text{ mm}^2$ and their length is 22 cm. The calorimeter is built of 61 200 crystals in the barrel and 14 648 in the endcaps. The front faces of the barrel crystals are at a radius of 1.29 m, those of the endcaps at a z -position of 3.15 m. The whole system covers a range up to $|\eta| = 3$. At the operation temperature of 18°C , 4.5 photoelectrons are collected per MeV. The crystals emit blue-green scintillation light which is measured by avalanche photodiodes in the barrel and vacuum phototriodes in the endcaps. To identify neutral pions decaying to two photons, and to improve the position determination of electrons and photons, in the endcaps preshower detectors made of silicon strips with much finer granularity than the crystals are placed in front of the ECAL.

2.3.4 The Hadron Calorimeter

As the name already suggests, the Hadron Calorimeter is used to measure the energy of hadrons like pions, kaons, protons or neutrons. Besides this, it has the important role of measuring the missing transverse energy. Therefore it needs to cover a area as big as possible around the interaction point, which is realized by the four components of the calorimeter [14, 15]. The barrel and endcap hadronic calorimeters, both placed inside the solenoid, cover a pseudorapidity range up to $|\eta| = 3$, while the forward HCAL, placed at 11.2 m from the interaction point extends the coverage up to $|\eta| = 5.2$. Since, at 90° , the total absorber thickness is only 5.82 interaction lengths, the calorimeter is completed by two additional layers of active material outside the solenoid. The HCAL is a sampling calorimeter built of brass interlaced with plastic scintillators as active material to detect the showers generated by the hadrons in the brass.

2.3.5 The Muon System

Since muons penetrate the tracking system, the calorimeters and the coil of the solenoid without being stopped, their track and momentum is again measured in the outer region of the experiment, the muon chambers [14, 15]. Three types of chambers exist: Drift tubes (DT), which provide a precise position measurement, are used in the barrel region, where the muon rate is relatively low, and cover a pseudorapidity range of $|\eta| < 1.2$. Cathode strip chambers (CSC) are used in the

endcap region, where the muon rate is high and the magnetic field is strong and non-uniform. They identify muons in the range $0.9 < \eta < 2.4$. Resistive plate chambers (RPC) are used in both the barrel and the endcap region. Since they provide a time resolution of ~ 1 ns, they are a reasonable completion of the DT and CSC. Due to the large bending power of the magnetic field, even muons with a high p_t can be measured with a reasonable cell size of the muon chambers. The momentum resolution for muons with low p_t is limited by multiple scattering and for muons with high p_t by the chamber resolution. The achievable resolutions using the muon system (in combination with the tracker system) are shown in Figure 2.7. The purposes of the muon system are muon identification, momentum measurements and triggering.

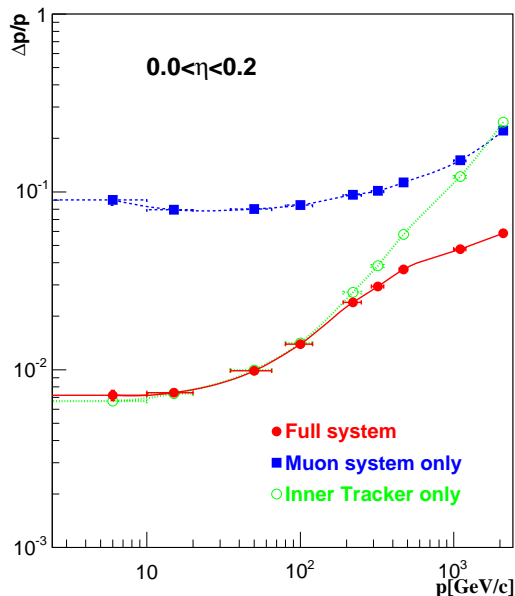


Figure 2.7: Muon momentum resolution in the central detector region ($0 < \eta < 0.2$) as a function of the momentum using the tracking system only, the muon system only and the combination of both [14].

2.3.6 The Trigger System

At the design luminosity, CMS will measure about 10^9 interactions per second. This huge amount of data has to be reduced since only an amount of 100 events per second can be written to disc. This reduction of data is done by a sophisticated

trigger system consisting of two trigger levels, namely the Level-1 trigger (L1) and the High Level Triggers (HLT), as shown in Figure 2.8 [16, 17, 18].

The time needed to send the electronic signals of an event from the detector to the L1 electronics, take the decision of the L1, and send the information whether an event should be stored or not back to the detector is about $3.2 \mu\text{s}$. The L1 decides on the basis of the presence of muons, jets above a specific E_T or p_T threshold or the global amount of E_T or E_T^{miss} measured with the muon system and the calorimeters. This reduces the amount of data to 10^5 events per second, which are buffered in readout electronic buffers (compare Figure 2.8). Here interesting objects in a couple of detector regions are partially reconstructed, combined and processed by the HLT, which is a software farm implemented in about 1000 processors. It reduces the number of events to about 100 per second. The HLT is a very dynamical system that can be adjusted according to luminosity and physics goals.

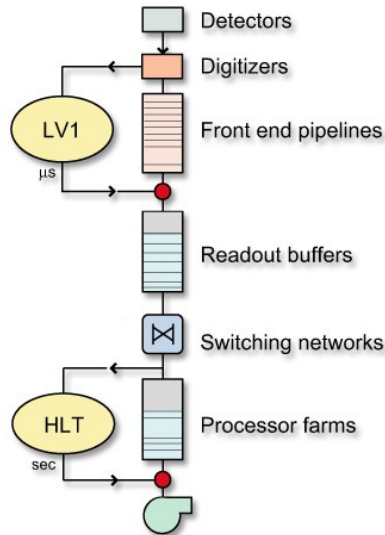


Figure 2.8: The CMS Trigger Strategy, consisting of the L1 electronics, the readout buffers and the HLT software farm.

2.3.7 Alignment of the Detector

The various detector components which actually measure the hits are independent objects. Their position inside the detector is not precisely known and may also

vary with time. The reason for this are construction tolerances, displacements during detector assembly and commissioning, magnetic field distortions and thermal instabilities [19].

Since the momentum and position resolutions of tracks, and therefore also the vertex resolutions, depend on the relative position of the detector components (modules in the tracking and chambers in the muon system) with respect to each other, it is crucial to determine these positions precisely. This alignment is done in four different approaches:

- Precisely measure the positions of single sub-detector components with respect to each other before insertion. This is done in the case of the barrel pixel detector by photographing the assembled detector and measuring the distances between reference points.
- Measure the positions of various sub-detector components with respect to each other after insertion and continuously during operation and use this information in the offline track reconstruction. This is done in case of the silicon strip detector and for the position of the tracking system with respect to the muon system with a laser alignment system.
- Align the detector with muon tracks during operation. This is done for both the tracking and the muon system.

By doing this, the position of the muon detectors can be known up to a precision of $100\ \mu\text{m}$ to $500\ \mu\text{m}$. For the tracking system, precisions up to $10\ \mu\text{m}$ can be achieved.

Part I

CMS Pixel Module Readout
Optimization

3

The Pixel Barrel Detector

The pixel detector is the innermost part of the CMS experiment after the beam pipe and therefore close to the interaction point. It consists of three barrel layers at a radial distance of 4.4 cm, 7.3 cm, and 10.2 cm and two forward disks at $z = \pm 34.5$ cm and $z = \pm 46.5$ cm as shown in Figure 3.1. The barrel part is built of 672 modules and 96 half-modules.

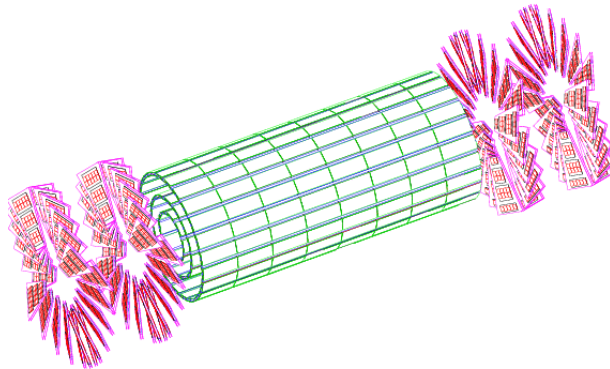


Figure 3.1: Layout of the pixel detector [14].

3.1 The Pixel Barrel Detector Module

Figure 3.2 shows the schematic structure of a barrel detector module. It comprises 16 readout chips (ROCs) with 4160 channels each, where every single one is connected via indium bumps to a common pixelated silicon sensor. On top of the sensor a High

Density Interconnect (HDI), a low mass flexible printed circuit board, is placed. In the middle of this, a token bit manager (TBM) chip is positioned. The voltage is supplied through a copper cable, the data transferred by a Kapton cable. The module is connected to the mechanical structure of the detector by two base strips.

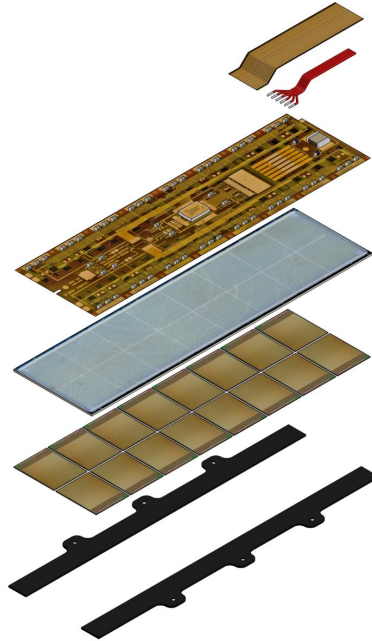


Figure 3.2: Schematic structure of a barrel pixel module: base strips, 16 ROCs, sensor, HDI, power and data cable [15].

3.1.1 The Silicon Sensor

The sensor is made of $285\ \mu\text{m}$ thick silicon with a pixel size of $100\ \mu\text{m} \times 150\ \mu\text{m}$ in r - φ - and z -direction, respectively [20]. The so-called *n-in-n* technology is used, i.e. n-implants are introduced in a n-substrate and the backside of the sensor is p-doped. Biasing the sensor creates a depletion zone inside which electron-hole pairs are generated along the path of a charged particle crossing this zone (Figure 3.3). The *n-in-n* concept is chosen to reach reasonable high signal charges already at low bias voltages. Full depletion is reached with a bias voltage of 150 V, but after irradiation up to 600 V can be applied.

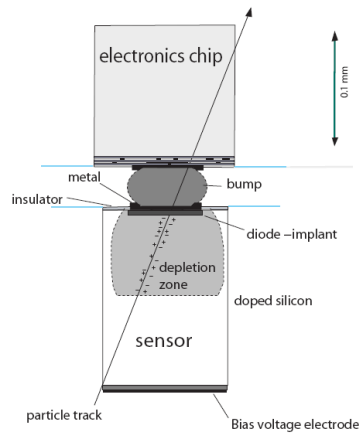


Figure 3.3: Charge deposition in the sensor [21].

3.1.2 The Readout Chip

The ROC is designed to measure the amount of charge produced in the sensor, to amplify it, to compare it to a threshold and to send it out together with the address of the hit pixel. It consists of 4160 pixels arranged in 52 columns and 80 rows. The readout is organized using the column drain mechanism [21]. One token is initialized for the readout of two neighboring columns (therefore they are sometimes also referred to as one double column).

The ROC [22] consists of three main building blocks, 4160 times the pixel unit cell, 26 times the double column periphery, and once the control and interface block (Figure 3.4).

To control and optimize the readout, 26 DACs (digital to analog converters) can be adjusted. One DAC is set to the same value in all pixel units cells and double column peripheries.

3.1.3 HDI and TBM

The HDI is connected to the ROCs by wire bonds and provides the electric connections needed for passing the signals entering and leaving the module. The token bit manager (TBM) chip on top of it controls the readout and programming of a module [23]. It distributes the L1 trigger and the 40 MHz clock over the HDI to the ROCs by initiating a token pass. For each token it writes a header and a trailer to the data coming from the ROCs.

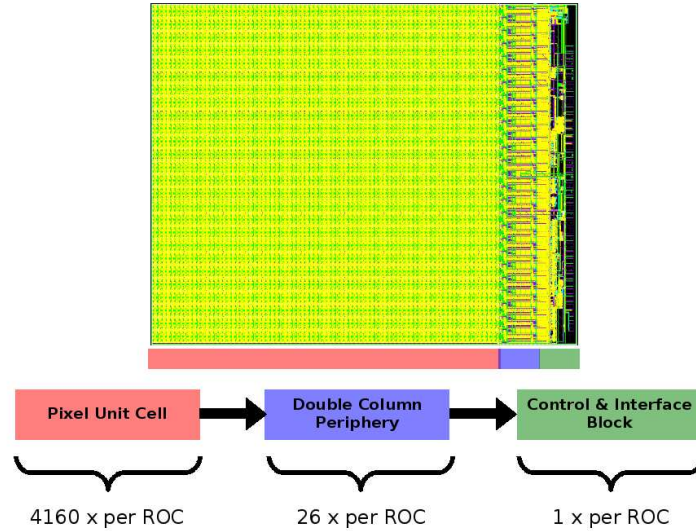


Figure 3.4: Layout of the ROC.

3.2 Purpose of the Pixel Barrel Detector

3.2.1 Tracking

The main advantage of a pixel detector compared to a silicon strip detector is the absence of so-called ghost hits, hits occurring due to wrong combinations of hit strips. Therefore track finding with a pixel detector is much faster and can be used for seeding in the high level trigger.

3.2.2 Vertex Reconstruction

For many physics channels it is very important to distinguish between primary and secondary vertices. Therefore the experiment needs the best possible impact parameter resolution which – under the given conditions of the spatial position of the pixels – directly depends on the resolution of a single hit. For a binary readout the resolution R only depends on the pixel pitch p and is given by:

$$R = \frac{p}{\sqrt{12}} \quad (3.1)$$

For a pixel size of $100 \mu\text{m} \times 150 \mu\text{m}$ this means a resolution of $\approx 30 \mu\text{m}$ in r - φ - and $\approx 40 \mu\text{m}$ in z -direction. The nearly square pixel shape is chosen because precise reconstruction in both, transverse and longitudinal coordinates is important.

To improve the resolution one uses the Lorentz drift and reads out the produced charge as an analog value. In the barrel detector the drift direction of the electron hole pairs is perpendicular to the magnetic field of 4 T and forces them to the neighboring pixel. In the forward detector the modules are tilted by 20° resulting in a turbine-like geometry. This implies that the drift direction of the electron hole pairs is not any longer parallel to the magnetic field.

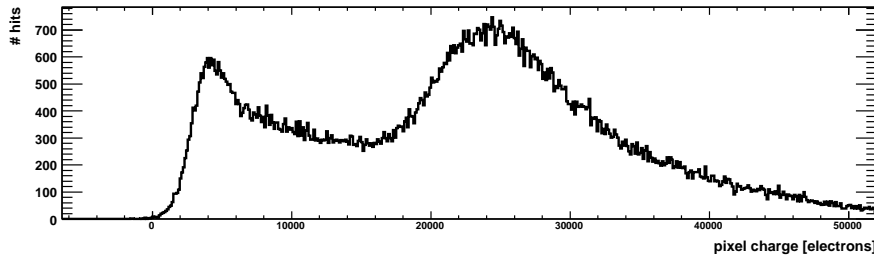


Figure 3.5: Charge distribution of a single pixel measured during a test-beam.

The typical charge distribution inside a single pixel is shown in Figure 3.5. If only one pixel is hit by a charged particle and if there is no Lorentz drift one expects a Landau distribution. Including charge sharing there is an overlaid peak at low charges. The readout must be very precise especially for those pixels with deposited charges below 30'000 electrons. How this can be reached by optimizing the DAC settings is discussed in detail in Chapter 5.

3.3 The Readout Chain

A schematic view of the readout chain is shown in Figure 3.6.

The goal of the ROC is to measure how much ionization charge was produced in which pixel. The charge produced by an ionizing particle in the sensor generates a voltage in the ROC via a capacitor. If a leakage current occurs, it can be compensated for (V_{leak_comp}). The analog signal then goes through the preamplifier (V_{wllPr} and V_{rgPr}) and the shaper (V_{wllSh} and V_{rgSh}).

After the shaper the signal takes two paths, one into the comparator, one into the sample and hold mechanism. When the rising edge of the signal has passed the threshold, the signal height is sampled after some delay (V_{hldDel}) and stored in the sample and hold capacitance until the readout mechanism is started from the periphery. The threshold can be set by a global value for the whole ROC ($V_{thrComp}$) and four trim bits on a pixel level (applied via V_{trim}).

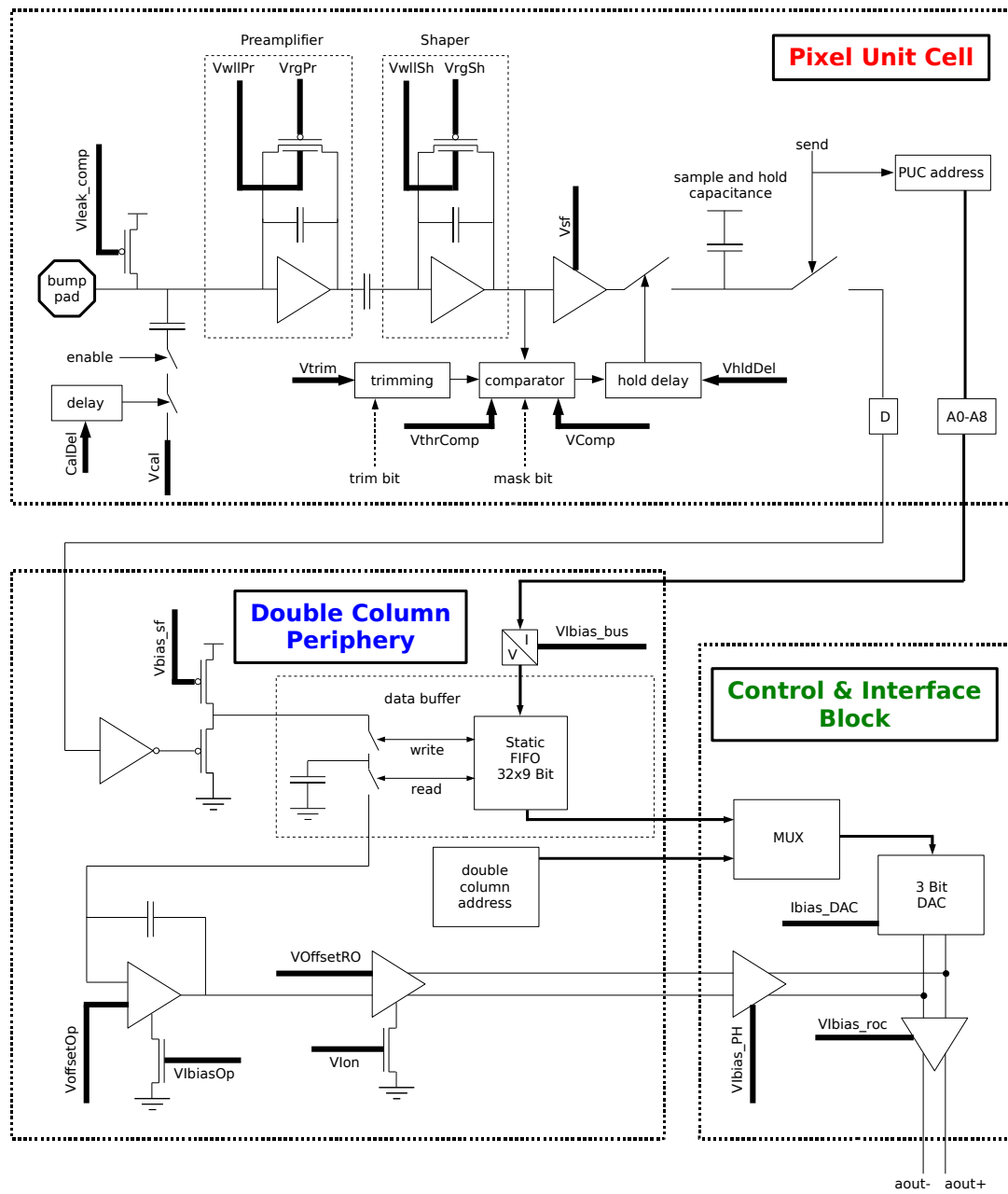


Figure 3.6: Schematic view of the readout chain.

Subsequently the signal is forwarded to the double column periphery where an

offset can be added (V_{bias_sf}) and it is stored in a data buffer. In a final step the signal can be shifted ($V_{offsetOp}$, controlled by $V_{IbiasOp}$; $V_{offsetRO}$, controlled by V_{Ion}) and – in the control and interface block – scaled (V_{Ibias_PH}). The size of the analog signal at the outcome of the ROC is referred to as pulse height.

For calibration an electrical signal (V_{cal}) can be injected and delayed for a certain time ($CalDel$).

The readout of all pixels is organized in two steps, first a fast one (through the comparator) to store the time of a hit and second a slower one (through the sample and hold mechanism) to read the signal height and the pixel address (column and row). For the first one every pixel on a double column sends a current to the periphery, its intensity is adjustable by V_{IColOr} . If more than one pixel is hit in a double column at the same time the currents are added. In the periphery a timestamp is created. The second step is to read out the addresses and the signal heights stored in the sample and hold capacitance and to assign them to the corresponding time stamp.

The pixel address is sent from the pixel unit cell to the periphery as digital current levels and converted there into digital voltage levels, which is needed because of the high data rate and the large distances between many pixel unit cells and the double column periphery. The threshold of this conversion is adjusted by V_{IBias_Bus} . In the control and interface block the components of the address can be shifted (I_{bias_DAC}) before they are joined together with the analog signal. Together they once more can be scaled (V_{Ibias_roc}) and are sent out from the control and interface block.

Different voltages have to be distributed over the ROC. V_{dig} and V_{ana} determine the digital and analog voltages which are used in various positions of the ROC, V_{Comp} regulates the supply voltage of the comparator, and V_{sf} of the sample and hold circuit.

V_{npix} and V_{SumCol} were originally designed to control a chip that organizes a self trigger of the pixel detector which is not used in the CMS experiment. $CtrlReg$, WBC and $RangeTemp$ are registers, i.e. they do not produce an analog voltage.

The TBM [23] is controlled via three DACs. $Dacgain$ stretches the digital TBM levels, $Inputbias$ and $Outputbias$ stretch both the signals of the ROCs and the TBM. Due to the high track density in the two inner layers of the barrel the TBM consists of two parts which – in principle – do the same. Normally only one half of it is used to control a full module (single mode). In the two inner layers of the barrel detector the TBM is operated in the dual mode, each half controlling 8 ROCs.

All DACs are listed and sorted by category in Table 3.1.

Table 3.1: DACs and registers of the pixel modules.

Voltage Regulators	Pixel Unit Cell			Double Column Periphery
	Analog	Trigger	Calibrate	
Vana	Vleak_comp	VIColOr	Vcal	VIbias_bus
Vdig	VwllPr	Vnpix	CalDel	Vbias_sf
Vcomp	VrgPr	VSumCol		VoffsetOp
Vsf	VwllSh			VIbiasOp
	VrgSh			VOffsetRO
	Vtrim			VIon
	VthrComp			
	VhldDel			

Control and Interface Block	Registers	TBM
Ibias_DAC	CtrlReg	Inputbias
VIbias_PH	WBC	Outputbias
VIbias_roc	RangeTemp	Dacgain

4

Optimization Criteria

To simulate an amount of charge inside the sensor a ROC internal signal can be used. It is created through $Vcal$ and delayed by $CalDel$. $Vcal$ is an 8-bit DAC and therefore can be varied between 0 and 255 in a low and a high range. In the former one unit of $Vcal$ corresponds to ≈ 65 electrons (Figure 4.1(a)), in the latter to seven times more or ≈ 455 electrons. If not explicitly mentioned, $Vcal$ is always given in high range DAC units.

The pulse height is measured in ADC units which range from -2048 to $+2047$ for the testboard used to read out a module. One ADC unit corresponds to 0.1275 mV.

4.1 Pulse Height Distributions

A typical behavior of the pulse height as a function of $Vcal$ is shown in Figure 4.1(b). For $Vcal$ between 0 and 12 the signal is below the threshold of the comparator and the pulse height is set to an arbitrary number. Between 12 and 50 the curve is very non-linear. This means that for a specific pulse height (here around -850) a single ionization charge can not be associated as clearly as possible by fitting with a linear function. The influence of this on the position resolution is discussed later. For $Vcal$ between 50 and 120 the pulse height behaves linearly, above 120 it starts to saturate. Though nothing can be done against this saturation, this is not a problem because the percentage of hits with such charges is low.

4.1.1 Linearity in the Low $Vcal$ Range

To quantify the degree of non-linearity in the lower $Vcal$ range the measured pulse height curve is fitted with a hyperbolic tangent function:

$$y = p_3 + p_2 \cdot \tanh(p_0 \cdot x - p_1) \quad (4.1)$$

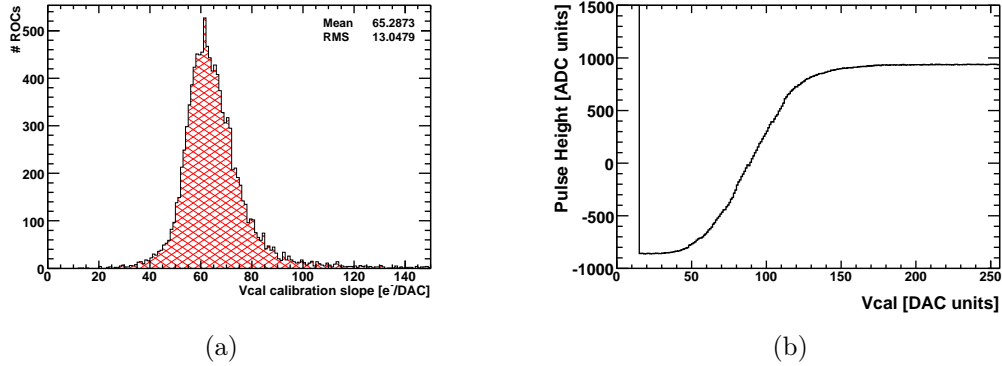


Figure 4.1: Distribution of the number of electrons per $Vcal$ DAC unit (a) and analog pulse height as a function of $Vcal$ (b).

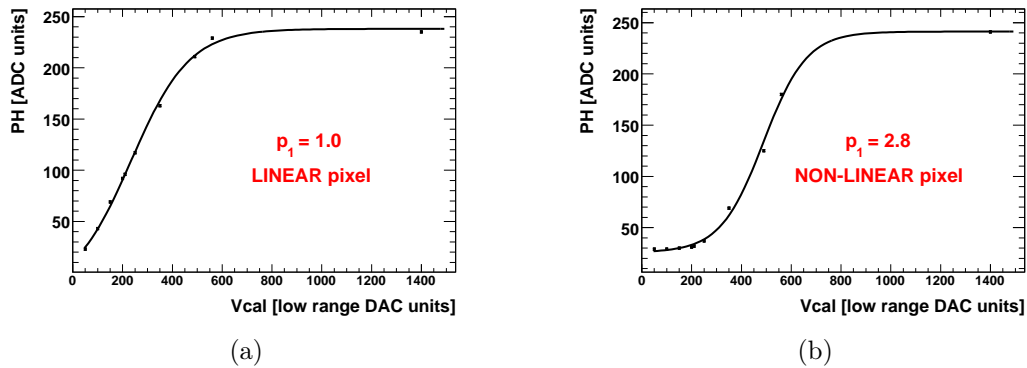


Figure 4.2: Pulse height curves fitted with a hyperbolic tangent function for a linear (a) and a non-linear (b) pixel.

The important parameter of this fit is p_1 , which shifts the curve in the $Vcal$ direction.

As Figure 4.2(a) shows, a value of p_1 around 1 means that the pulse height curve shows an almost linear behavior down to low $Vcal$ values, $p_1 \approx 2.5$ indicates a saturation in the low $Vcal$ range (Figure 4.2(b)). In between the behavior does not vary linearly, already curves with p_1 around 2.0 are strongly curved.

4.1.2 Linearity in the Full V_{cal} Range

Besides the linear behavior in the lower V_{cal} range it is also important to have a linear distribution over a large part of the V_{cal} range and to use all the available ADC range. For quantification the curve is fitted with a polynomial of 5th degree and a tangent through the inflection point in the main region is determined. Then, beginning from the inflection point in both directions, the PH-difference between the tangent and the fit is calculated. The curve is defined to be not linear anymore when this difference exceeds 10 % of the total pulse height range. The linear range is then defined by a quadratic combination of the linear part in V_{cal} direction and the linear part in PH direction as shown in Figure 4.3:

$$\text{linear range} = \sqrt{(\Delta V_{cal})^2 + (\Delta \text{PH})^2} \quad (4.2)$$

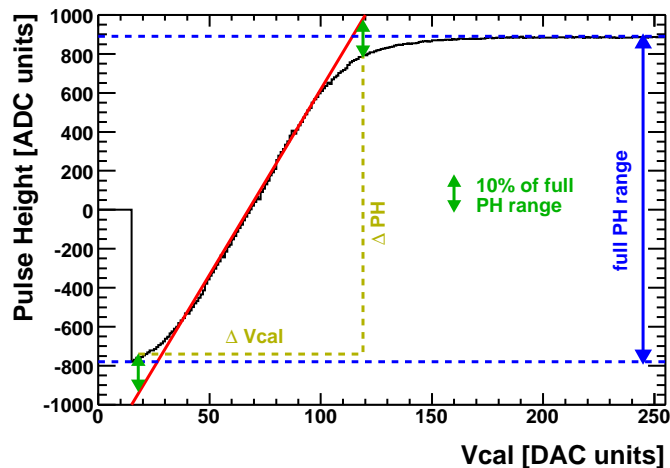


Figure 4.3: Definition of the linear range. The curve is defined to be not linear anymore when the difference between the curve and the straight line exceeds 10 % of the total pulse height range.

4.2 Timewalk

When a signal is compared to a threshold in the comparator the time when it crosses this threshold depends on its amplitude. The time difference between two signals when crossing the threshold is called timewalk and is shown in the upper part of Figure 4.4.

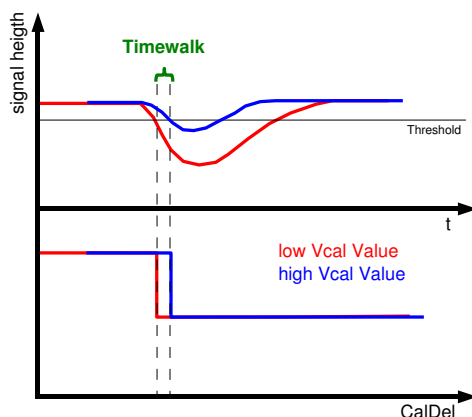


Figure 4.4: Timewalk between two signals with different amplitudes.

To associate all hits of an event to the same bunch crossing it is very important to minimize the timewalk between different ROCs. It is extracted as follows. The pulse height is measured as a function of $CalDel$ for two different $Vcal$ values ($Vcal = 80$ and $Vcal = 250$ in the low range). The signal appears at a lower value of $CalDel$ for the lower $Vcal$ value than for the higher one (compare lower part of Figure 4.4). This difference in $CalDel$ DAC units can be converted into a time difference according to the following formula:

$$\text{timewalk} = 0.45 \text{ ns} \cdot (256 - \Delta_{CalDel} + 30 \text{ ns}) \quad (4.3)$$

A different procedure of measuring the timewalk can be found in [24].

4.3 Address Levels

The output of a whole module consists of a so called TBM header with a length of eight clock cycles to indicate the beginning of a module, three clock cycles for each ROC with no hit, and a TBM trailer with again eight clock cycles at the end of a module. Two characteristic levels in the ADC range are used to structurize it, the ultrablack (UB) at the lowest position of the used ADC range and the black around 0 ADC units. The address of a hit pixel is sent out in five clock cycles, two for the column and three for the row. Six levels are available to encode the address. The TBM header consists of three ultrablacks, one black, and four counter digits, the TBM trailer of two ultrablacks, two blacks, and four status bits [23]. A ROC with no hits only consists of a ultrablack, a black, and a last DAC (which contains

the value of the DAC which was set last). An example for the analog readout of a module where one pixel on ROC 0 has been activated can be found in Figure 4.5.

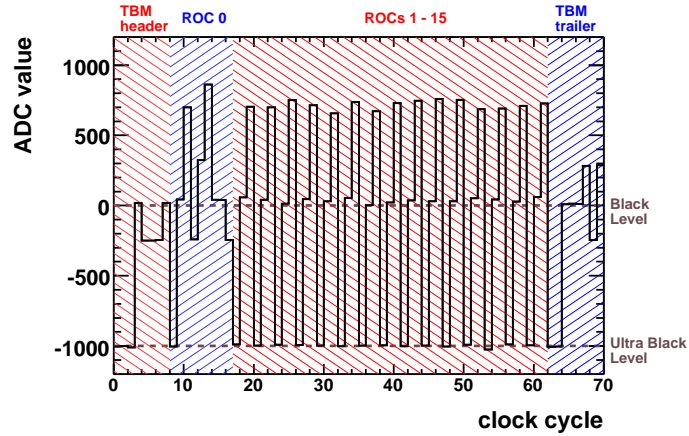


Figure 4.5: Output of a module with one pixel activated on ROC 0.

To exploit the available ADC range as well as possible it is reasonable to have the full pulse height range and all address levels in the same range. Everything should be symmetric around the black level.

5

DAC Setting

5.1 Generally optimized DACs

In terms of optimization the DACs on a ROC can be separated into two main categories. First there are those that are set to the same value on all ROCs of the pixel detector. Some of them are not used at all, but the main fraction of them is optimized once and a broad operational regime same is found. The second category is composed of those DACs which have to be adjusted for every single ROC of the pixel detector individually.

Vdig

Vdig is a 4-bit DAC and is used to regulate the digital voltage of a ROC. Since it does not affect the analog pulse height the only criterion for it is the behavior of the address levels. It is set to 6 since there the amplifier shows a linear behavior and the voltage is below the external voltage (2.5 V).

VNpix and VSumCol

VNpix and *VSumCol* are designed for adjusting the minimum number of hit pixels in a double column and the minimum number of double columns in a self triggering mode of the pixel detector. Since this possibility is not used in the experiment, both of these 8-bit DACs can be set to 0.

VIColOr

The 8-bit DAC *VIColOr* adjusts the amount of current that is sent to the periphery when a token asks for hit pixels in a double column. If more than one pixel is hit the currents are added together. When the ROC is operated in the self triggering mode a threshold on the number of hit pixels per double double column can be set. Therefore it is important to know how large the current per pixel is. Since this mode is not used, it is only important to set the current big enough that a pixel hit is recognized, which is true from 20 on upwards. In the experiment it is set to 99.

Vcal

Vcal has already been described in Chapter 4.

Vleak_Comp

The increasing irradiation of the pixel detector will cause an increased leakage current in the sensor. The 8-bit DAC *Vleak_Comp* controls a circuit, which can compensate for this current. At the startup of the experiment it is set to 0.

VrgPr and VrgSh versus VwllPr and VwllSh

The 4-bit DACs *VrgPr* and *VrgSh* and the 8-bit DACs *VwllPr* and *VwllSh* are designed to be set simultaneously and control the preamplifier/shaper system. Figure 5.1(a) shows the timewalk as a function of those four DACs. Figure 5.1(b) on the other hand shows the pulse height as a function of *VhldDel*. The shape of this curve represents the shape of the analog signal. Since the timewalk should be as small as possible and the pulse height as large as possible a compromise between those two criteria has to be chosen. The chosen DAC settings are $VrgPr = VrgSh = 0$ and $VwllPr = VwllSh = 35$.

VComp

The 4-bit DAC *VComp* regulates the supply voltage of the comparator. In the middle part of its possible range the comparator already works very reliably. Therefore it is set to 10. After irradiation it possibly has to be adjusted.

VhldDel

The 8-bit DAC *VhldDel* should be set in such a way that for different *Vcal* values and different pixels the signal is sampled around its maximum value. Figure 5.2

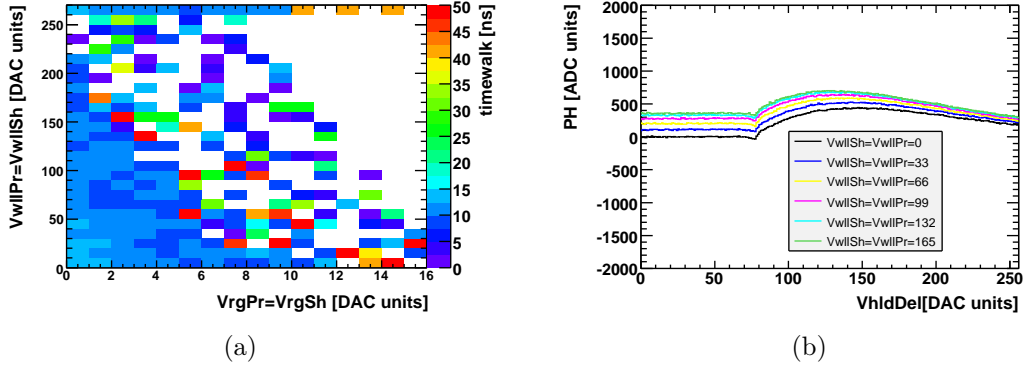


Figure 5.1: Timewalk (a) and pulse shapes (b) as a function of the four preamplifier and shaper DACs. $VrgPr$ and $VrgSh$ are set to the same value. The same is true for $VwllPr$ and $VwllSh$. In (a) the timewalk is decreased from the bottom left to the top right, while it is not reliably measurable any longer.

shows the pulse height as a function of $VhldDel$ for different $Vcal$ values which are given in low range DAC units. The black lines indicate the mean of a complete ROC, the grey bands show the range of all pixels of this ROC.

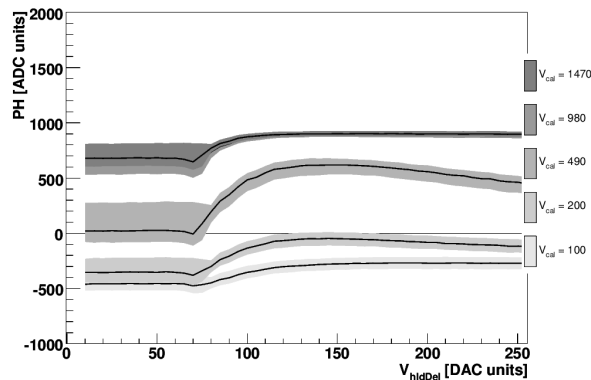


Figure 5.2: Pulse height as a function of $VhldDel$ for different $Vcal$ values.

160 is chosen to be a value which fulfills all the conditions above.

***V*bias_*_*bus**

The addresses of the pixel unit cells are sent to the double column periphery as a current and converted there into a voltage. The threshold of the conversion can be adjusted by the 8-bit DAC *V*bias_*_*bus which is set to 30.

***V*bias_*_*sf**

The 4-bit DAC *V*bias_*_*sf only shifts the pulse height curve. Since *V*offset*Op* is used to do this, *V*bias_*_*sf is set to 10, a value in the medium range of the DAC's proper working region.

V*bias*Op

There is almost a binary influence of the 8-bit DAC *V*bias*Op* on the pulse height curve: below *V*bias*Op* \approx 20 there is no signal seen for the whole *V*cal range, above this value, the shape of the pulse height curve does not change at all. Therefore the setting can be done more or less arbitrary, *V*bias*Op* = 50 is chosen.

***V*lon**

The 8-bit DAC *V*lon has a stretching influence on the pulse height curve. Since the pulse height range is adjusted by *V*bias_*_*PH, it is set in the middle region: *V*lon = 130.

***V*bias_*_*roc**

The influence of the 8-bit DAC *V*bias_*_*roc is to stretch the address levels and—like *V*bias_*_*PH—to stretch the pulse height curve. Since *V*bias_*_*PH is optimized, *V*bias_*_*roc is set close to its maximum to keep all possibilities of adjustments.

Inputbias and Outputbias

Both *Inputbias* and *Outputbias* are 8-bit TBM DACs which have no influence on the pulse height curve if they are above a certain threshold, which lies around 110. Both are set above this threshold to 128.

5.2 Dynamically optimized DACs

Several DACs on the ROC have a big influence on its behavior, for example on the functionality or on the pulse height linearity. Their best setting varies quite strongly

from ROC to ROC. Therefore they are dynamically adjusted for every single ROC. To determine the precision with which DAC can be set, each optimization is repeated under the same conditions and the RMS of those measurements is taken.

Dacgain

The TBM 8-bit DAC *Dacgain* only has an influence on the analog levels of the TBM. Therefore it is the ideal candidate to set the ultrablack level of the TBM to a user-defined value, -1000 here. It is adjusted in such a way that the ultrablacks of both channels of the TBM differ least from the target value, but lie below it. Since the position of the different levels is symmetric around the black level and can not be shifted but only be stretched, this also fixes the position of all other levels, in particular the one of the highest TBM level to $+1000$ in this case.

Ibias_DAC

Ibias_DAC is an 8-bit DAC and has almost only an influence on the ROC levels. The little shifting influence on the pulse height can be ignored since this is adjusted anyway in a later step. It is used to set the ultrablack of all ROCs to the same value as the TBM ultrablack. In the same way as for the TBM this also fixes the position of the ROC address levels. *Ibias_DAC* can be set with a precision of 0.73 DAC units.

Vana

The 8-bit DAC *Vana* is set in such a way that the analog current drawn per ROC is 24 mA. The analog current of a module when *Vana* is changed on one ROC is shown in Figure 5.3 for -10°C and $+17^{\circ}\text{C}$. It strongly depends on the temperature. At -10°C an analog current of 0.56 mA is drawn for $Vana = 0$ and a slope of $-6.1 \times 10^{-2}\text{A}/\text{DAC unit}$ is measured; at $+17^{\circ}\text{C}$ an analog current of 0.54 mA is drawn for $Vana = 0$ and a slope of $-5.0 \times 10^{-2}\text{A}/\text{DAC unit}$ is measured. *Vana* can be set with a precision of 0.55 DAC units.

VthrComp versus CalDel

All ROCs only work in a specific region of the *VthrComp* - *CalDel* range. To measure this region, *Vcal* is set to 200 in low range DAC units (this was found to be a good setting for many tests in [25]), five calibrate signals are sent for each pair of *VthrComp* and *CalDel*, and the number of readouts is counted. Since the working range does not change very strongly from pixel to pixel on the same ROC,

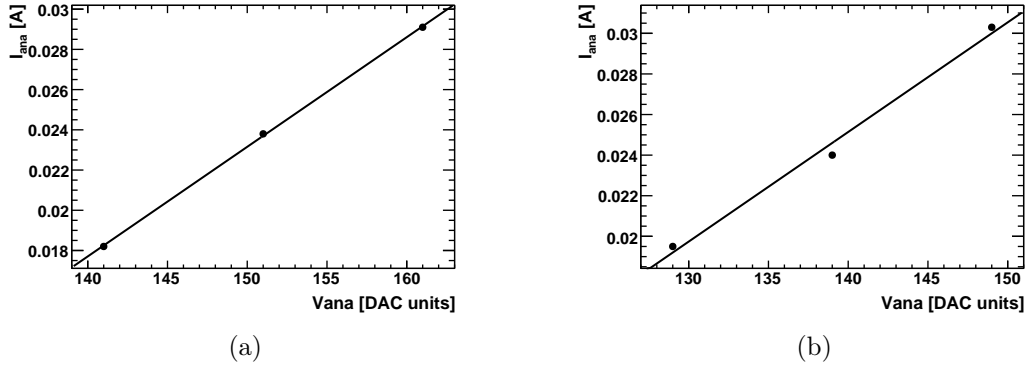


Figure 5.3: Dependency of the analog current on $Vana$ for the same ROC for -10°C (a) and $+17^\circ\text{C}$ (b).

this procedure is only done for one single pixel. A typical shape of the valid readout area is shown in Figure 5.4.

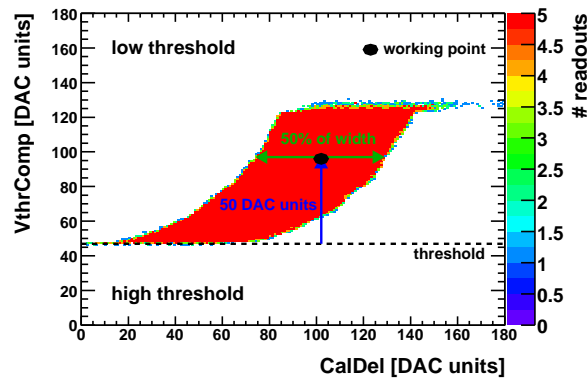


Figure 5.4: Procedure of finding a stable working point in the $VthrComp$ - $CalDel$ space.

The used values for this DAC pair should lie as far away as possible from the edges of the readout area. To find such a point in a first step the minimal value of $VthrComp$ where a signal appears (horizontal line in Figure 5.4) is determined. From this point $VthrComp$ is increased by 50 units and $CalDel$ is established in the middle of the readout range. This pair of DAC values is defined as the working point for calibration purpose. For the trimming of a ROC, $VthrComp$ is set in a different

way. *CalDel* can be set with a precision of 0.53 DAC units.

VIbias_PH

An important criterion of the DAC optimization is that the pulse heights and digital levels of all ROCs lie inside the same ADC range. In case of the levels this goal is already reached by setting the TBM and ROC ultrablack levels to a specific value. The only adjustment remaining is the one of the pulse heights, which should fill the target ADC range. The general idea behind this procedure is first to stretch or squeeze the pulse height range with one DAC and shift it afterwards to the desired region.

With the 8-bit DAC *VIbias_PH* the complete pulse height curve can be stretched as shown in Figure 5.5. Since this DAC has no influence on any address levels at all it is the optimal candidate to stretch or squeeze the size of the pulse height range to the favored one, 2000 (from -1000 to $+1000$) in this case. To set it, the lowest *Vcal* value is searched for which a pulse height is measurable and the difference to the pulse height for $Vcal = 255$ is computed. *VIbias_PH* is adjusted until this difference equals 2000. It can be set with a precision of 0.52 DAC units.

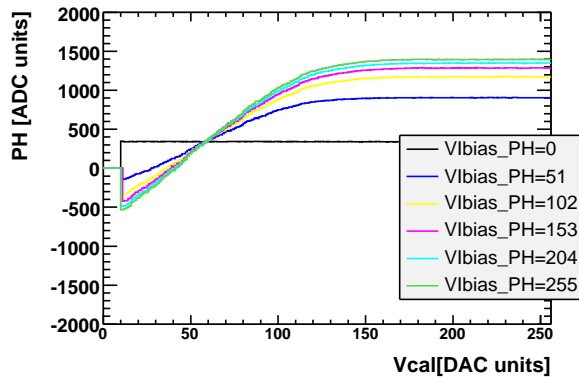


Figure 5.5: Influence of *VIbias_PH* on the pulse height curve.

Two DACs that only shift the pulse height curve and also have no influence on any address levels at all are *VoffsetOp* and *VoffsetR0*. Since they are correlated, they are first discussed before coming back to the adjustment of the pulse height range.

VoffsetOp versus VOffsetR0

$VoffsetOp$ and $VOffsetR0$ are both 8-bit DACs which shift the pulse height curve and have an influence on the linear range. The correlation between them is shown in Figure 5.6. It can be seen that for $VOffsetR0 > 100$ any linear range can be achieved by setting $VoffsetOp$ correctly. Since the band with the highest linear range is shifted for different temperatures (up for lower and down for higher temperatures) and different pixels, $VOffsetR0$ is set to 120 and $VoffsetOp$ is adjusted afterwards. It can be set with a precision of 0.41 DAC units.

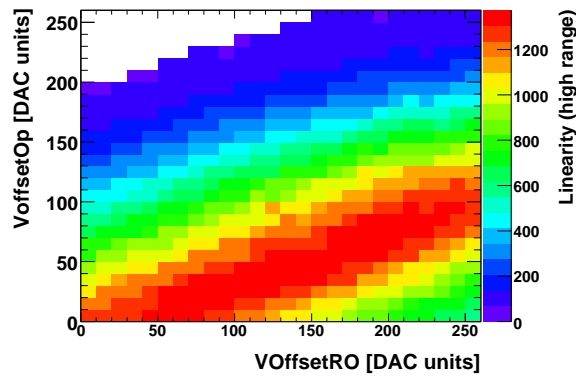


Figure 5.6: High range linearity in dependency of $VoffsetOp$ and $VOffsetR0$ for $+17^{\circ}\text{C}$. The greatest linear range is reached for the dark (red) band at the bottom of the plot. For -10°C the band is shifted upwards.

While the absolute value of the pulse height range is already adjusted with $Vbias_PH$, $VoffsetOp$ can now be used to shift the pulse height curve in the target ADC range. Since the variation of $VoffsetOp$ also influences the pulse height range a little bit and $Vbias_PH$ has a small influence on the position inside the ADC range, the procedure of adjusting those DACs needs to be repeated on average three times.

Vsf

The 8-bit DAC Vsf is the crucial DAC to get a linear behavior of the pulse height in the low $Vcal$ range. The higher it is the more linear the pulse height curve becomes, as shown in Figure 5.7(a). However, the digital current of the ROC rises with increasing Vsf . Its absolute value depends on the difference between $Vana$ and Vsf , whereas the former is already adjusted and is not changed at this point anymore.

The total digital current of a module as a function of V_{sf} of one ROC is shown in Figure 5.7(b).

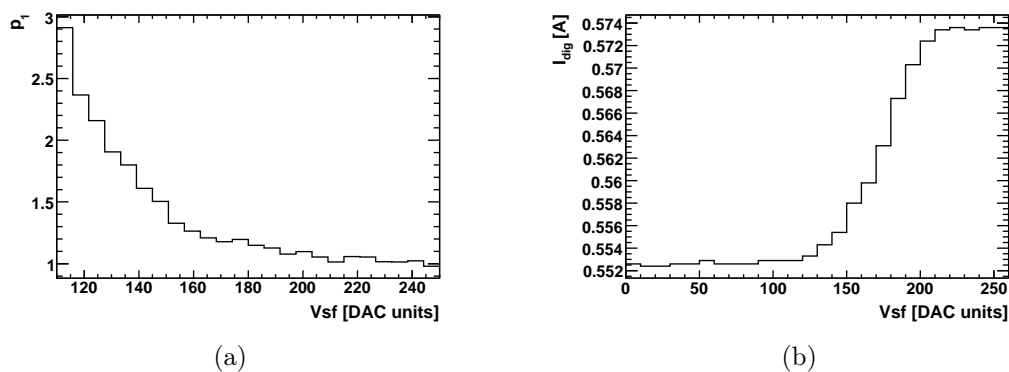


Figure 5.7: Influence of V_{sf} on the linearity of a pixel (a) and on the digital current of a module, V_{ana} fixed (b). For (b), V_{sf} is changed only on one ROC

The value of V_{sf} where the current starts to rise significantly is very chip dependent because V_{ana} also varies from ROC to ROC. Besides the dependency on V_{sf} the linearity of the pulse height curve strongly depends on the temperature.

As discussed in Chapter 4.1.1 the (non-) linearity of a pixel can be quantified by fitting its pulse height curve with a hyperbolic tangent function. The parameter p_1 of this fit is an indication for the linearity. To adjust V_{sf} it is increased in steps of five until this parameter is smaller than 1.4; if the increase of the digital current between $V_{sf} = 0$ and the present setting is below 5 mA this setting is used, otherwise V_{sf} is lowered until the current increase is smaller than 5 mA.

This optimization is done for an average pixel in terms of linearity. V_{sf} can be set with a precision of 0.9 DAC units, while it is set in steps of 5 DAC units to speed up the procedure.

VthrComp versus Vtrim

The optimization of the 8-bit DACs V_{trim} and $V_{thrComp}$ is part of the trimming. It is used to unify the threshold of all pixels of a ROC for which four trim bits can be set per pixel. A detailed description of the procedure can be found in [25]. Here only a rough description is given.

- Measure the $V_{thrComp}$ threshold for a fixed V_{cal} value (here: $V_{cal} = 60$, target threshold)

- Set $VthrComp$ to the minimum value of this distribution
- Measure the $Vcal$ threshold for each pixel of a ROC
- Take the pixel with the highest threshold
- Turn all trim bits on and increase $Vtrim$ until the threshold reaches the target value

$VthrComp$ can be set with a precision of 0.65 DAC units.

5.3 Registers

Besides the DACs there are three registers on each ROC which are used to change between different operational states.

- $RangeTemp$ is used to switch between different ranges of the ROC internal temperature sensor.
- $CtrlReg$ allows to switch between high and low $Vcal$ range, full speed (40 MHz) and half speed and to disable a whole ROC.
- WBC sets the bunch crossing in which data is read out.

6

Setting Verification

Several criteria can be investigated to check that all the optimizations are really successful. Those are on the one hand ROC specific parameters but on the other hand also reconstruction specific parameters, especially position resolutions. The latter ones are determined in a CMSSW simulation.

6.1 P_1 Distributions

Figure 6.1(a) shows the distribution of p_1 before and after the optimization of V_{sf} . Almost all non-linear pixels are removed and the distribution is much more uniform. The influence of the optimization on the digital current is shown in Figure 6.1(b). The average digital current is only increased by 40 mA or 9%.

6.2 ADC Range Utilization

To verify that the complete output of a ROC lies within the target ADC range from -1000 to $+1000$ Figure 6.2 shows the outputs of all ROCs where one pixel is activated on each ROC. Sequentially the ultrablack, the black, the last DAC, and the five address levels are shown. The last bin contains the minimal and maximal value of a pulse height curve. It can be seen that both the ultrablack and the black are centered around their target values of -1000 and 0 , respectively. The highest address level is centered around $+1000$, the others are well separated and distributed over the ADC range. The maximal value of all pulse heights lies perfectly at $+1000$, while the minimal value is distributed over a broader range since the measurement is done close to the threshold here.

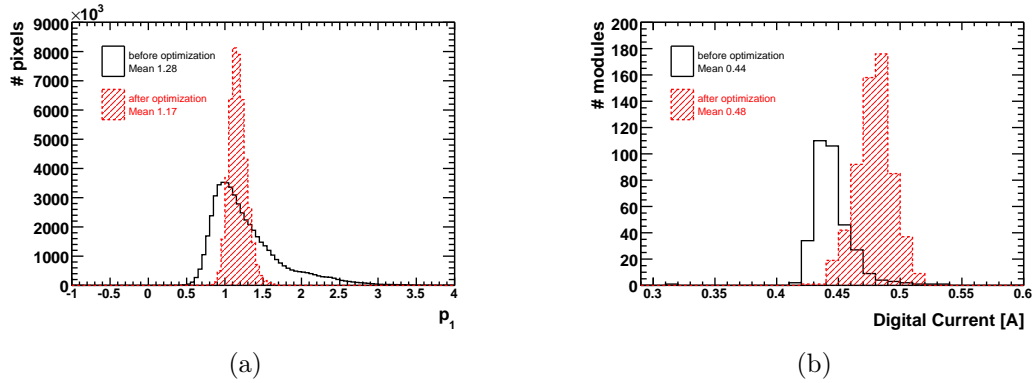


Figure 6.1: Distribution of p_1 (a) and the digital current per module (b) before and after the optimization of p_1 .

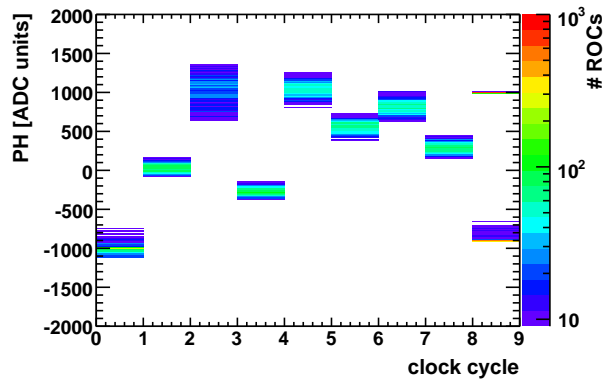


Figure 6.2: Outputs of all ROCs where one pixel is activated on each ROC.

6.3 Position Resolutions

To investigate the influence of the non-linearity a simulation using CMSSW_1_2_0 is done. 10000 muons with a transverse momentum of $p_t = 10$ GeV are generated in two ranges of pseudorapidity, $-0.1 < \eta < 0.1$ (central barrel region) and $1.8 < \eta < 2.0$ (forward barrel region). For both ranges the same pixel response is simulated for all pixels, once a linear response and once a non-linear response. Both the linear and the non-linear response are reconstructed with a linear and an area tangent hyperbolic function. Afterwards a comparison between different combinations of responses and calibrations in $r\varphi$ - and z -direction of layer one is done. Furthermore

Table 6.1: Cluster sizes in the central and forward barrel regions with the RMS of their distributions.

	$-0.1 < \eta < 0.1$	$1.8 < \eta < 2.0$
$r\varphi$	2.0 ± 0.7	2.3 ± 1.0
z	1.2 ± 0.6	6.0 ± 1.9
total	2.1 ± 2.2	7.1 ± 2.8

the central and the forward barrel region are compared.

6.3.1 Influence of the Responses and Calibrations

To compare the resolutions for different responses and calibrations the different η -ranges have to be investigated separately since the cluster shapes depend on the pseudorapidity. In the central barrel region ($-0.1 < \eta < 0.1$) the tracks pass the detector layers almost perpendicularly while in the forward barrel region ($1.8 < \eta < 2.0$) only under a few degrees. The resulting cluster sizes are shown in Table 6.1.

Central Barrel Region

(a) *R φ -direction:*

The resolutions of the four combinations of linear and non-linear responses and calibrations and the corresponding deteriorations are shown in Figure 6.3, as an example the distribution is shown for a linear pixel with an area tangent hyperbolic reconstruction in Figure 6.4(a). It can be seen that for a linear pixel $1.3 \mu\text{m}$ in the resolution can be gained when using an area tangent hyperbolic calibration with four parameters instead of a linear one with only two parameters. Using a non-linear pixel instead, the resolution becomes more than 50 % worse for both calibration functions. Therefore it is very important to have all pixels as linear as possible, independent of the used calibration function.

(b) *Z-direction:*

In z-direction the resolution neither depends on the response nor on the calibration. The distribution in Figure 6.4(b) shows a non-Gaussian shape because only a single pixel is hit and there is no Lorentz drift in z-direction. The outliers are wrongly reconstructed hits.

Forward Barrel Region In the forward barrel region the resolution is around $7 \mu\text{m}$ in $r\varphi$ - and around 22μ in z-direction. It neither depends on the response nor on

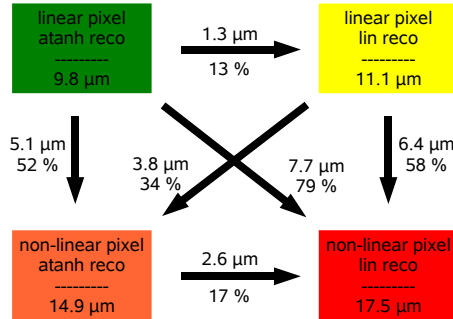


Figure 6.3: Position resolution in $r\phi$ -direction in the central region of the barrel pixel detector. The arrows indicate the degradations between the different methods in absolute values and percentage.

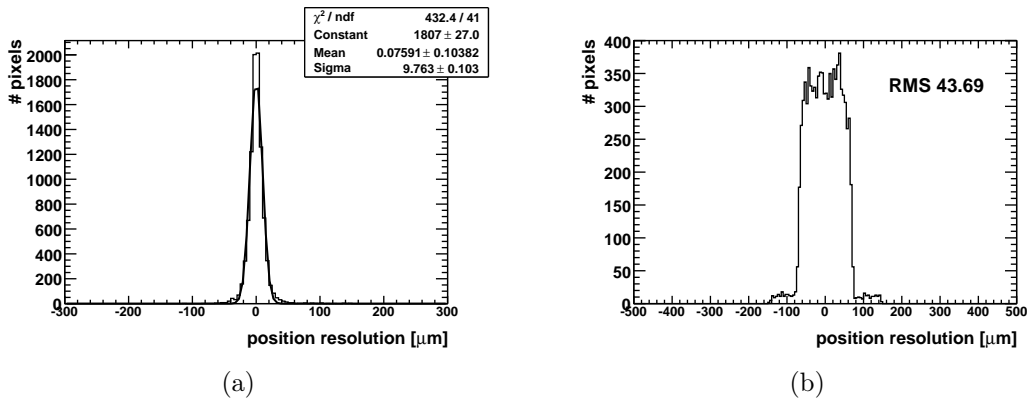


Figure 6.4: Position resolution in $r\phi$ -direction (a) and z -direction (b) in the central region of the barrel pixel detector.

the calibration but is a bit better than in the central barrel region. As an example the resolutions for a linear pixel with an area tangent hyperbolic reconstruction are shown in Figure 6.5(a) and Figure 6.5(b), respectively.

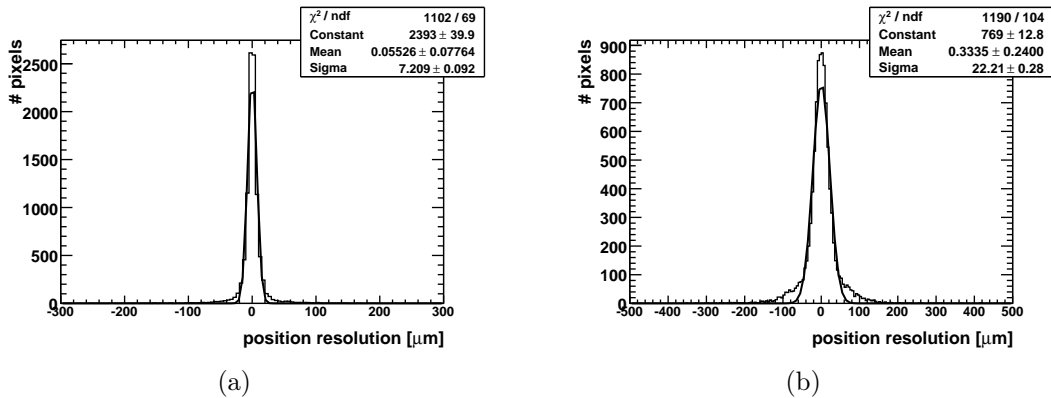


Figure 6.5: Position resolution in $r\varphi$ -direction (a) and z -direction (b) in the forward region of the barrel pixel detector.

6.3.2 Influence of the Pseudorapidity Range

To further investigate the resolution differences between the central and the forward barrel region binary pixel response are simulated. The resolution in $r\varphi$ -direction is $21 \mu\text{m}$ in the central and $7 \mu\text{m}$ in the forward barrel region. The value in the central barrel region is roughly as large as expected, the one in the forward direction is much better than expected and comparable to the one with a linear response and area tangent hyperbolic reconstruction. This shows – together with the fact that the resolutions in the central and the forward barrel region differ so much – that the resolution in forward direction is dominated by the shape of the hit clusters, which are longish there. It is influenced by the length of the cluster and by the ratio between the number of hit pixels in two rows (compare Table 6.1).

6.3.3 Influence of the Trimming

The influence of the trimming uniformity on the position resolution is also investigated. Therefore the threshold in the CMSSW simulation is set to the nominal value of 2500 electrons and smeared by a Gaussian distribution centered at 0 and characterized by the width σ ; the noise is switched off in the simulation. Figure 6.3.3 shows the position resolutions in the central and the forward barrel region in $r\varphi$ - and z -direction as a function of threshold uncertainty σ . For realistic values of the order of a few hundred electrons no influence on the position resolution can be seen. This is also true for the central barrel region. A little influence is only seen in the forward barrel region and z -direction for the completely unrealistic threshold uncertainty of 2500 electrons.

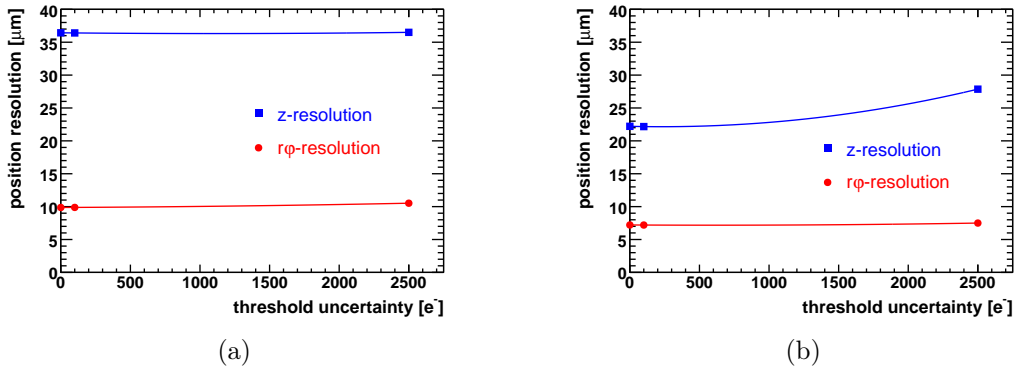


Figure 6.6: Influence of the threshold uncertainty (not the mean of the threshold) on the position resolution in the central (a) and forward (b) barrel region.

6.3.4 Influence of the Uniformity of the Calibration

In the last step of investigating various influences on the position resolution different responses of all the pixels are applied. To use realistic results, measurements from the module testing [25] are used. The pulse height curves of about 25 million pixels are fitted with Equation 4.1 and the average values and deviations of all four fit parameters are extracted. In the simulation of the pixels a response according to those values is used, while in the calibration the average value is used in the area tangent hyperbolic function. The results are shown in Table 6.2.

It can be seen that a per ROC instead of a per pixel calibration causes - except for the z-direction in the central barrel region - a big degradation of the resolution. Since the fit parameters are correlated, a study has been done where the four parameters of all pixels are taken from the module testing results [26]. The investigation concludes that there is no measurable difference between using average parameters and extracting each parameter separately. This is valid for both an absolute change of the threshold and a variation in the threshold uncertainty.

Table 6.2: Position resolution for ideally uniform and for realistically distributed pixel responses

Central Barrel Region				
	uniform	realistic	degradation	
$r\varphi$	9.76 μm	15.94 μm	6.18 μm	63%
z	36.53 μm	36.31 μm	-0.22 μm	-1%

Forward Barrel Region				
	uniform	realistic	degradation	
$r\varphi$	7.13 μm	9.43 μm	2.30 μm	32%
z	22.41 μm	33.85 μm	11.44 μm	51%

Part II

Study of the B^0 Lifetime in the Semileptonic Decay Mode

7

B Physics

7.1 Historical Aspects of *B*-physics

In 1960, Yoichiro Nambu formulated the hypothesis that spontaneous symmetry breaking, already well known from condensed matter physics, could also be applied to elementary particle physics [27]. Already one year later, Goldstone formulated his theorem, that the existence of a spontaneously broken continuous symmetry causes the existence of massless scalar particles [28]. As described in Chapter 2.2.1, Peter Higgs and others applied this concept on the gauge fields, where the symmetry is explicitly broken.

In the same year, the CP violation in the neutral kaon system was discovered, which was not understandable at that time [29]. Nine years later, in 1973, Makoto Kobayashi and Toshihide Maskawa came up with an explanation of the CP violation by a mixing of the mass eigenstates and the eigenstates of the weak interaction in the quark sector [30]. Their model predicted a third generation of quarks (or three new quarks, since only the up, the down and the strange quark were known at that time), which is discussed in more detail in the next section. Not much later, in 1974 and 1977, the charm and the bottom quark were discovered [31, 32], while the top quark was only discovered 22 years after its theoretical prediction at the Tevatron [33]. In 2002, CP violation was also found in the neutral B meson system by both B factories BABAR and BELLE [34, 35].

In 2008, Yoichiro Nambu with Makoto Kobayashi and Toshihide Maskawa, received the Nobel prize "for the discovery of the mechanism of spontaneous broken symmetry in subatomic physics" and "for the discovery of the origin of the broken symmetry which predicts the existence of at least three families of quarks in nature", respectively [36].

7.2 The CKM Matrix and *CP* Violation

7.2.1 The CKM Matrix

The idea of Kobayashi and Maskawa was to extend an already existing theory of Cabibbo, saying that the *d* and *s* quark states are not pure flavor eigenstates, but rotated by a mixing angle ϑ_c . His theory had been supported experimentally by a comparison of the semileptonic decay rates of the Σ^- which includes an *s* quark,

$$\Sigma^- \rightarrow n + e^- + \bar{\nu}_e, \quad (7.1)$$

and the strangeless neutron:

$$n \rightarrow p + e^- + \bar{\nu}_e. \quad (7.2)$$

It was found that the decay of the Σ^- , which changes the strangeness by $\Delta S = 1$, was suppressed by a factor of 20 compared to the decay of the neutron with $\Delta S = 0$ [37].

If one includes in this theory not only the three lightest quarks but also the three heavy ones, i.e. introducing a third generation of quarks, this leads to the following relation between the eigenstates of the weak interaction and the mass eigenstates, expressed in the CKM matrix:

$$\begin{pmatrix} d' \\ s' \\ b' \end{pmatrix} = V_{\text{CKM}} \begin{pmatrix} d \\ s \\ b \end{pmatrix} \quad (7.3)$$

with

$$V_{\text{CKM}} = \begin{pmatrix} V_{ud} & V_{us} & V_{ub} \\ V_{cd} & V_{cs} & V_{cb} \\ V_{td} & V_{ts} & V_{tb} \end{pmatrix}. \quad (7.4)$$

Generally, a complex $N \times N$ matrix has $2N^2$ free parameters. From the theoretical point of view, the CKM matrix must be unitary, $\sum_k V_{ik}V_{kj}^* = \delta_{ij}$, which reduces the number of free parameters to N^2 . One phase can be absorbed into each quark field and one phase is unobservable, which leads to $(N-1)^2$ free parameters. In the case of the standard model with three quark generations there are four free parameters, one phase and three mixing angles. To illustrate this, many parametrizations have been proposed, out of which the one of Wolfenstein [38] is the most popular one:

$$V_{\text{CKM}} = \begin{pmatrix} 1 - \lambda^2/2 & \lambda & \lambda^3 A(\rho - i\eta) \\ -\lambda & 1 - \lambda^2/2 & \lambda^2 A \\ \lambda^3 A(1 - \rho - i\eta) & -\lambda^2 A & 1 \end{pmatrix} + \mathcal{O}(\lambda^4), \quad (7.5)$$

with the phase η and the three parameters ρ , A and $\lambda = \sin(\vartheta_c)$.

Since V_{CKM} is a unitary matrix, six vanishing combinations of its matrix elements arise out of which

$$V_{ud}V_{ub}^* + V_{cd}V_{cb}^* + V_{td}V_{tb}^* = 0 \quad (7.6)$$

is the most commonly used one. It can be represented by a triangle in the complex plane which is shown Figure 7.1. Its baseline is normalized to unity because $V_{cd}V_{cb}^*$ is the experimentally best-known value. Its area vanishes if there would be no CP violation.

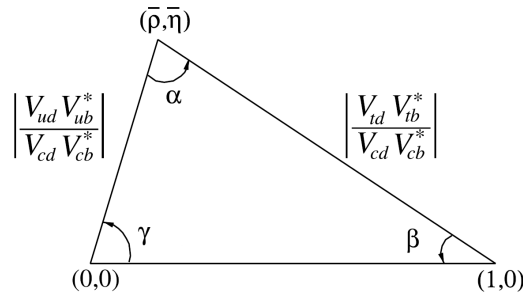


Figure 7.1: The unitarity triangle

7.2.2 CP Violation

As already shortly mentioned, CP violation was first discovered in the decay of the neutral kaon system. Two types of neutral kaons were known, one decaying very fast into two pions and one with a much longer lifetime into three pions. In 1964, James Cronin and Val Fitch discovered the decay of a long living kaon into two pions with a probability of 10^{-3} . Therefore the observed kaons are no CP eigenstates, but mixtures of the real CP eigenstates K_1^0 and K_2^0 called

$$K_S^0 = \frac{1}{\sqrt{1 + \epsilon^2}} (K_1^0 + \epsilon K_2^0) \quad (7.7)$$

$$K_L^0 = \frac{1}{\sqrt{1 + \epsilon^2}} (K_2^0 + \epsilon K_1^0) \quad (7.8)$$

with ϵ being a small parameter that quantifies the amount of CP violation.

This phenomenon could be explained by the theory of Kobayashi and Maskawa about mixing in the quark sector. As mentioned above, a theory with only two quark families results in only one free parameter, namely the Cabibbo angle ϑ_c .

Only with three families, a phase arises that makes CP violation possible. The area in the unitarity triangle is now different from zero.

The theory also predicts that the CP violation is larger in mesons consisting of heavier quarks, e.g. B mesons. This was verified with a high precision in the recent past by the B factories BABAR and BELLE [34, 35].

7.2.3 Experimental Determination of the CKM Matrix Elements

The magnitudes of the CKM matrix elements need to be determined experimentally [39]. For this several measurements can be done. Generally, one can say that the angles of the unitary triangle are determined by measuring CP violating asymmetries and the sides of the unitary triangle are determined by looking at tree level weak decays, flavor oscillations, and loop induced flavor changing neutral currents (FCNC).

In detail this is done in the following way. V_{ud} , which is the same as $\cos(\vartheta_c)$, is determined by the study of nuclear β -decays or by measuring the neutron lifetime. For V_{us} , one uses semileptonic decays of kaons and hyperons, where an s quark turns into an u quark by emitting a W boson, which decays into a lepton pair. The matrix element V_{ub} is determined by looking at semileptonic decays of B mesons to non-charmed particles. This is quite difficult, because the decay of a b quark to the two generations lower u quark is rare and overwhelmed by the much more frequent decay of a b to a c quark. This background can be reduced by requiring the lepton of the W decay to have $p > 2.3$ GeV in the restframe of the B , which is the kinematic limit in the decay $B \rightarrow D\ell\nu X$. This is the decay that is used to determine V_{cb} in an inclusive and exclusive way. For the determination of V_{cd} , neutrino beams are used and the ratios of double-muon production ($\nu_\mu + d \rightarrow u + \mu^-$) and single-muon production ($\nu_\mu + d \rightarrow c + \mu^-$, $c \rightarrow s + \mu^+ + \nu_\mu$) are compared. V_{cs} is determined using the decay $D^+ \rightarrow \bar{K}^0 e^+ \nu_e$ and the D production of $s\bar{s}$ sea quarks. For V_{td} and V_{ts} , effects of virtual top quarks in the $B_{(s)}^0 \bar{B}_{(s)}^0$ mixing are used.

The current status of the CKM matrix elements is shown in Equation 7.9, a graphical overview of the unitary triangle using these results in Figure 7.2, where Figure 7.2(b) shows an enlarged view of Figure 7.2(a).

$$V_{\text{CKM}} = \begin{pmatrix} 0.97383 \pm 0.00024 & 0.2272 \pm 0.0010 & 0.00396 \pm 0.00009 \\ 0.2271 \pm 0.0010 & 0.97296 \pm 0.00024 & 0.04221 \pm 0.00045 \\ 0.00814 \pm 0.00048 & 0.04161 \pm 0.00045 & 0.999100 \pm 0.000019 \end{pmatrix} \quad (7.9)$$

Until today, it is not understood why the weak interaction violates P maximally but CP only so little. Also an open question is if $V_{\text{CKM}}^\dagger V_{\text{CKM}} = \mathbb{1}$, i.e. if the unitary

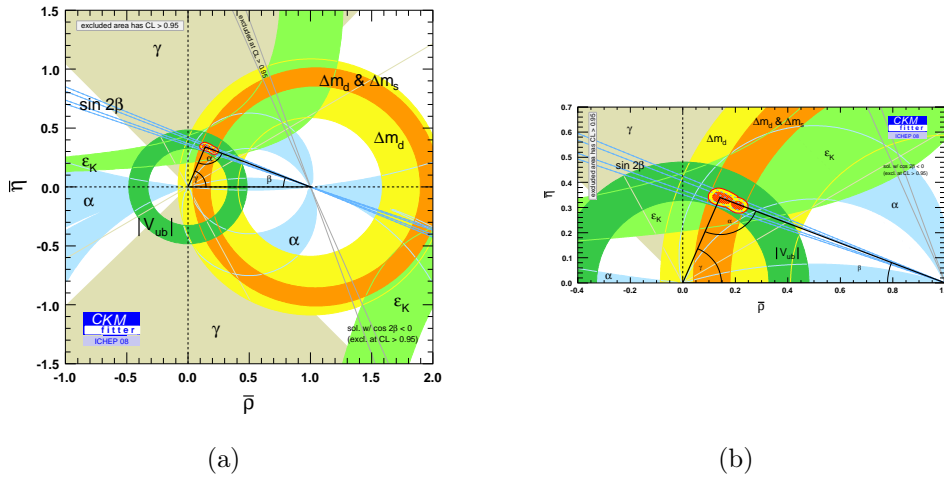


Figure 7.2: Current result of the global CKM fit in a (a) large and (b) zoomed $\bar{\rho}\bar{\eta}$ plane.

triangle is really closed.

7.3 B Mesons

B mesons are particles consisting of a \bar{b} and a lighter quark held together by the strong force. The antiparticle of each B meson is composed of a b quark and the corresponding anti-quark. In the following, charge conjugation is always included when mentioning B mesons. The neutral B mesons have the possibility to transform into their antiparticle, which is called flavor oscillation or mixing. An overview over the ground states of B mesons and some of their properties is given in Table 7.1 [39].

Table 7.1: Properties of B mesons.

meson	quark content	mass [MeV]	lifetime [ps]
B^+	$\bar{b}u$	5279.0 ± 0.5	1.638 ± 0.011
B^0	$\bar{b}d$	5279.4 ± 0.5	1.530 ± 0.009
B_c^+	$\bar{b}c$	6286 ± 5	0.46 ± 0.17
B_s^0	$\bar{b}s$	5367.5 ± 1.8	1.466 ± 0.059

A quite large fraction of *B* mesons decay by a transition of the *b* quark to a lighter quark and a *W* boson: $b \rightarrow qW$ and the *W* decaying to a quark or lepton pair. The Feynman diagram of the decay, when assuming the *W* turning to $l\nu$ and treating the *b* as a free quark and the lighter quark as a spectator, is shown in Figure 7.3.

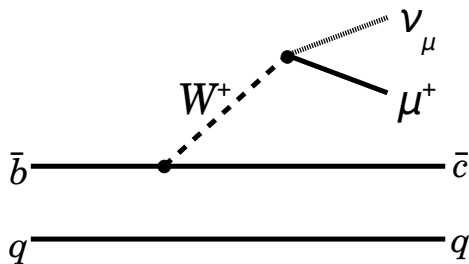


Figure 7.3: Feynman diagram of a semileptonic *B* meson decay.

In this simple spectator model, all *B* mesons have identical lifetimes and the *b* decay width in analogy to the muon decay is given by

$$\Gamma(b \rightarrow ql\nu) = \frac{\mathcal{B}(b \rightarrow ql\nu)}{\tau_B} = \frac{G^2 m_b^5}{192\pi^3} |V_{qb}|^2 f. \quad (7.10)$$

Here f is already a correction factor for the fact that the *b* quark is not free but bound in a meson and that the phase space is reduced compared with that for massless products [37]. Since the mass of the *b* quarks is small compared to the mass of the *W* boson, here also the weak coupling constant g can be replaced by the Fermi constant G . The fact that the second quark interacts, contributes to the lifetime differences of the various *B* mesons.

7.3.1 Lifetimes of *B* Mesons

By looking at the CKM matrix in the Wolfenstein parametrization in Equation 7.5, the hierarchical structure in the probabilities of quark transitions can be seen. Since λ is a small number, the diagonal elements, representing the probabilities of transitions within one generation, are close to one (compare numerical values of the CKM matrix in Equation 7.9). The elements of the secondary diagonals represent the transitions between one quark generation and the next. They are much smaller, meaning that the probability of a transition of a quark into one of the neighbor

family is much lower. The probability of a quark of the third generation directly decaying into one of the first generation is very low and given by the CKM matrix elements on the top right and bottom left.

Since the b quark is only allowed to decay into quarks of lower generations (due to the higher mass of the top quark, the transition within the third generation is forbidden), B mesons have relatively long lifetimes in the order of pico seconds. Those long lifetimes result in long mean flight paths and therefore a significant separation between the primary vertex and the B decay vertex. With the CMS pixel detector, this vertex can be resolved with a high precision (see Chapter 10.6.2).

7.3.2 Heavy Flavor Production

At a hadron collider like the LHC, where composite objects like protons collide with each other, there is a big variety of heavy flavor production processes [40] since the incoming protons are made of many different quarks and gluons. Those processes can be grouped into three categories, explained in the following.

- **Pair Creation** This is the leading order production process, where either two gluons (Figure 7.4(a)) or two quarks (Figure 7.4(b)) of the colliding protons directly produce two heavy flavor quarks Q . The two quarks are back-to-back.

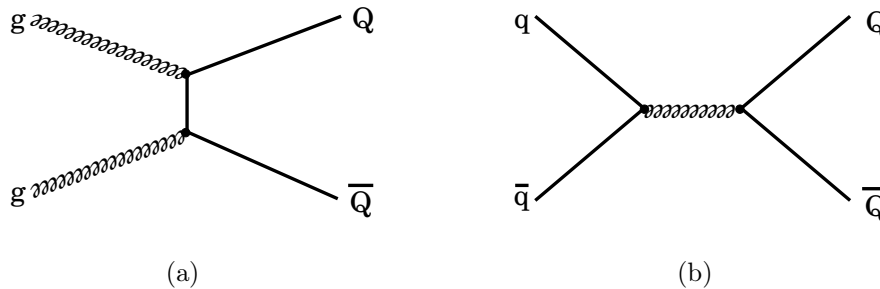


Figure 7.4: Pair Creation as the leading order heavy quark production processes in gluon-gluon fusion (a) and quark-antiquark fusion (b).

- **Flavor Excitation** An off-shell heavy flavor quark from one of the colliding protons is put on-shell by scattering with a quark or gluon of the other incoming proton. This process is illustrated in Figure 7.5(a). The emitted heavy flavor quarks do not have to be back-to-back.

- **Gluon Splitting** This process happens when one of the gluons from the hard scattering process splits into two heavy flavor quarks as shown in Figure 7.5(b). The two quarks can be emitted with only a small angular separation.

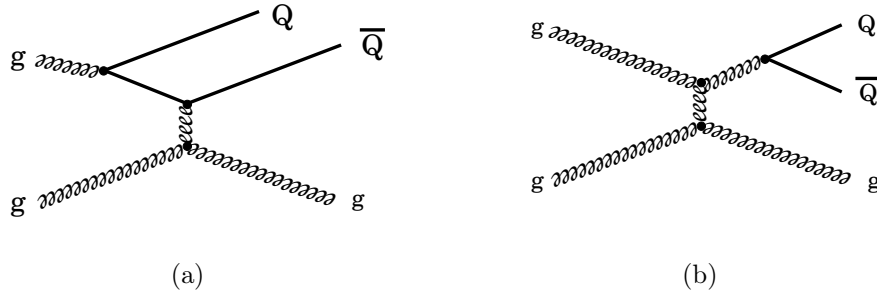


Figure 7.5: Heavy quark production by flavor excitation (a) and gluon splitting (b).

The total $b\bar{b}$ cross section is about $\sigma_{b\bar{b}} = 500 \mu\text{b}$. Once a $b\bar{b}$ quark pair is produced, one or both hadronize to form B mesons. For a B^0 , this happens with a probability of $(39.8 \pm 1.0)\%$ [39].

7.3.3 The B^0 Decay

In this work, the lifetime of the B^0 meson is measured using the following decay chain (final state particles are marked in red and underlined).

$$\begin{aligned}
 B^0 &\rightarrow D^{*-} \underline{\mu^+ \nu_\mu} \\
 &\quad \downarrow \underline{\bar{D}^0 \pi_s^-} \\
 &\quad \quad \downarrow \underline{K^+ \pi^-}
 \end{aligned}
 \tag{7.11}$$

As mentioned above, the B^0 meson propagates a certain distance before decaying into a D^{*-} , a positive muon and muon-neutrino. The D^{*-} decays instantaneously into a \bar{D}^0 and a slow pion. This pion is called slow because of its low momentum (further details on this below). The \bar{D}^0 again flies a certain distance before decaying into a positively charged kaon and a negatively charged pion. A graphical illustration as well as the associated Feynman diagrams are shown in Figure 7.6 and Figure 7.7, respectively.

With the branching ratios for the single decay steps [39] quoted in Table 7.2, in total 0.138% of the produced B^0 mesons decay in the chain mentioned in Equation 7.11. The decay products of this chain that can be measured in the detector

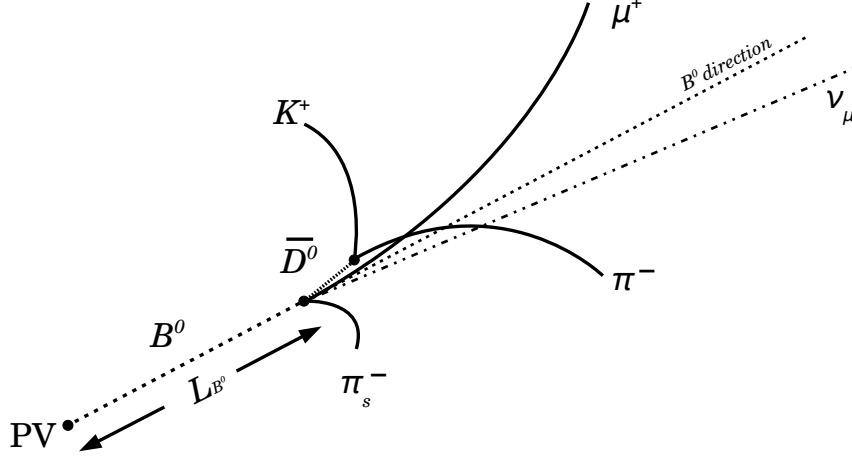


Figure 7.6: Decay topology of $B^0 \rightarrow D^{*-} \mu^+ \nu_\mu$ with $D^{*-} \rightarrow \bar{D}^0 \pi_s^-$ and $\bar{D}^0 \rightarrow K^+ \pi^-$.

are the positively charged muon, the negatively charged slow pion, and the negatively charged pion. The neutrino can not be measured in the detector. It should be pointed out that there is a charge correlation between these final state particles, which can be used for the reconstruction of the decay.

Table 7.2: Branching ratios for the different steps of the B^0 decay chain.

decay	$\mathcal{B}[\%]$
$B^0 \rightarrow D^{*-} \mu^+ \nu_\mu$	5.35 ± 0.20
$D^{*-} \rightarrow \bar{D}^0 \pi_s^-$	67.7 ± 0.5
$\bar{D}^0 \rightarrow K^+ \pi^-$	3.8 ± 0.07
total	0.138 ± 0.006

Some masses of particles involved in the signal decay are given in Table 7.3. The proper decay time of the B^0 meson is given by the following equation:

$$c\tau = \frac{L_{B^0}}{\beta\gamma} = L_{B^0} \cdot \frac{M_{B^0}}{|\vec{p}(B^0)|}, \quad (7.12)$$

with L_{B^0} being the decay length of the B^0 meson, β and γ the usual relativistic factors and $p(B^0)$ the B^0 momentum.

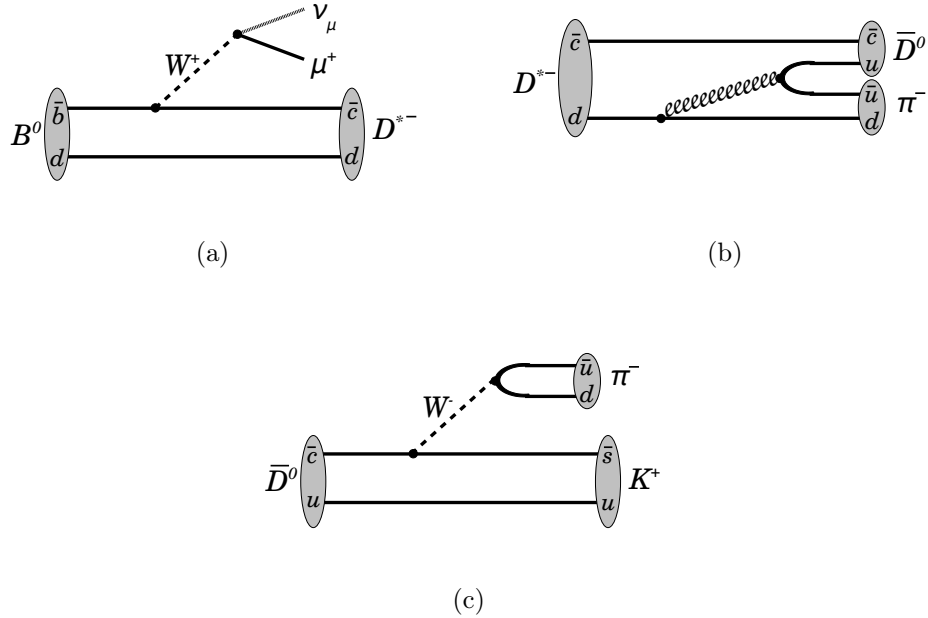


Figure 7.7: Feynman diagrams for the decays $B^0 \rightarrow D^{*-} \mu^+ \nu_\mu$ (a) $D^{*-} \rightarrow \bar{D}^0 \pi^-$ (b) and $\bar{D}^0 \rightarrow K^+ \pi^-$ (c).

Table 7.3: Some masses of particles involved in the signal decay.

particle	mass
D^*	$2.010 \text{ GeV}/c^2$
D^0	$1.8645 \text{ GeV}/c^2$
π	$139.57 \text{ MeV}/c^2$

This means that both the decay length and the full momentum of the B^0 meson need to be measured to determine the lifetime. The precision of the decay length measurement is only limited by the detector resolution, but for the momentum measurement there is an irreducible information loss due to the neutrino that cannot be detected. To account for this missing neutrino, commonly a so-called k -factor method is used. In this analysis, a new approach of reconstructing the neutrino and therefore also of the full momentum of the B^0 is applied. More details on this follow in the next chapter.

8

The Neutrino Reconstruction Method

8.1 Motivation

Generally it is considered that the decay of a particle, where one of the final state products is not detected (e.g. a neutrino), can not be fully reconstructed. There are a few well known exceptions.

- If the momentum of the decaying particle is known and all but one of the decay products are detected and reconstructed, then, obviously, it is possible to determine the missing particle's 4-momentum.
- If the detector is very hermetic, the missing energy can be measured sufficiently well.
- If the direction of the decay products is almost the same as the one of the decaying particle, the collinear approximation leads to reasonable resolutions [41].

For the semileptonic decays of B^0 mesons within the CMS detector, none of the above condition is fulfilled. Therefore, in a conventional analysis, the so-called k -factor method would be used.

8.2 The k -Factor Method

The proper time of the B^0 meson is given by Equation 7.12 and requires the knowledge of the full B^0 momentum. Since this is not given, due to the missing neutrino, one uses the combination of all visible decay products instead:

$$p(D^*\mu) = p(K^+) + p(\pi^-) + p(\pi_s^-) + p(\mu^+) \quad (8.1)$$

For the momentum of the B^0 meson one then gets

$$|\vec{p}(B^0)| = \frac{|\vec{p}(D^*\mu)|}{k} \quad (8.2)$$

with the k -factor estimated from Monte Carlo (MC) simulations. This results in the proper time:

$$c\tau = L_{B^0} \cdot \frac{M_{B^0}}{|\vec{p}(D^*\mu)|} \cdot k \quad (8.3)$$

A distribution of the k -factor (obtained from the decay in Equation 8.23) is shown in Figure 8.1. Applying the mean value of this distribution to every single reconstructed event introduces a significant error on the B^0 momentum in this event and, hence, on the proper time as well. To reduce the error by an average k -factor, it is calculated in bins of $m_{D^*\mu}$. For each bin, the mean value of the k -factor distribution is taken and applied to those reconstructed events inside the particular $m_{D^*\mu}$ bin. This indeed reduces the spread, but the single B^0 momentum is still not known as well as possible.

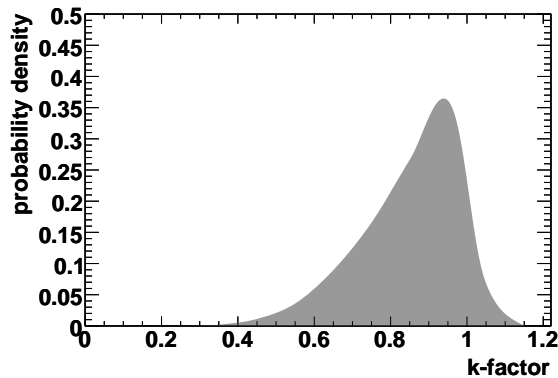


Figure 8.1: Probability density for the k -factor obtained from the decay in Equation 8.23.

8.3 Kinematics of B^0 Decays

To not depend on MC information and average values, the topological information from the B^0 decay can be used. For this, the decay vertex of the B^0 meson is a crucial input parameter. Due to the high hit resolution of the CMS pixel detector, this can be resolved very well. With this reconstruction method, the neutrino 4-momentum can be reconstructed up to a twofold ambiguity.

Since the detectable B^0 decay products can be treated as a single particle, the decay of the B^0 meson is a “two-body-decay” into the $D^*\mu$ system and the neutrino. Such a decay happens in only two space dimensions, one of which (the B^0 flight direction \vec{V}_B) is labeled with \parallel , and the other one (\perp) is defined in the plane spanned by the two vectors $\vec{P}_{D^*\mu}$ and \vec{V}_{B^0} and is orthogonal to the B^0 flight direction as shown in Figure 8.2.

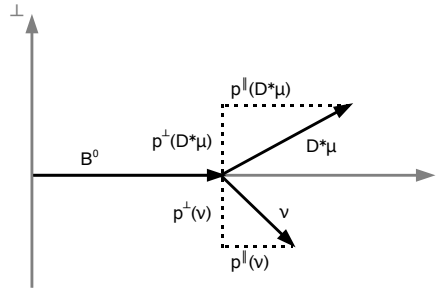


Figure 8.2: The B^0 decay into the $D^*\mu$ system and the neutrino in two dimensions.

Since the neutrino is assumed to have zero mass, there are only two unknown quantities left, namely its momentum components in the \perp and the \parallel directions. For momentum conservation reasons, the \perp component of the neutrino momentum must be of equal magnitude and opposite sign to the one of the $D^*\mu$ system ($\vec{p}_{D^*\mu}^\perp = -\vec{p}_\nu^\perp$). The \parallel component can be calculated up to a twofold ambiguity by requiring energy (8.6) and momentum (8.7) conservation¹.

¹ In the following some abbreviations are used:

$\vec{p} \equiv \vec{p}_{D^*\mu}$, $\vec{p}_\perp \equiv \vec{p}_{D^*\mu}^\perp$, $\vec{p}_\parallel \equiv \vec{p}_{D^*\mu}^\parallel$, $E \equiv E_{D^*\mu}$, $m \equiv m_{D^*\mu}$

Energy conservation: (8.4)

$$\begin{aligned}
 E_{B^0} &= E_\nu + E \\
 &= \sqrt{\vec{p}_\nu^2} + E \\
 &= \sqrt{\vec{p}_\nu^{\parallel 2} + \vec{p}_\nu^{\perp 2}} + E \\
 &= \sqrt{\vec{p}_\nu^{\parallel 2} + \vec{p}_\perp^2} + E
 \end{aligned} \tag{8.5}$$

Momentum conservation:

$$\vec{p}_{B^0}^{\parallel} = \vec{p}_\nu^{\parallel} + \vec{p}_{\parallel} \tag{8.6}$$

$$\tag{8.7}$$

For the B^0 the energy-momentum relation holds:

$$m_{B^0}^2 = E_{B^0}^2 - \vec{p}_{B^0}^2 \tag{8.8}$$

$$= E_{B^0}^2 - \vec{p}_{B^0}^{\parallel 2} - \vec{p}_{B^0}^{\perp 2} \tag{8.9}$$

$$= E_{B^0}^2 - \vec{p}_{B^0}^{\parallel 2} \tag{8.10}$$

$$= E_{B^0}^2 - (\vec{p}_\nu^{\parallel} + \vec{p}_{\parallel})^2 \tag{8.11}$$

$$= (\sqrt{\vec{p}_\nu^{\parallel 2} + \vec{p}_\perp^2} + E)^2 - (\vec{p}_\nu^{\parallel} + \vec{p}_{\parallel})^2 \tag{8.12}$$

$$m_{B^0}^2 + \vec{p}_\nu^{\parallel 2} + \vec{p}_{\parallel}^2 + 2\vec{p}_\nu^{\parallel} \vec{p}_{\parallel} = \vec{p}_\nu^{\parallel 2} + \vec{p}_\perp^2 + E^2 + 2E\sqrt{\vec{p}_\nu^{\parallel 2} + \vec{p}_\perp^2} \tag{8.13}$$

$$m_{B^0}^2 - \vec{p}_\perp^2 - E^2 + \vec{p}_{\parallel}^2 + 2\vec{p}_\nu^{\parallel} \vec{p}_{\parallel} = 2E\sqrt{\vec{p}_\nu^{\parallel 2} + \vec{p}_\perp^2} \tag{8.14}$$

$$\underbrace{m_{B^0}^2 - m^2 - 2\vec{p}_\perp^2}_{\kappa} + 2\vec{p}_\nu^{\parallel} \vec{p}_{\parallel} = 2E\sqrt{\vec{p}_\nu^{\parallel 2} + \vec{p}_\perp^2} \tag{8.15}$$

$$\kappa^2 + 4\kappa\vec{p}_{\parallel} \vec{p}_\nu^{\parallel} + 4\vec{p}_{\parallel}^2 \vec{p}_\nu^{\parallel 2} = 4E^2 \vec{p}_\nu^{\parallel 2} + 4E^2 \vec{p}_\perp^2 \tag{8.16}$$

$$\begin{aligned}
 0 &= 4(\vec{p}_{\parallel}^2 - E^2)\vec{p}_\nu^{\parallel 2} + 4\kappa\vec{p}_{\parallel} \vec{p}_\nu^{\parallel} + \\
 &\quad \kappa^2 - 4E^2 \vec{p}_\perp^2
 \end{aligned} \tag{8.17}$$

$$\begin{aligned}
 0 &= \vec{p}_\nu^{\parallel 2} + \underbrace{\frac{\kappa\vec{p}_{\parallel}}{\vec{p}_{\parallel}^2 - E^2}}_e \cdot \vec{p}_\nu^{\parallel} + \\
 &\quad \underbrace{\frac{\kappa^2}{4(\vec{p}_{\parallel}^2 - E^2)} - \frac{E^2 \vec{p}_\perp^2}{\vec{p}_{\parallel}^2 - E^2}}_f
 \end{aligned} \tag{8.18}$$

This equation has the following solutions:

$$\vec{p}_\nu^\parallel(1,2) = -\frac{e}{2} \pm \sqrt{\frac{e^2}{4} - f} \quad (8.19)$$

$$= -a \pm \sqrt{r}, \quad (8.20)$$

with

$$a = \frac{(m_{B^0}^2 - m^2 - 2\vec{p}_\perp^2)\vec{p}_\parallel}{2(\vec{p}_\parallel^2 - E^2)} \quad (8.21)$$

$$r = \frac{(m_{B^0}^2 - m^2 - 2\vec{p}_\perp^2)^2 E^2}{4(\vec{p}_\parallel^2 - E^2)^2} + \frac{E^2 \vec{p}_\perp^2}{\vec{p}_\parallel^2 - E^2} \quad (8.22)$$

Mathematically and physically, both solutions are possible, but in a decay only one of them is realized. The occurrence of two solutions can be explained by looking at the decay in the rest frame of the B^0 (Figure 8.3(a)) and in the lab frame (Figure 8.3(b)). Since only the direction and not the magnitude of the B^0 momentum is known, one only knows that in the B^0 rest frame the absolute momentum of the neutrino and the $D^*\mu$ system must be equal: $|\vec{p}_\nu| = |\vec{p}|$. The neutrino can be emitted in forward or in backward direction. Since the B^0 is moving, the transverse components of the neutrino and the $D^*\mu$ system are boosted into the forward direction in the lab frame, while the transverse components stay unchanged.

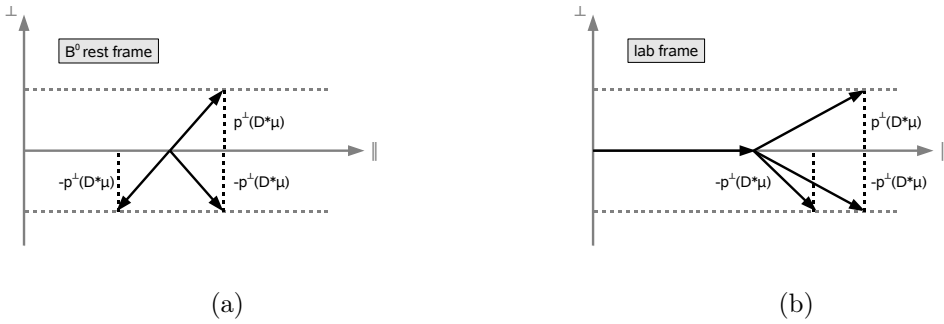


Figure 8.3: “Two-body-decay” of the B^0 meson in its restframe (a) and in the lab frame (b).

8.4 Comparison of k -Factor and Neutrino Reconstruction Method

To compare the neutrino reconstruction method and the k -factor method, a detailed study is done [42]. The goal of this comparison is to measure the B_s^0 oscillation frequency with both methods in the semileptonic decay mode. For this a MC simulation using the PYTHIA V6.227 [43] package with a center-of-mass energy of 14 TeV is done. The B_s^0 meson is forced to decay according to

$$B_s^0 \rightarrow D_s^- \mu^+ \nu_\mu, \quad D_s^- \rightarrow \phi \pi^-, \quad \phi \rightarrow K^+ K^-. \quad (8.23)$$

After applying some kinematic cuts, the track parameters and primary and secondary vertex positions are smeared according to Gaussian distributions to simulate the detector resolutions. The momentum uncertainty is simulated by smearing the pseudorapidity with $\sigma_\eta = 5.8 \times 10^{-4}$, the angle ϕ with $\sigma_\phi = 0.58$ mrad and the inverse transverse momentum with $\sigma_{(1/p_t)} = 0.013 \frac{1}{\text{GeV}/c}$. The primary vertex is smeared with $\sigma_{x,y} = 20 \mu\text{m}$ in both, x- and y-direction, the secondary vertex is smeared with $\sigma_{\parallel} = 70 \mu\text{m}$ in the flight direction of the B_s and $\sigma_{\perp} = 10 \mu\text{m}$ and $\sigma_{\perp} = 30 \mu\text{m}$, respectively, in the perpendicular direction. These values are expected to be reachable resolutions with the CMS experiment.

The transverse momentum of the B_s^0 meson is calculated using both methods. Its resolution as a function of the invariant mass of the $D_s^- \mu^+$ system is shown in Figure 8.4. It can be seen that, for the full mass range of the $D_s^- \mu^+$ system, the neutrino reconstruction method leads to better resolutions. Besides this, the influence of the precision of the secondary vertex position (comparing secondary vertex resolutions of $10 \mu\text{m}$ and $30 \mu\text{m}$ in \perp direction) on the B_s^0 transverse momentum resolution is shown. The secondary vertex resolution in \parallel direction has no influence on this resolution.

Figure 8.4 illustrates the proper time resolution obtained with the k -factor method (a) and the neutrino reconstruction method (b). For the latter method, the closest to the true value solutions are filled in the histogram. The distributions are fitted with two Gaussian functions, the average width σ is determined according to

$$\sigma^2 = \frac{N_n^2 \sigma_n^2 + N_w^2 \sigma_w^2}{N_n^2 + N_w^2}, \quad (8.24)$$

where σ_n (σ_w) and N_n (N_w) are the width and normalization of the narrow (wide) Gaussian, respectively. For the k -factor method, $\sigma_n = 100$ fs ($\sigma_w = 330$ fs) and $N_n = 2700$ ($N_w = 730$), which gives an average $\sigma = 132$ fs. For the neutrino reconstruction method $\sigma_n = 77$ fs ($\sigma_w = 193$ fs) and $N_n = 2300$ ($N_w = 660$) that gives an average

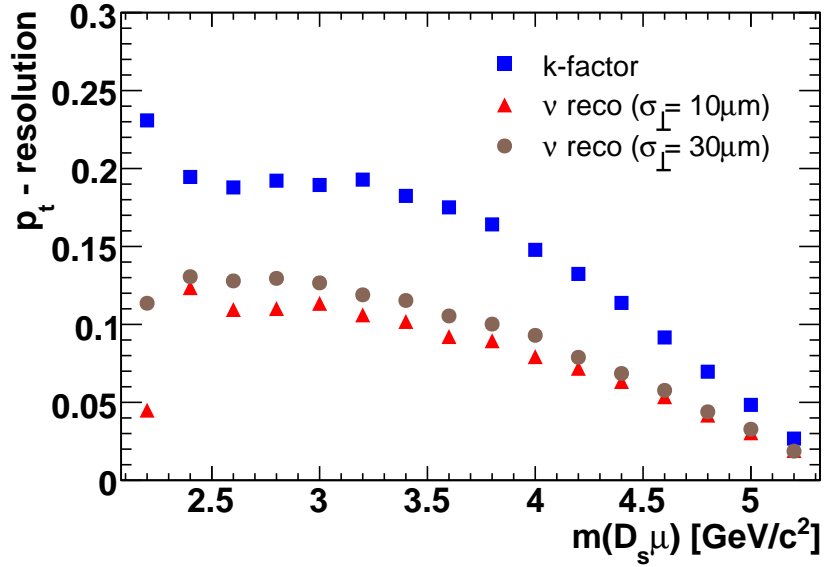


Figure 8.4: Relative B_s transverse momentum resolution calculated with k -factor and neutrino reconstruction method.

$\sigma = 91$ fs. The neutrino reconstruction method provides a proper time resolution which is substantially better than the k -factor reconstruction method.

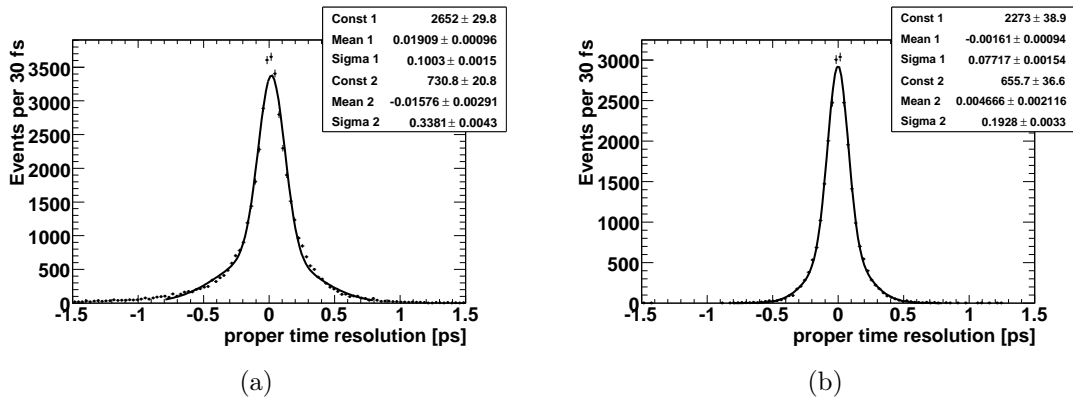


Figure 8.5: Proper time resolution obtained with the k -factor method (a) and the neutrino reconstruction method (b).

8.5 Experimental Limitations

The neutrino reconstruction method is sensitive to the precision of the measurement of $\vec{p}_{D^*\mu}$ and the resolutions of both the primary and secondary vertices. As shown in the above study, the most crucial parameter is the resolution of the secondary vertex perpendicular to the flight direction of the initial B meson. Hence it is very important to reconstruct this vertex with a high precision. A detailed comparison of different strategies for fitting this vertex will be given in Chapter 10.6.

The big advantage of the neutrino reconstruction method is that the full momentum of the B^0 meson can be calculated, and does not have to be applied based on averaging. Nevertheless, there are some experimental limitations. The calculation of the neutrino momentum leads to a quadratic equation with two solutions. One solution is the *right*, the other is the *wrong* one. Therefore the number of background events is increased by the number of *wrong* solutions from the signal as well as from the background sample. Again due to the quadratic equation and the resolutions, a certain fraction of events has a negative radicand r (Equation 8.22) and, hence, there is no solution for the B^0 meson momentum. Since this happens for both, signal and background events, the signal over background ratio is kept constant but the number of signal events is decreased.

Both problems can eventually be weakened. Firstly, it is possible to search for variables to distinguish *right* and *wrong* solutions and select only one of them for each B^0 meson. Secondly, it is possible to set the radicand to 0 if there was no solution. An investigation of these two possibilities will follow in Chapter 10.7.

9

Monte Carlo Production

9.1 Simulation

Within this analysis all data is simulated. For the physics processes the event generator PYTHIA [43] is used in version 6.416 with the underlying event settings and probability density functions shown in Table 9.1. The package EvtGen [44] is focused on b hadron decays, it provides a framework to handle complex sequential decays and CP violating decays. Hence, all c and b hadrons are kept stable within PYTHIA and passed over to EvtGenLHC (a modified version of EvtGen, which is designed for a hadron collider environment), which lets them decay.

After the generation of all decays, the response of the CMS detector is simulated using the full detector simulation based on GEANT4 [45]. It simulates the physics processes that accompany the passage of particles through the hierarchy of volumes and materials that compose the CMS detector. Although this is very CPU time consuming, it provides very precise results that are needed especially for the determination of secondary vertices. At this stage of the simulation, the data is in a state like it would be measured with the CMS detector.

Both the event generation and the simulation of the detector reaction, are implemented in the CMS software (CMSSW) used in version 2_1_0. This software is also used for the reconstruction of the initial event. It writes out physical objects like tracks, momenta, vertices, missing transverse energy, etc. All simulation is done with a center-of-mass energy of 14 TeV.

9.2 The Signal Sample

To extract efficiencies and resolutions, a large sample of 8374000 minimum bias events is produced. To all of them, several filters at generator level are applied to

ensure that they are within a geometrically and kinematically reconstructible region. There has to be one muon within a pseudorapidity range of $-2.4 \leq \eta(\mu) < 2.4$. To 26% (or 2174000 events), a single muon filter of $p_t(\mu) > 2.5 \text{ GeV}/c$, and to 74 % (6200000 events) of them, a single muon filter of $p_t(\mu) > 4.5 \text{ GeV}/c$ is applied. Additionally, a B^0 meson has to be in each event, which is forced to decay according to the signal chain in Equation 7.11 with a branching ratio of $\mathcal{B} = 1.38 \times 10^{-3}$. After these requirements, 6022 events are left, which corresponds to an efficiency of 7.2×10^{-4} .

With a cross section of 55 mb this amount of data corresponds to an integrated luminosity of $\mathcal{L} = 110 \text{ nb}^{-1}$ and a data taking time of 15 hours at startup luminosity of $2 \times 10^{30} \text{ cm}^{-2}\text{s}^{-1}$. Hence, this analysis is an excellent candidate for both

- measuring a physical quantity with the very first data
- probing a new method (neutrino reconstruction) with real data

The lifetime of the B^0 meson used by EvtGenLHC is 1.536 ps.

9.3 The Data Sample

Beside the signal sample, 4.6×10^8 minimum bias events are generated, which corresponds to an integrated luminosity of $\mathcal{L} = 8.28 \text{ nb}^{-1}$. Here, only a kinematic and a geometric single muon filter are applied, $p_t(\mu) > 4.5 \text{ GeV}/c$, $-2.4 \leq \eta(\mu) < 2.4$. The requirement on the transverse momentum of the muon lies slightly below the lowest HLT single muon threshold (compare Table 10.1). To receive a realistic composition of the sample, no particle is forced to a specific decay. This guarantees that all currently known physics is used as a possible background, not only specific channels one assumes to be background are taken into account. After the kinematic cuts, 106992 events are left, which corresponds to a efficiency of 2.35×10^{-2} .

This amount of data corresponds to a data taking time of 69 minutes at startup luminosity of $2 \times 10^{30} \text{ cm}^{-2}\text{s}^{-1}$.

Table 9.1: Underlying event settings and probability density functions used by the PYTHIA generator.

PYTHIA setting	Description
MSTJ(11)=3	Choice of the fragmentation function.
MSTJ(22)=2	Decay those unstable particles for which $c\tau < 10$ mm.
PARJ(71)=10	
MSTP(2)=1	Which order running α_s .
MSTP(33)=0	No k-factors in hard cross sections.
MSTP(51)=7	Structure function chosen (external PDF CTEQ6L1).
MSTP(81)=1	Multiple parton interactions.
MSTP(82)=4	Defines the multi-parton model.
MSTU(21)=1	Check on possible errors during program execution.
PARP(82)=1.9409	p_t cutoff for multiparton interactions.
PARP(89)=1960.	\sqrt{s} for which PARP82 is set.
PARP(83)=0.5	Multiple interactions: matter distribution parameter
PARP(84)=0.4	Multiple interactions: matter distribution parameter
PARP(90)=0.16	Multiple interactions: rescaling power
PARP(67)=2.5	Amount of initial-state radiation.
PARP(85)=1.0	Gluon production mechanism.
PARP(86)=1.0	Gluon production mechanism.
PARP(62)=1.25	
PARP(64)=0.2	
MSTP(91)=1	
PARP(91)=2.1	
PARP(93)=15.0	

10

Event Reconstruction

After an event is reconstructed with CMSSW and all physical objects are written, it is analyzed if the event contains the required decay or not. Therefore, it is important to understand the geometrical and kinematical properties of the required decay, and its differences to other decays. For the signal decay in Equation 7.11 of this analysis, the following objects should be detected by CMS:

- A muon track.
- Two charged hadron tracks (kaon and pion) in approximately the same direction as the muon. Since they come from the D^0 decay, their invariant mass should be consistent with the mass of this meson.
- A charged low p_t track (slow pion) in roughly the same direction as the muon.

The following charge correlations need to be fulfilled: The charges of the muon and the kaon must be equal and opposite to the charges of the pion and the slow pion, whose charges must be equal as well. Since CMS offers no hadron particle identification, a kaon and a pion track can not be distinguished.

The reconstruction of the signal decay is done in two steps, one with quite loose selection criteria (candidate construction in Chapter 10.2) and a tougher one (candidate selection in Chapter 10.4).

10.1 Trigger Paths

A criterion with which the trigger system decides whether a reconstructed event is accepted or not, is the transverse momentum of muons. They are excellent physics

objects to trigger on, since they provide a signal in two subdetectors, the tracking system, and the muon system. As shown in Figure 2.6(b), the reconstruction efficiency for muons with high transverse momenta is close to 100 % over a large pseudorapidity range. Two main trigger channels for muons exist, a single and a di-muon trigger. As their names suggest, they accept an event if at least one or two muons above certain transverse momentum thresholds are reconstructed. For the single muon trigger, the threshold lies higher.

At the LHC startup, the machine will not provide the nominal luminosity from the beginning. It will rather be increased step by step. Since a lower luminosity causes less particles to be measured per time span, the trigger system is allowed to accept more events. For the muon triggers, this means that the threshold is allowed to be lower for lower luminosities. The exact HLT values, for a single muon or two muons, as a function of the instantaneous luminosity, are given in Table 10.1.

Table 10.1: Transverse momentum threshold for the single and the double muon HLT.

Luminosity	single muon p_t [GeV/c]	double muon p_t [GeV/c]
$2 \times 10^{30} \text{ cm}^{-2}\text{s}^{-1}$	7	3
$1 \times 10^{31} \text{ cm}^{-2}\text{s}^{-1}$	9	3
$2 \times 10^{31} \text{ cm}^{-2}\text{s}^{-1}$	16	3
$1 \times 10^{32} \text{ cm}^{-2}\text{s}^{-1}$	16	3

Both muon trigger channels can be used for this analysis. One muon is already present in the signal of the decay. The double muon trigger responds for those events, for which the hadron, produced by the second b quark, decays semileptonically with a muon among its final state particles. The advantage of using also the double muon trigger channel is that also signal events producing muons with lower transverse momenta can be analyzed. Since this analysis is tailored to the startup phase of the LHC, it can profit from the low thresholds at this luminosity.

Figure 10.1 shows the transverse momentum distribution of the generated signal muons (only those 6200000 events with the higher single muon p_t filter). The cutoffs at 3 GeV/c and 4.5 GeV/c represent the requirements on the muon in the candidate construction (Chapter 10.2) and the single muon filter at generator level (Chapter 9), respectively. The muons between 3 GeV/c and 4.5 GeV/c contain a second muon that passed the generator level filter.

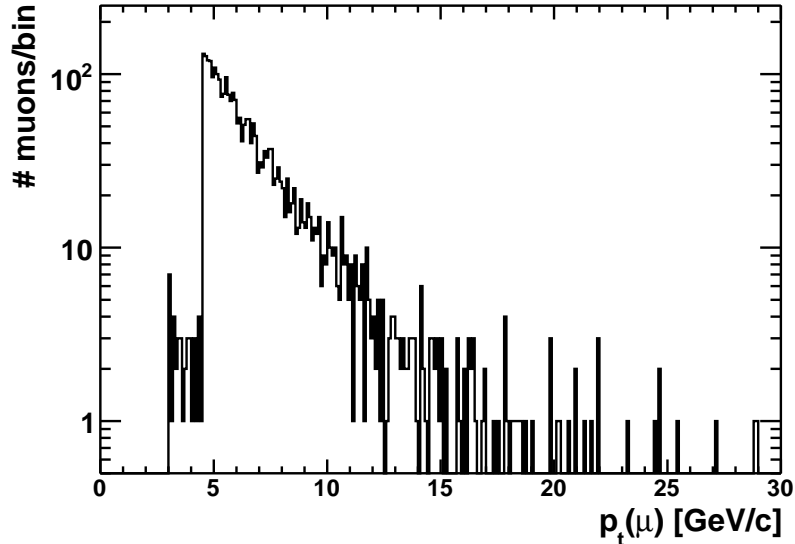


Figure 10.1: Transverse momentum distribution of the generated muons.

10.2 Candidate Construction

In a first step of analyzing the events reconstructed by the CMS software, several loops over all reconstructed tracks are performed to build different combinations of tracks that could constitute the products of the signal decay. For each event, all possible combinations are stored. Since in the reconstruction the identity of the muon can be determined, one starts with this track(s). Afterwards, among all tracks with the same charge as the muon track and a transverse momentum greater than $1 \text{ GeV}/c$, a track is searched that lies in a cone of $\Delta R = \sqrt{\Delta\eta^2 + \Delta\phi^2} \leq 1.5$ around the muon track. It is assumed to be the kaon track. If such a track is found, among all tracks with opposite charge as the muon and a transverse momentum greater than $1 \text{ GeV}/c$, a track within $\Delta R \leq 1.5$ around the muon is searched (pion track). If such a combination also exists, among all tracks of the same charge as the muon track, it is searched for one that lies within $\Delta R \leq 1$ around the muon track. Because this pion has a low transverse momentum, no further demands are made. Since the kaon and the pion track should come from the decay of the D^0 meson, their invariant mass should be consistent with its mass. The $K\pi$ -system is required to lie in a cone of $\Delta R \leq 1$ around the muon and of $\Delta R \leq 0.4$ around the slow pion track. All requirements are summarized in Table 10.2. To illustrate that the cut values are reasonably chosen, the distribution of each cut variable is plotted after

applying all previous cuts in Figure 10.2 and Figure 10.3.

Table 10.2: Requirements on all tracks that compose a signal candidate.

	p_t [GeV/c]	charge q	ΔR to μ
μ	3	–	–
K	1	$= q(\mu)$	1.5
π	1	$\neq q(\mu)$	1.5
π_s	–	$\neq q(\mu)$	1

	m_{inv} [GeV/c ²]	ΔR to μ	ΔR to π_s
$K\pi$ -system	≥ 1.6 and ≤ 2.1	1	0.4

Not all tracks emerging from signal decays fulfill all the cuts in Table 10.2. To quantify how many of the events containing the signal decay result in a candidate, the efficiencies of the cuts are determined on generator level for the signal sample. Note that the cut on the invariant mass of the $K\pi$ -system can not be tested on this level, since the invariant mass on generator level is always identical to the D^0 meson mass. The results are shown in Table 10.3. It can be seen that most events get lost due to the p_t cut on the kaon and the pion. Overall, 38 % of the signal events pass the candidate construction cuts on generator level.

Table 10.3: Efficiencies of the candidate construction cuts.

Cut	# Events	Efficiency [%]	cumulative Efficiency [%]
generator level cuts	6022	7.2×10^{-4}	—
$p_t(\mu) > 3 \text{ GeV}/c$	4925	82	82
$p_t(K) > 1 \text{ GeV}/c$	3703	75	61
$\Delta R(\mu, K) < 1.5$	3659	99	61
$p_t(\pi) > 1 \text{ GeV}/c$	2319	63	39
$\Delta R(\mu, \pi) < 1.5$	2296	99	38
$\Delta R(\pi_s, \mu) < 1.0$	2270	99	38
$\Delta R(\pi_s, D^0) < 0.4$	2269	100	38
$\Delta R(\mu, D^0) < 1.0$	2260	100	38

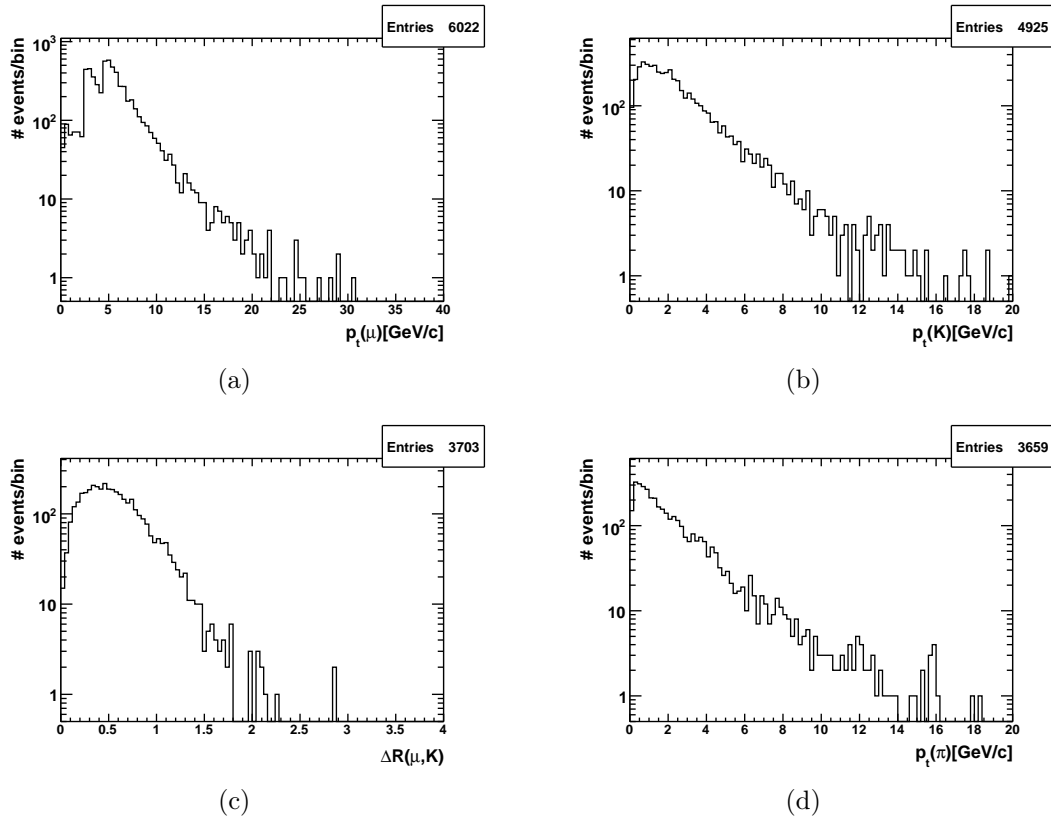


Figure 10.2: Distribution of the cut variables $p_t(\mu)$ (a), $p_t(K)$ (b), $\Delta R(\mu, K)$ (c), and $p_t(\pi)$ (d) after applying all previous cuts.

10.3 Track Reconstruction Efficiencies

Besides the purely kinematical reason that no candidate is built from a signal event, there are other influences. Firstly, the tracks may lie in a geometrical region where no detector is placed ($|\eta|$ too high). Another reason is that the detector components are not a hundred percent efficient. If some hits in the tracker get lost, this might cause the reconstruction software not to be able to reconstruct the track at all. Including also those inefficiencies, the signal candidate is contained in 939 events or 16 % of the cases.

A critical point in the full reconstruction of the signal decay is the slow pion. Since its transverse momentum is so low, the probability of reconstructing it with the standard software is very low. Nevertheless, within CMSSW, a dedicated algorithm was developed, focused on the reconstruction of very low p_t tracks [46]. This

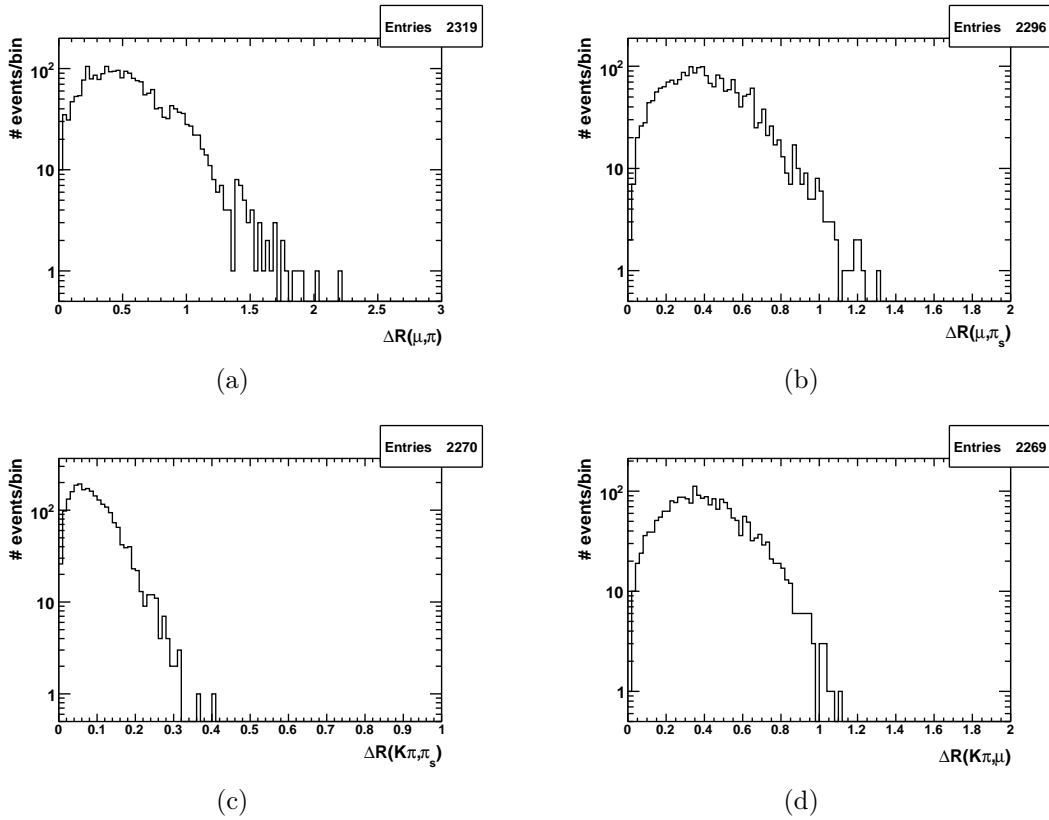


Figure 10.3: Distribution of the cut variables $\Delta R(\mu, \pi)$ (a), $\Delta R(\pi_s, \mu)$ (b), $\Delta R(\pi_s, D^0)$ (c), and $\Delta R(\mu, D^0)$ (d) after applying all previous cuts.

algorithm is able to reconstruct pion tracks down to $0.1 \text{ GeV}/c$ in the range $|\eta| < 1$ with an efficiency above 80 %. The reconstruction efficiency ε of the slow pion in this analysis, where it can lie in the full η range, is shown in Figure 10.4.

10.4 Candidate Selection

After a variable number of candidates is constructed per event, it has to be decided, if one of those candidates and which one really corresponds to the signal candidate. Because of the relatively loose cuts in the candidate construction, candidates are also present in events that do not contain a signal decay at all. Therefore, handles need to be found to distinguish signal and background candidates. Here, the advantage of having a slow pion in the decay chain comes into play. With $\Delta M \equiv M(K, \pi, \pi_s) - M(K, \pi)$ a variable for the difference in the invariant masses of the kaon, the pion,

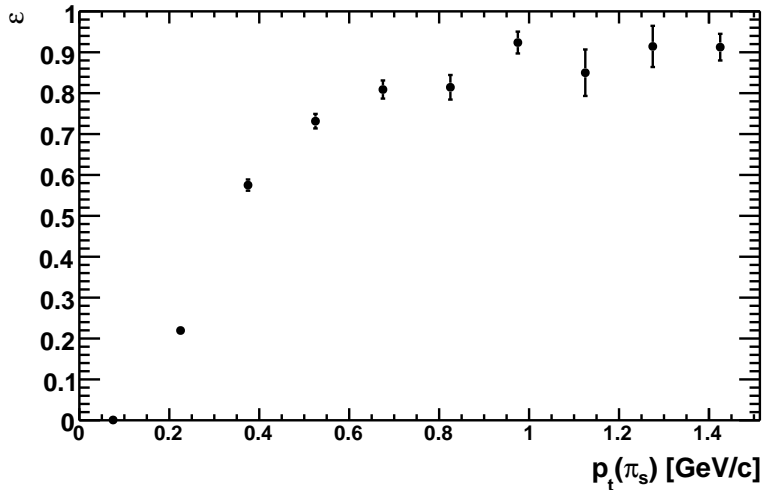


Figure 10.4: Reconstruction efficiency ε of the slow pion as a function of its transverse momentum.

and the slow pion on the one hand and of only the kaon and the pion on the other hand is used.

In Table 7.3, the masses for the D^* , the D^0 and the π mesons are given. The difference between the masses of the D^* and the D^0 meson is $145.5 \text{ MeV}/c^2$, while the mass of the pion is $139.57 \text{ MeV}/c^2$. Hence, the variable ΔM is restricted to a very small range for signal events. For background events, where at least one of the tracks is not the one it is accounted for, ΔM can be distributed over a broad range.

The distribution of ΔM for signal and background candidates is shown in Figure 10.5. It can be seen that the signal candidates show a clear peak, while the background candidates are distributed over a broad range. Note that the little bump of the background inside the signal region comes from peaking background events, which are discussed in more detail below.

Since ΔM provides such a good distinction between signal and background candidates, the selection is done in the following way. If more than one candidate is present for an event, only those ones will be used that fulfill $0.139 \text{ GeV}/c^2 \leq \Delta M \leq 0.150 \text{ GeV}/c^2$. If after this selection criterion still more than one candidate is present in an event, the one with the highest p_t of the reconstructed D^0 meson is selected. With this selection procedure, a purity of 93.5% is reached. This means that, if a signal candidate is present in an event, in 93.5% of the cases it is selected.

The results of the candidate selection performed on the “data” sample are shown in Table 10.4. In the first part it can be seen that for 33.1% of the 106992 events

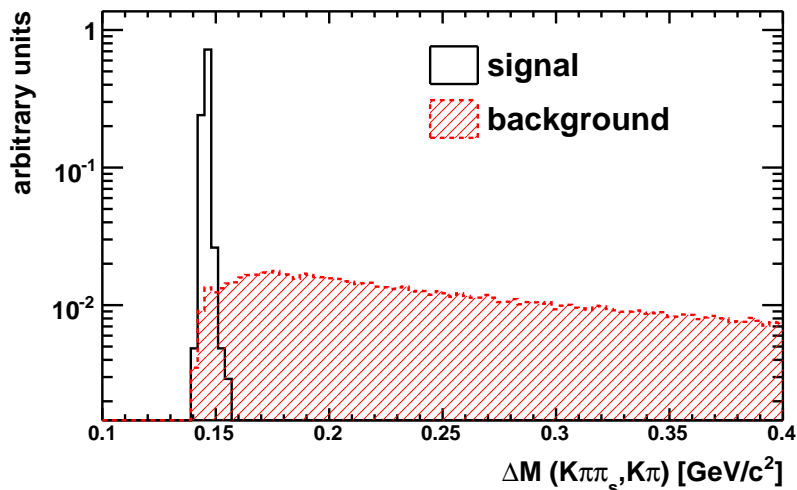


Figure 10.5: Distribution of ΔM for signal and background candidates in arbitrary units.

that survive the generator level filters, at least one candidate is constructed. In the second and third part it is distinguished between the signal and background events among the mixture of all possible minimum bias decays. 99.7% of the events, for which a candidate is written, do not contain the signal decay. This is only present in 0.3%. Contradictory to that, for only 7.6% of the huge number of background events, one of the candidates is considered as a signal candidate. If an event contains a signal candidate, in 93.5% of the cases it is as well selected. Only in 5.4%, another candidate is selected, and only in 1.1%, no candidate is selected at all.

Table 10.5 summarizes the output of the candidate selection. For 7.8% of the 35447 events that contain a candidate, one of those candidates is assumed to represent a signal decay. This is correct in 3.1% of the cases while 96.9% of the selected candidates are background.

10.5 D^0 Mass Distributions

Despite the fact that the candidate selection based on the ΔM criterion determines signal candidates with high purity, there are still background candidates present for which ΔM by accident lies in the signal region. For all those events, the invariant mass of the kaon and the pion is plotted in Figure 10.6. A clear signal peak from D^0 mesons on top of background candidates can be seen. The distribution is fitted with

Table 10.4: Candidate selection overview in the “data” sample.

	# Events	Percentage [%]
# events containing at least one candidate	35447	33.1
# events containing the good candidate	92	0.3
• selected	86	93.5
• other selected	5	5.4
• none selected	1	1.1
# events containing only wrong candidates	35355	99.7
• anyway one selected	2679	7.6
• none selected	32676	92.4

Table 10.5: Signal and background events after candidate selection in the “data” sample.

	# Events	Percentage [%]
Events with a selected candidate	2770	7.8
Signal events	86	3.1
Background events	2684	96.9
• from $B_{(s)}^0 \bar{B}_{(s)}^0$ mixing	8	0.3
• from $c\bar{c}$	34	1.3

a Gaussian function over a linear background. The dotted blue line shows the linear part of the fit, the dashed red line the Gaussian part. Comparing the integral of this fit (119 events) with the number of signal events that should be in the distribution (86 events), there is a discrepancy, even when considering the fit error of 23 events.

Those events inside the signal peak come from peaking background. Two possible sources of such background are:

- **$c\bar{c}$ events:** A $c\bar{c}$ quark pair is produced, and the \bar{c} quark hadronizes into a D^{*-} meson that results in a negatively charged slow pion, a positively charged kaon, and a negatively charged pion. The charmed hadron from the second c quark decays semileptonically producing a positively charged muon.
- **$B^0 \bar{B}^0$ mixing:** From the two initial b quarks, a B^0 and a \bar{B}^0 are produced

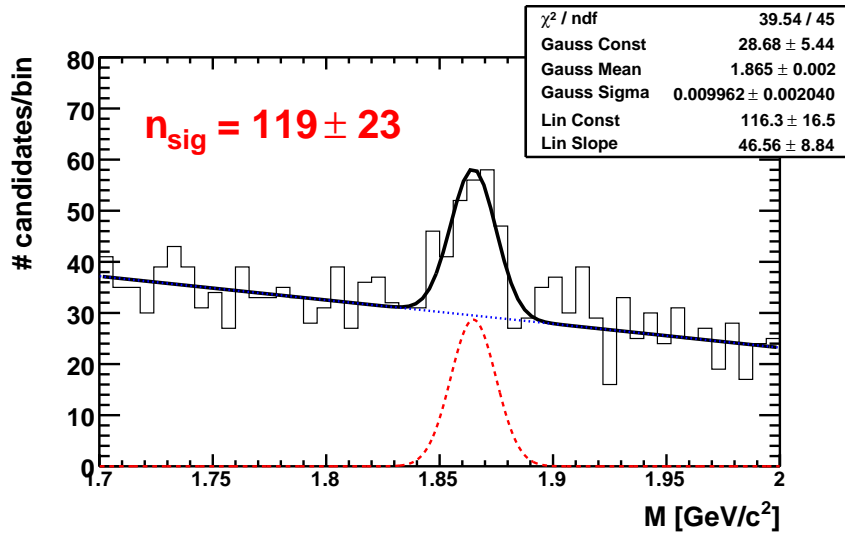


Figure 10.6: D^0 mass distribution of all events where a candidate is selected, fitted with a Gaussian peak over a linear background. The dashed red line shows only the Gaussian fraction of the fit, the dotted blue only the linear fraction.

and one of them mixes. If it then decays semileptonically, the produced muon can be combined with the slow pion, the kaon, and the pion from the signal decay, fulfilling the charge correlations.

Both kinds of events can survive the ΔR candidate construction cuts, when the two initial c or b quarks are produced with a small angular separation by gluon splitting.

The obtained mass distribution with all events separated into the signal, the two peaking and the one non-peaking background channel is shown in Figure 10.7.

10.6 Vertex Fitting

As mentioned in Chapter 8.5, the precision of the secondary vertex reconstruction has a strong influence on the quality of the neutrino reconstruction method. Within CMSSW, different methods of vertex fitting are available, for example a simple Kalman vertex fitting, an adaptive vertex fitting or a kinematic vertex fitting.

From the decay of the B^0 meson, besides the undetected neutrino, a D^* meson and a muon arise. The D^* decays instantaneously, hence, the D^0 meson, the slow pion and the muon point to the B^0 decay vertex. Since the D^0 is not a measured track, it can not be used for the vertex fit within the conventional fit methods. Three

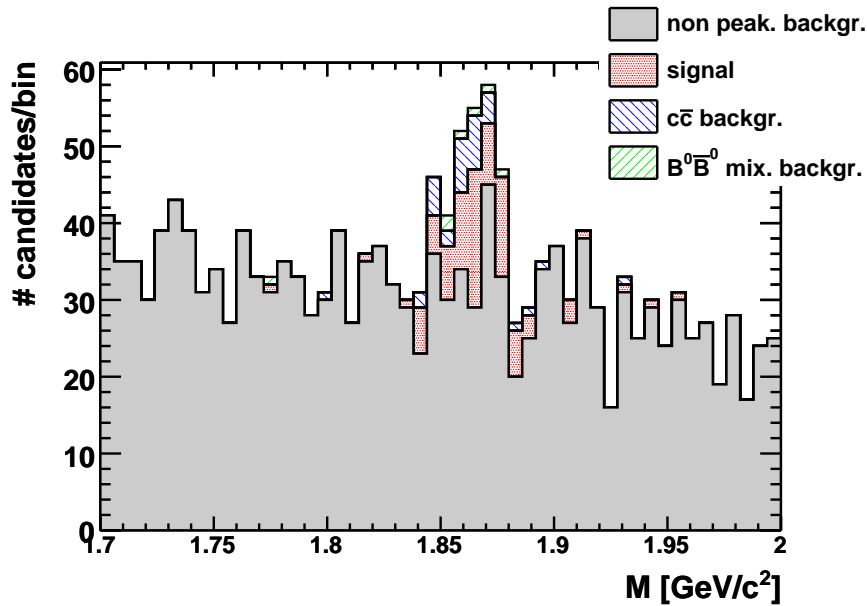


Figure 10.7: D^0 mass distribution split into signal and different sources of background.

different approaches of fitting the secondary vertex are tested and compared in the following:

- (a) Using only the muon and the slow pion in a Kalman vertex fitter.
- (b) Assuming the decay length of the D^0 meson to be negligible and using its decay products (kaon and pion) together with the muon in a Kalman vertex fitter.
- (c) Using a kinematic vertex fit [47] that constrains masses and vertices.

For the cases (a) and (b), the D^0 decay vertex is fitted using the kaon and the pion track and all tracks are refitted constraining them to their originating vertex. Before coming to these three possibilities in more detail, the principal differences between the standard Kalman vertex fitter and the kinematic vertex fitter are discussed.

10.6.1 The Kinematic Vertex Fitter

In a Kalman fitter, only tracks can be fitted to vertices. This is a good solution for decays where the initial particle directly decays to the final state products. If there

are intermediate states, the knowledge of the geometrical (e.g. decay length) and kinematical (e.g. mass) properties is completely neglected in the fit. This missing information leads to an increased error in the resolution of a vertex. If a particle with finite lifetime is present in the decay chain, the vertex position is biased.

The goal of the kinematic vertex fitter is to avoid this problem by introducing 4-vector-like kinematic particles that serve as an input to the fit. For tracks, mass hypotheses need to be provided before fitting. With this strategy, it is possible to make a bottom-up fitting, beginning from the final state particles to the initial particle. For each step, vertex and mass constraints can be applied.

In the case of the signal decay of this analysis, in a first step the kaon and the pion are fitted to a common vertex, while constraining the mass of the resulting intermediate state to the mass of the D^0 meson. In a second step the D^0 meson is fitted together with the muon and the slow pion.

10.6.2 Different Approaches of Fitting the B^0 vertex

All three approaches of fitting the secondary vertex are applied to the signal sample and various quantities are compared. For the secondary vertex, the differences of the generated and the reconstructed vertex position in B^0 flight direction \parallel and perpendicular to this direction \perp are compared. Afterwards, the B^0 decay length (distance from primary to secondary vertex) and its proper time (using Equation 7.12) are calculated and also compared to their respective values on generator level. Since the quality of the secondary vertex reconstruction has such a strong influence on the neutrino reconstruction, it is also compared, in how many cases it is successful and in how many cases it fails (negative radicand r). The resolution of the transverse momentum of the $D^*\mu$ -system is also compared for the different approaches, it is around 0.1 GeV/ c for all fit methods.

All resolution histograms are fitted with a single Gaussian function. The histograms for the kinematic fit are shown. The one of the secondary vertex resolution perpendicular to the B^0 flight direction in Figure 10.8(a), the one of the secondary vertex resolution in B^0 flight direction in Figure 10.8(b). The resolution of the decay length is shown in Figure 10.8(c), the one of the proper time in Figure 11.2.

Since the obtained resolutions are biased, besides the sigma of the Gaussian fit in Table 10.6, there is also given the peak position in Table 10.7.

Table 10.6 shows that the quality of the secondary vertex, and therefore also of the decay length and the proper time of the B^0 meson, strongly depends on the fit method. Compared to the kinematic fit, the first method (slow pion and muon) is four times worse in the width of the Gaussian function. The reason for this is the low momentum of this pion that causes it to undergo multiple scattering, through which its direction is changed. This is also the reason why the peak of the Gaussian

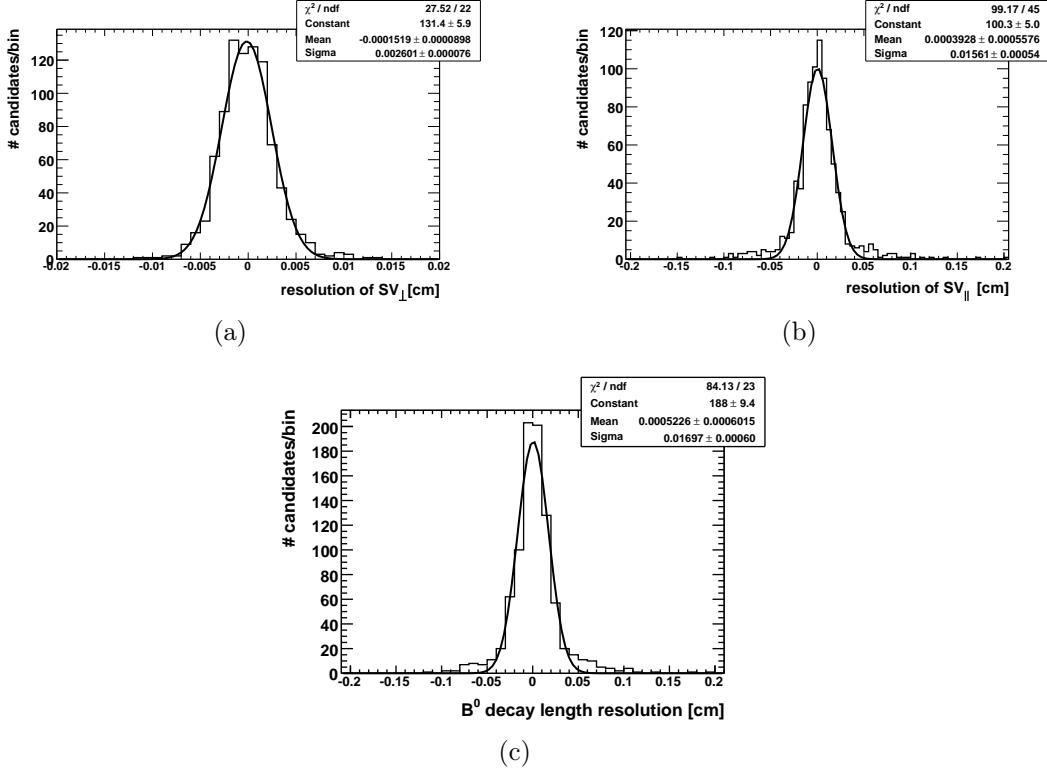


Figure 10.8: Resolution of the secondary vertex perpendicular to the B^0 flight direction (a) and in B^0 flight direction (b). Resolution of the B^0 decay length (c).

Table 10.6: Width of various resolution distributions for different approaches of fitting the B^0 vertex.

	$\Delta SV_{\parallel} [\mu\text{m}]$	$\Delta SV_{\perp} [\mu\text{m}]$	$\Delta L_{B^0} [\mu\text{m}]$	$\Delta\tau [ps]$
μ, π_s	683 ± 34	62 ± 2	626 ± 31	0.41 ± 0.05
μ, K, π	199 ± 8	30 ± 1	218 ± 9	0.26 ± 0.02
kinematic fit	156 ± 5	26 ± 1	170 ± 6	0.18 ± 0.01

fit (Table 10.7) is not consistent with 0 on the one hand, but on the other hand much closer to 0 than the peak position obtained with the three tracks fit (b).

The improvement in the width of the fit from the three tracks fit to the kinematic fit is only about 20%, while the peak lies more than seven times closer to 0 for the proper time. This huge shift for the three tracks fit comes from the assumption

that the decay length of the D^0 meson can be neglected. The combined vertex is shifted towards the position of the D^0 decay vertex. For the resolution component of the secondary vertex transverse to the B^0 flight direction, no significant difference between the three tracks fit and the kinematic fit can be seen.

The kinematic fit shows for all compared quantities the best results. Especially the resolution of the lifetime (the variable that one wants to measure) is improved by a factor three to four for both, width and peak position of the Gaussian fit. Note that even with the kinematic fit there is a small bias of 0.04 ps in the resolution of the proper time. This means that in the final results, the reconstructed lifetime of the B^0 meson is expected to be 0.04 ps larger than the lifetime used in the event generation with EvtGenLHC:

$$\tau_{expected} = (1.536 + 0.04) \text{ ps} \quad (10.1)$$

Table 10.7: Peak position of various resolution distributions for different approaches of fitting the B^0 vertex.

	$\Delta SV_{\parallel} [\mu\text{m}]$	$\Delta SV_{\perp} [\mu\text{m}]$	$\Delta L_{B^0} [\mu\text{m}]$	$\Delta \tau [\text{ps}]$
μ, π_s	-23 ± 26	-17 ± 3	86 ± 24	0.11 ± 0.04
μ, K, π	183 ± 9	0 ± 1	193 ± 10	0.28 ± 0.02
kinematic fit	4 ± 6	-1 ± 1	5 ± 6	0.04 ± 0.01

Beside the resolutions, it is also possible to compare the number of candidates for which the reconstruction of the neutrino is successful, since this affects the number of available signal candidates. The results are shown in Table 10.8. It can be seen that the highest efficiency is obtained when using the three track fit, followed by the kinematic fit, and the first fit method. It is not known, why the neutrino reconstruction works more successful with the three track fit than with the kinematic fit.

10.7 Results of the Neutrino Reconstruction

In general, there are two different outcomes of the neutrino momentum reconstruction:

- The reconstruction is successful and two solutions for the neutrino momentum exist.

Table 10.8: Percentage of candidates with successful neutrino reconstruction, i.e. $r \geq 0$.

ν -reco	
μ, π_s	43%
μ, K, π	62%
kinematic fit	51%

- The radicand in the quadratic equation for calculating the neutrino momentum is negative. The neutrino reconstruction failed and no solution exists.

Each of the outcomes has consequences, as already explained in Chapter 8.5, namely a decrease in the signal over background ratio and in the number of signal events. In the following, it is discussed how those consequences can be limited.

10.7.1 Selection of a Neutrino Solution

To compare the two solutions of the neutrino reconstruction, it has to be determined, which one is the one that really represents the decay and which one is the just possible solution. This is done by comparing the transverse momentum of the generated neutrino with the transverse momenta of the two reconstructed solutions. The solution for which this difference is smaller is tagged as the *right* solution, the other one is tagged as the *wrong* solution.

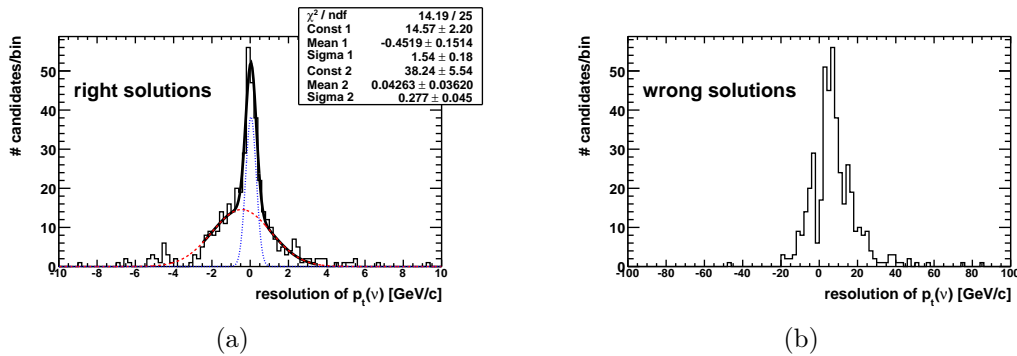


Figure 10.9: Transverse momentum resolution of the reconstructed neutrino for the *right* (a) and *wrong* (b) solutions.

The resolutions obtained for the *right* and the *wrong* solutions are shown in Figure 10.9. The distribution for the right solutions is fitted with two Gaussian functions, the width $\sigma = 1.1 \text{ GeV}/c$ is given by the second central moment. Note that the x -axis for the *wrong* solutions is stretched by a factor 10 with respect to the one for the *right* solutions.

If a criterion is found to decide which solution is the *right* one, the B^0 momentum, and from this the proper time of each B^0 meson, can be calculated only once per candidate. The transverse momentum of the neutrino is found to be a good variable for this discrimination. Its distribution, separated into the *right* and the *wrong* solutions, is shown in Figure 10.10.

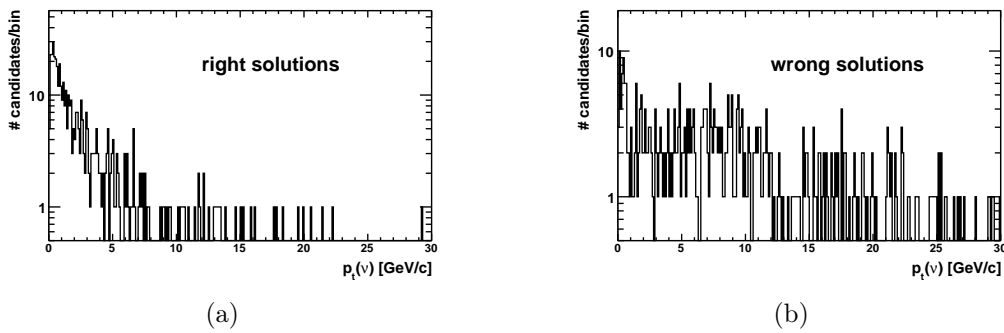


Figure 10.10: Transverse momentum distribution of the reconstructed neutrino for the *right* (a) and *wrong* (b) solutions.

From those distributions, one can conclude that it is a reasonable strategy to select always the neutrino solution with the lower transverse momentum. By doing this, in 78% of the cases the *right* neutrino solution is selected. This can also be seen in Figure 10.11, which shows the transverse momentum difference between the *right* and the *wrong* solution. Since the number of candidates below 0 is larger than the number of those above 0, it is also shown on an event-by-event basis that it is reasonable to select the solution with the lower transverse momentum.

10.7.2 Candidates with a Negative Radicand

Another question is, if the candidates, for which the neutrino reconstruction failed, are really lost, or if the proper time of the B^0 meson for those events, although with a worse resolution, can be reconstructed. To test this, two different methods are applied to the signal sample, for both a lifetime fit is done and its result is compared to the lifetime used by EvtGenLHC.

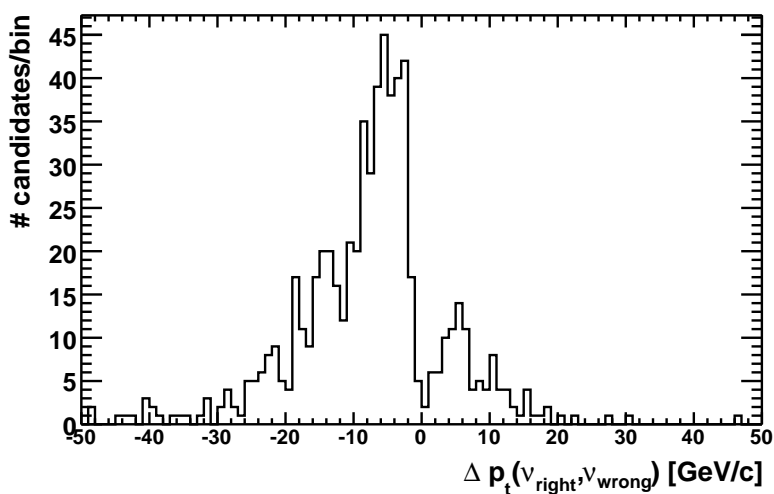


Figure 10.11: Difference between the *right* and *wrong* solution of the transverse momentum of the reconstructed neutrino.

- (a) If the radicand r is smaller than zero, one can set it to zero instead: $r = 0$
- (b) If the radicand r is smaller than zero, one can set the full parallel component of the neutrino momentum in Equation 8.20 to zero: $\vec{p}_\nu^{\parallel}(1, 2) = 0$

The proper time resolutions obtained with the two methods are shown in Figure 10.12. Since the biases of 0.05 ps for method (a) and 0.06 ps for method (b) are increased compared to the case when only using successful solutions, the candidates with a negative radicand are not used at all.

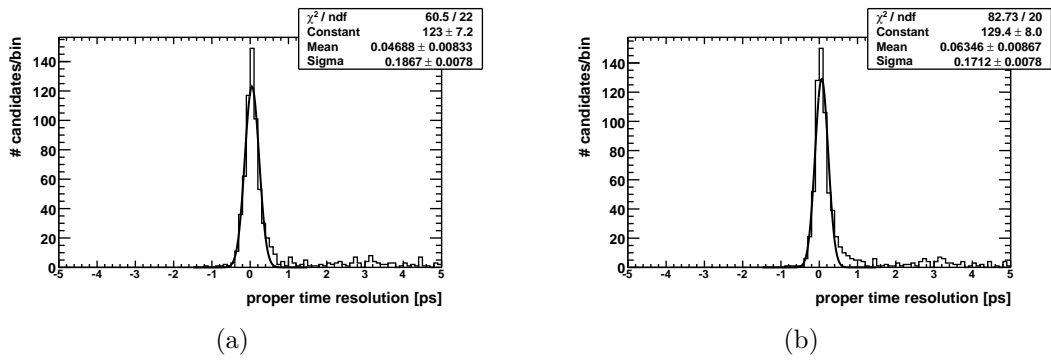


Figure 10.12: Proper time resolutions when candidates with negative radicands are used for the methods (a) and (b).

11

Study of the Lifetime Measurement

11.1 Proper Time Reconstruction

The resolution of the proper time has already been used when comparing the different methods of fitting the B^0 vertex. Only events are used for which the momentum of the $D^*\mu$ -system points in roughly the same direction like the vector between the primary vertex and the B^0 decay vertex. This is done to remove those candidates, for which the primary vertex lies “behind” the secondary vertex. A distribution of the angle between the momentum of the $D^*\mu$ -system and the vector between the primary vertex and the B^0 decay vertex is shown in Figure 11.1. It can be seen that there are some candidates for which this angle is greater than 90° . Those candidates are removed from the analysis since they would result in a negative proper time.

Figure 11.2 shows the resolution for the kinematic fit. The shift towards a too high reconstructed lifetime of 0.04 ps and the resolution of 0.16 ps can be observed. There are also some outliers, for which the reconstructed proper time is much higher than the generated one. The reason for the outliers is that for those events the tagging as *right* and *wrong* solution did not work correctly. By accident, the difference in the transverse momentum between the generated and the *wrong* solution was smaller than between the generated and the *right* solution.

11.2 Lifetime Fit

After using the ΔM criterion for the candidate selection, there is still a large number of background candidates in the sample that are fitted with a linear function (compare Figure 10.6). To further reduce this number, a signal region of $\pm 2\sigma$ around the peak of the Gaussian fit is defined, $M(K\pi) = 1.86 \text{ GeV}/c^2 \pm 0.02 \text{ GeV}/c^2$. Within

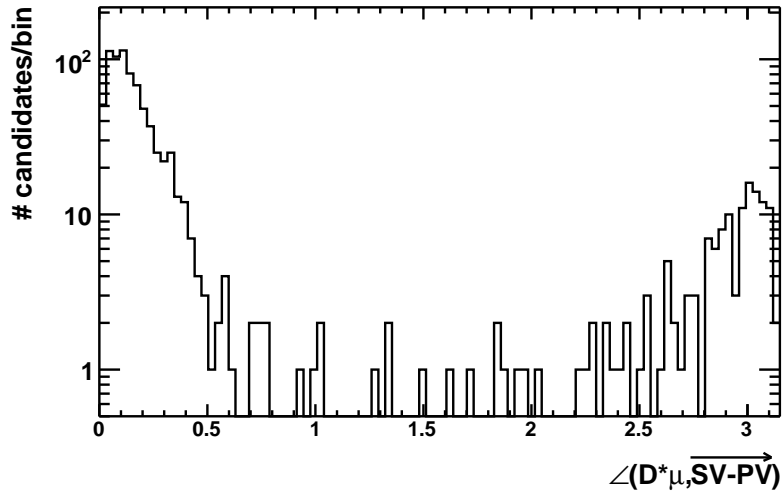


Figure 11.1: Angle between the momentum of the $D^*\mu$ -system and the vector between the primary vertex and the B^0 decay vertex.

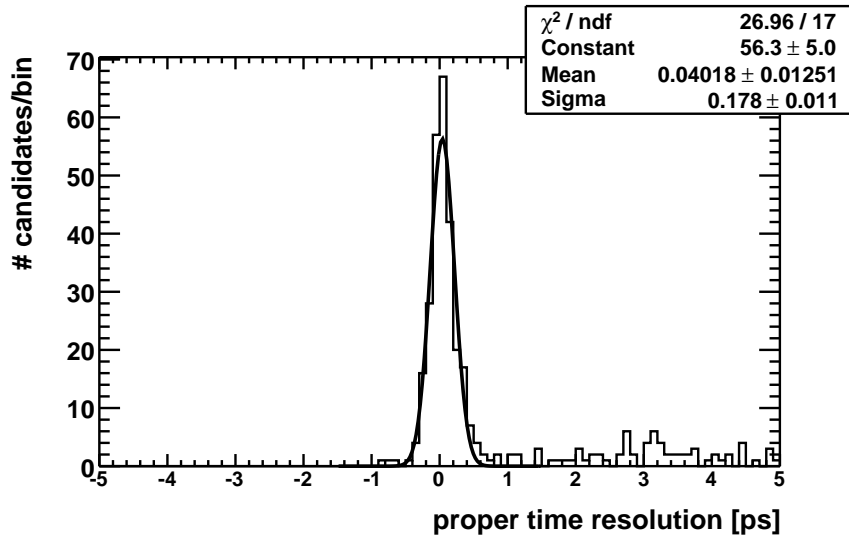


Figure 11.2: Resolution of the reconstructed proper time.

this region, the signal-over-background ratio is $S/B = 55/133 = 0.41$ and the significance $S/\sqrt{B} = 4.77$. An interesting point is that the neutrino reconstruction has a positive influence on these two numbers. It works more successfully for signal

candidates than for background candidates. After requiring a successful neutrino reconstruction, these numbers change to $S/B = 30/40 = 0.75$ and $S/\sqrt{B} = 4.74$, respectively. Figure 11.3 shows the invariant mass distribution of the $K\pi$ -system, using only the candidates with a successful neutrino reconstruction.

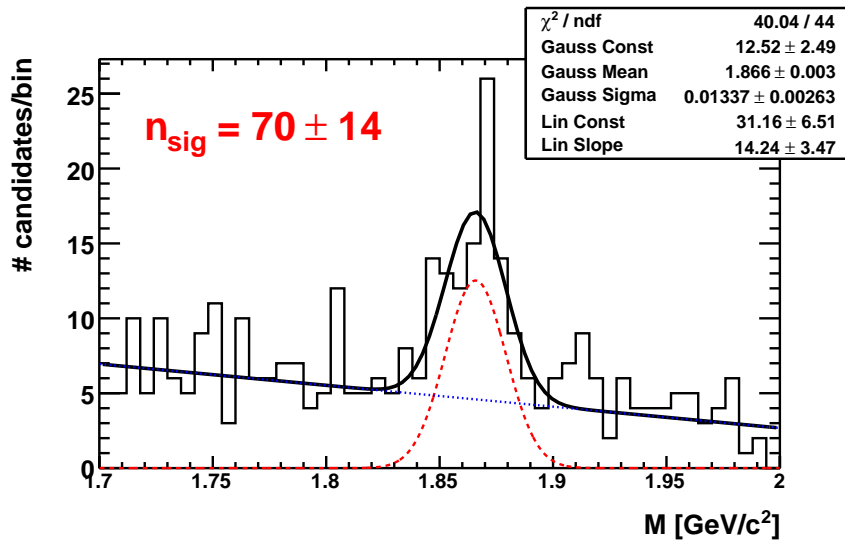


Figure 11.3: D^0 mass distribution of all events where a candidate is selected and the neutrino reconstruction worked successfully, fitted with a Gaussian peak over a linear background. The dashed red line shows only the Gaussian fraction of the fit, the dotted blue only the linear fraction.

To further reduce the number of background candidates, the decay length significance of the B^0 meson would be a good criterion. But since this introduces a bias into the proper time distribution a different procedure is chosen. Within the signal region there are two sources of background, namely normal background candidates (peaking and non-peaking) and background from wrongly selected solutions of the neutrino reconstruction.

The proper time distribution for these two sources of background using the full mass range of the $K\pi$ -system is shown separately in Figure 11.4. The normal background is fitted with an exponential function and the resulting lifetime is calculated¹ as the inverse value of the slope of the exponential function as (1.88 ± 0.16) ps. The shape of the proper time distribution for wrongly selected solutions of the neutrino reconstruction is significantly different, in particular it is not exponential.

The signal-over-background ratio inside the signal region can be calculated from

¹All proper time distributions are fitted using a binned maximum likelihood fit.

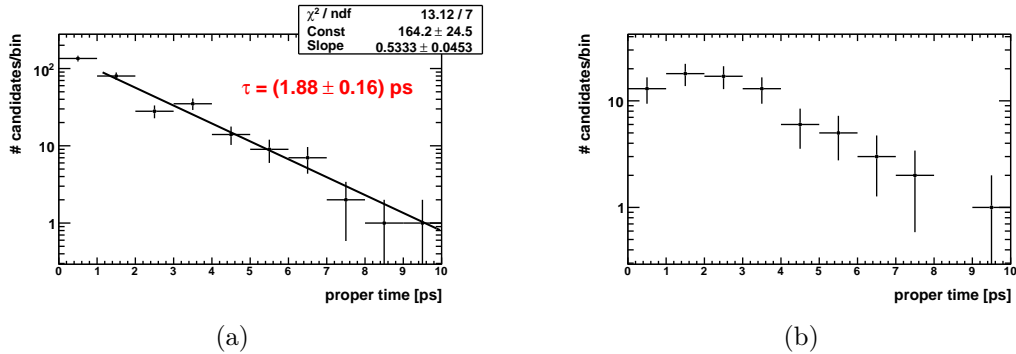


Figure 11.4: Proper time distribution for normal background (a) and wrongly selected solutions of the neutrino reconstruction (b).

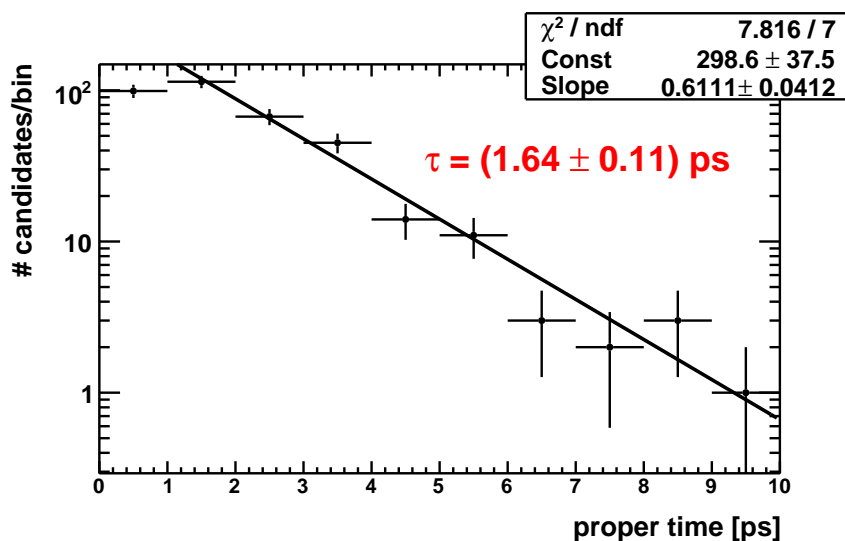
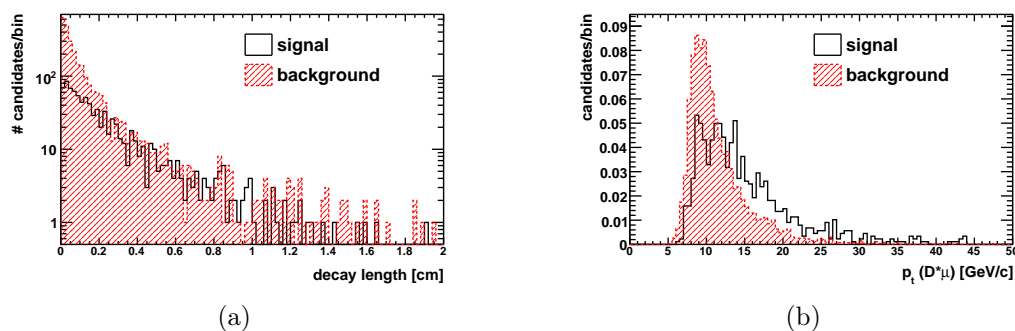
data by comparing the integral of the Gaussian function and the linear function in Figure 11.3. The percentage of peaking background in the Gaussian part and the percentage of wrongly selected neutrino reconstruction solutions have to be taken into account and can be extracted from MC information. To extract the shape of the background from data, sideband regions in the mass distribution of the $K\pi$ -system can be defined, where there are no signal candidates.

To verify that the reconstruction of the full B^0 momentum and of its decay length and therefore also of the B^0 lifetime works successfully, the signal sample is used. In this sample the proper time is calculated for those candidates, for which the neutrino reconstruction is successful. The values of all *right* solutions are filled into a histogram and fitted with an exponential function as shown in Figure 11.5. The resulting lifetime with its statistical uncertainty is also given, it is $(1.64 \pm 0.11) \text{ ps}$ which is consistent with the expected value τ_{expected} .

11.3 Shape of the Proper Time Distribution

In Figure 11.5 it can be seen, that the distribution of the proper time deviates from an exponential behaviour in the first bin. The reason for this lies in the neutrino reconstruction method. As mentioned above, this method does not give a solution for some candidates. Two ingredients that are used to calculate the proper time are the decay length of the B^0 meson and the momentum of the $D^*\mu$ -system. The distributions of both variables for signal and background candidates are shown in Figure 11.6.

The efficiency of the neutrino reconstruction as a function of those two variables is shown in in Figure 11.7. It is higher for signal than for background candidates.

Figure 11.5: Reconstructed proper time for *right* solutions of signal candidates.Figure 11.6: B^0 decay length (a) and transverse momentum of the $D^*\mu$ -system (b) for signal and background candidates.

For both, no dependency on the transverse momentum of the $D^*\mu$ -system can be seen, while the dependency on the decay length is strong. It is much lower for lower decay lengths for both signal and background, which results in missing entries in the first bin of the proper time distribution. Since the shape of the efficiency is different for signal and background, it would introduce a bias in the proper time distribution, when filling each event weighted according to its decay length. Instead of doing this, the proper time distribution is only fitted in a range where it shows an exponential behaviour for correctly selected signal solutions.

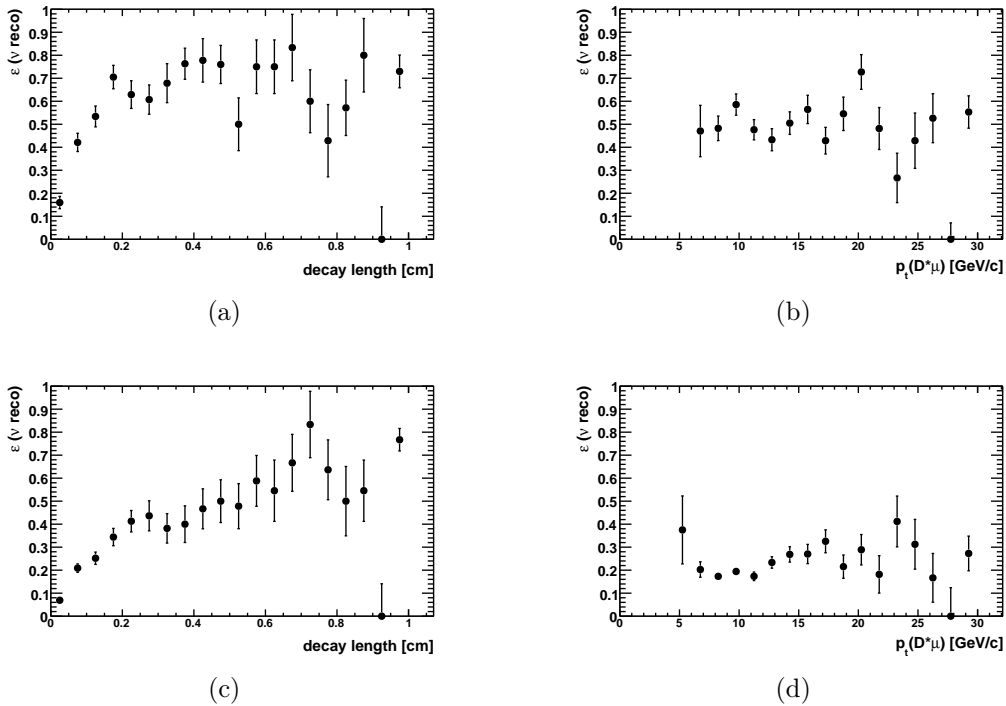


Figure 11.7: Neutrino reconstruction efficiency as a function of the B^0 decay length (a),(c) and the transverse momentum of the $D^*\mu$ -system (b),(d). The distributions on the top are for signal, the one on the bottom for background candidates.

11.4 Systematic Errors

Beside the pure statistical uncertainties, there are a couple of systematics that have an influence on the quality of the measurement.

- **Efficiencies** As explicitly seen in case of the (un)successful neutrino reconstruction, efficiencies can have a strong biasing influence on the results. Therefore also track reconstruction efficiencies need to be investigated.
- **Peaking Background** There is an uncertainty on the fraction of peaking background candidates inside the signal peak.
- **Wrongly selected solutions of the neutrino reconstruction** Also the fraction of candidates for both signal and background is only known to a certain precision.

- **Misalignment** If the detector is misaligned, the position resolutions of the vertices are degraded. This negatively influences the proper time resolution.

11.5 Outlook

This analysis already shows promising results in the current state. The lifetime for signal events can be extracted without a bias. To extract the lifetime also from the data sample, an unbinned maximum likelihood fit needs to be performed. This is necessary, since the number of both signal and background candidates is not big enough to fit all components with a binned maximum likelihood fit. Beside this, binning always introduces a loss of information.

In the unbinned maximum likelihood fit, at least three probability distribution functions (*pdf*) should be used in dependency of the proper time and the invariant mass of the $K\pi$ -system, one for signal, one for normal background and one for the wrongly selected solutions of the neutrino reconstruction. The shape of the pdf for normal background can be extracted from candidates in the sideband regions, while the shape of the wrongly selected solutions of the neutrino reconstruction needs to be determined based on MC information. Potentially it is helpful to treat the peaking background separately.

It is very likely that the quality of the measurement even with an unbinned maximum likelihood fit can be optimized. Since the current data sample corresponds to a data taking time of 15 hours at startup luminosity of $2 \cdot 10^{30} \text{ cm}^{-2}\text{s}^{-1}$, it is not a problem to increase the statistics significantly.

Since in this analysis the influence of a trigger is only simulated by requiring a muon with $p_t > 4.5 \text{ GeV}/c$, the real influence of the HLT needs to be investigated in more detail. Furthermore, the influence of a misaligned detector is not studied so far.

Conclusions

This work is divided into two parts. In the first one, optimization algorithms for the analog readout chain of the CMS barrel pixel detector modules have been developed and tested. An analog readout is used to reach a precise resolution of the hits produced by charged tracks penetrating the CMS pixel barrel detector. Several DACs can be adjusted to optimize the precision of this readout. Four optimization criteria have been defined that have been used to optimize the setting of the DACs. It has been decided whether a specific DAC needs to be adjusted dynamically, i.e. the procedure has to be repeated for every produced readout chip, or if it can be set to the same value for all chips. For the DACs that need to be dynamically optimized, algorithms have been developed and applied.

The functionality of these approaches has been checked on the one hand by comparing a large number of optimized readout chips. On the other hand, a CMSSW simulation was done, comparing the influence of different DAC settings on the hit resolution of the detector.

In the second part a measurement of the B^0 lifetime has been studied in the semileptonic decay mode using a new reconstruction method. The neutrino appearing in this decay is usually treated as a missing particle that has to be corrected for, based on averaged Monte Carlo information. The new method makes use of the geometrical information that is present and reconstructs the neutrino momentum up to a twofold ambiguity. Since geometrical information, here especially the position of the B^0 decay vertex, is a key ingredient for this method, it can profit from the optimization of the analog readout chain in the first part of this work. Furthermore, different algorithms of fitting this vertex have been compared and a kinematic fit was found to give the most precise results. The proper time resolution was found to be 0.18 ps with a bias of 0.04 ps towards too large proper times.

The background suppression was done by requiring the difference of the invariant masses of the $K\pi\pi_s$ -system and the $K\pi$ -system to be between $0.139 \text{ GeV}/c^2$ and

$0.150 \text{ GeV}/c^2$, and the invariant mass of the $K\pi$ -system to be $M(K\pi) = 1.86 \text{ GeV}/c^2 \pm 0.02 \text{ GeV}/c^2$. For the remaining candidates, the proper time distributions have been plotted separately for signal and background, resulting in significantly different lifetimes. The resulting value for the signal candidates of

$$\tau_{reco} = (1.64 \pm 0.11_{\text{stat}}) \text{ ps} \tag{12.1}$$

was consistent with expected value. Hence, the lifetime of the B^0 meson could be reconstructed using the new method of reconstructing the missing neutrino with an integrated luminosity of $\mathcal{L} = 110 \text{ nb}^{-1}$.

Bibliography

- [1] Lyndon Evans and Philip Bryant. LHC Machine. *JINST*, 3:S08001, 2008.
- [2] CERN press release, First beam in the LHC - accelerating science, PR08.08, 10.09.2008.
- [3] CERN press release, Incident in LHC sector 3-4, PR09.08, 20.09.2008.
- [4] CERN press release, LHC re-start scheduled for 2009, PR10.08, 23.09.2008.
- [5] CERN press release, CERN releases analysis of LHC incident, PR14.08, 16.10.2008.
- [6] Higgs, Peter W. Broken symmetries, massless particles and gauge fields. *Phys. Lett.*, 12:132–133, 1964.
- [7] Higgs, Peter W. Broken symmetries and the masses of gauge bosons. *Phys. Rev. Lett.*, 13:508–509, 1964.
- [8] F. Englert and R. Brout. Broken symmetry and the mass of gauge vector mesons. *Phys. Rev. Lett.*, 13:321–322, 1964.
- [9] G. S. Guralnik, C. R. Hagen, and T. W. B. Kibble. Global conservation laws and massless particles. *Phys. Rev. Lett.*, 13:585–587, 1964.
- [10] Michael Spira and Peter M. Zerwas. Electroweak symmetry breaking and Higgs physics. 1997.

- [11] M. Dittmar and A.S. Nicollerat. High Mass Higgs Studies Using $gg \rightarrow H$ and $qq \rightarrow qqH$ at the LHC. CERN-CMS-NOTE-2001-036.
- [12] Y. Ashie et al. A Measurement of Atmospheric Neutrino Oscillation Parameters by Super-Kamiokande I. *Phys. Rev.*, D71:112005, 2005.
- [13] J. Wess and B. Zumino. Supergauge Transformations in Four-Dimensions. *Nucl. Phys.*, B70:39–50, 1974.
- [14] G. L. Bayatian et al. CMS physics: Technical design report. CERN-LHCC-2006-001.
- [15] R. Adolphi et al. The CMS experiment at the CERN LHC. *JINST*, 3:S08004, 2008.
- [16] S. Dasu et al. CMS. The TriDAS project. Technical design report, vol. 1: The trigger systems. CERN-LHCC-2000-038.
- [17] P. Sphicas. CMS: The TriDAS project. Technical design report, Vol. 2: Data acquisition and high-level trigger. CERN-LHCC-2002-026.
- [18] W. Adam et al. The CMS high level trigger. *Eur. Phys. J.*, C46:605–667, 2006.
- [19] I. Vila. The CMS hardware alignment system. Prepared for 1st LHC Detection Alignment Workshop, Geneva, Switzerland, 4-6 Sep 2006.
- [20] Y. Allkofer et al. Design and performance of the silicon sensors for the CMS barrel pixel detector. *Nucl. Instrum. Meth.*, A584:25–41, 2008.
- [21] L. Rossi, P. Fischer, T. Rohe, and N. Wermes. Pixel detectors: From fundamentals to applications. Berlin, Germany: Springer (2006) 304 p.
- [22] K. Gabathuler. PSI46 Pixel Chip - External Specification. Villigen, Switzerland (2005).
- [23] E. Bartz. The 0.25 μm token bit manager chip for the CMS pixel readout. Prepared for 11th Workshop on Electronics for LHC and Future Experiments (LECC 2005), Heidelberg, Germany, 12-16 September 2005.
- [24] L. Wehrli. Study of Time Walk Behaviour of CMS Pixel Modules. Diploma Thesis, Zurich, (2007).
- [25] A. Starodumov et al. Qualification procedures of the CMS pixel barrel modules. *Nucl. Instrum. Meth.*, A565:67–72, 2006.

- [26] C. Gharagouzloo. Impact of the Energy Threshold Dispersion on the Position Resolution of the CMS pixel detector. Semester Thesis, Zurich, (2008).
- [27] Yoichiro Nambu. Axial vector current conservation in weak interactions. *Phys. Rev. Lett.*, 4:380–382, 1960.
- [28] J. Goldstone. Field Theories with Superconductor Solutions. *Nuovo Cim.*, 19:154–164, 1961.
- [29] J. H. Christenson, J. W. Cronin, V. L. Fitch, and R. Turlay. Evidence for the 2π Decay of the K Meson. *Phys. Rev. Lett.*, 13(4):138–140, Jul 1964.
- [30] Makoto Kobayashi and Toshihide Maskawa. CP Violation in the Renormalizable Theory of Weak Interaction. *Prog. Theor. Phys.*, 49:652–657, 1973.
- [31] J. E. Augustin, A. M. Boyarski, M. Breidenbach, F. Bulos, J. T. Dakin, G. J. Feldman, G. E. Fischer, D. Fryberger, G. Hanson, B. Jean-Marie, R. R. Larsen, V. Lüth, H. L. Lynch, D. Lyon, C. C. Morehouse, J. M. Paterson, M. L. Perl, B. Richter, P. Rapidis, R. F. Schwitters, W. M. Tanenbaum, F. Vannucci, G. S. Abrams, D. Briggs, W. Chinowsky, C. E. Friedberg, and G. Goldhaber. Discovery of a Narrow Resonance in e^+e^- Annihilation. *Phys. Rev. Lett.*, 33(23):1406–1408, Dec 1974.
- [32] J. J. Aubert, U. Becker, P. J. Biggs, J. Burger, M. Chen, G. Everhart, P. Goldhagen, J. Leong, T. McCorrison, T. G. Rhoades, M. Rohde, Samuel C. C. Ting, Sau Lan Wu, and Y. Y. Lee. Experimental Observation of a Heavy Particle J . *Phys. Rev. Lett.*, 33(23):1404–1406, Dec 1974.
- [33] F. Abe, H. Akimoto, A. Akopian, M. G. Albrow, S. R. Amendolia, D. Amidei, J. Antos, C. Anway-Wiese, S. Aota, G. Apollinari, T. Asakawa, W. Ashmanskas, M. Atac, P. Auchincloss, F. Azfar, P. Azzi-Bacchetta, N. Bacchetta, W. Badgett, S. Bagdasarov, M. W. Bailey, J. Bao, P. de Barbaro, A. Barbaro-Galtieri, V. E. Barnes, B. A. Barnett, P. Bartalini, and G. Bauer. Observation of Top Quark Production in $p\bar{p}$ Collisions with the Collider Detector at Fermilab. *Phys. Rev. Lett.*, 74(14):2626–2631, Apr 1995.
- [34] B. Aubert et al. Measurement of the CP-violating asymmetry amplitude $\sin 2\beta$. *Phys. Rev. Lett.*, 89:201802, 2002.
- [35] K. Abe et al. An improved measurement of mixing-induced CP violation in the neutral B meson system. *Phys. Rev.*, D66:071102, 2002.

- [36] The Royal Swedish Academy of Science. Scientific Background on the Nobel Prize in Physics 2008, Broken Symmetries, compiled by the Class for Physics of the Royal Swedish Academy of Sciences, (2008).
- [37] D. H. Perkins. Introduction to High Energy Physics. Reading, USA: Addison-Wesley (1982) 437 p.
- [38] Lincoln Wolfenstein. Parametrization of the Kobayashi-Maskawa Matrix. *Phys. Rev. Lett.*, 51:1945, 1983.
- [39] C. Amsler et al. Review of particle physics. *Phys. Lett.*, B667:1, 2008.
- [40] E. Norrbin and T. Sjostrand. Production and hadronization of heavy quarks. *Eur. Phys. J.*, C17:137–161, 2000.
- [41] R. Keith Ellis, I. Hinchliffe, M. Soldate, and J. J. van der Bij. Higgs Decay to $\tau^+\tau^-$: A Possible Signature of Intermediate Mass Higgs Bosons at the SSC. *Nucl. Phys.*, B297:221, 1988.
- [42] S. Dambach, U. Langenegger, and A. Starodumov. Neutrino reconstruction with topological information. *Nucl. Instrum. Meth.*, A569:824–828, 2006.
- [43] Torbjorn Sjostrand, Stephen Mrenna, and Peter Skands. PYTHIA 6.4 physics and manual. *JHEP*, 05:026, 2006.
- [44] D. J. Lange. The EvtGen particle decay simulation package. *Nucl. Instrum. Meth.*, A462:152–155, 2001.
- [45] S. Agostinelli et al. GEANT4: A simulation toolkit. *Nucl. Instrum. Meth.*, A506:250–303, 2003.
- [46] Ferenc Sikler. Low p_t hadronic physics with CMS. *Int. J. Mod. Phys.*, E16:1819–1825, 2007.
- [47] K. Prokofiev and T. Speer. A kinematic fit and a decay chain reconstruction library. *CMS Internal Note*, CMS-IN-2004/020.

Acknowledgements

First of all I would like to express my great gratitude to Urs Langegger for taking me to Switzerland and giving me the opportunity to do this PhD study. I treasure the time he took for continuous discussions and explanations. Great thanks to Roland Horisberger who also never hesitated to answer my questions. It was a great pleasure to work in the kind and competent environment of the pixel group. I would like to thank Andrey Starodumov for supporting me in both the hardware and the analysis part. Furthermore I would like to mention Christina Eggel and Peter Trüb, with whom I discussed miscellaneous aspects of work.

Beside this, I thank the whole pixel group for the interesting Monday morning meetings and all other helpful discussions. I am especially grateful to Beat Meier, who never stopped explaining my electronics questions and who made all those long S6 trips feel much shorter. Hans-Christian Kästli and Wolfram Erdmann invested a lot of time in explaining DAC functionalities.

Thanks to Gürkan Sengün and Axel Beckert for all their support and collaboration in computing questions. Derek Feichtinger and Zhiling Chen helped a lot to finish all my grid jobs in time. I also appreciate the help of Thomas Speer with the kinematic vertex fit.

I am very thankful to Astrid Bauer for reading this work far into the night. Thanks also to Antonia, Christine and Sascha for the kind evenings when we joined together. I also cherish the companionship with all other friends from the Elim.

My big gratitude goes to mum, dad and Samuel for never giving up motivating me. Thanks for always being there for me. I am deeply grateful to Emanuel, who guided my vision into the correct direction.

My biggest gratitude goes to the Lord without whom I would never be where I am.

*I will sing to the LORD all my life;
I will sing praise to my God as long as I live.
Psalms 104:33*

Curriculum Vitae

Personal Data

Name and Address: Sarah Dambach
Schaffhauserstrasse 405
8050 Zürich
Switzerland
043 300 9790

Date of Birth: June 10, 1980
Place of Birth: Speyer, Germany
Nationality: German

Education

11/2005 - 09/2008 ETH Zurich und Paul Scherrer Institute Villigen,
PhD in Experimental Particle Physics

10/2000 - 10/2005 Ruprecht-Karls-Universität Heidelberg,
Study of Physics and Theology
("Verbesserung eines Experiments zur Messung
der Myonenlebensdauer und -polarisation
für das Fortgeschrittenenpraktikum")

08/1991 - 07/2000 Edith-Stein-Gymnasium Speyer, Abitur

08/1987 - 07/1991 Primary School in Böhl